



**The vacuolar TPC1 channel and its luminal calcium sensing
site in the luminal pore entrance**

Der vakuoläre TPC1-Kanal und seine luminal Kalzium-Sensorstelle im luminalen
Porenbereich

Dissertation on the attainment of a doctorate in natural sciences

Julius-Maximilians-Universität Würzburg,

submitted by

Jinping Lu

from

Henan, China

Würzburg

(2021)





**The vacuolar TPC1 channel and its luminal calcium sensing
site in the luminal pore entrance**

Der vakuoläre TPC1-Kanal und seine luminal Kalzium-Sensorstelle im luminalen
Porenbereich

Dissertation on the attainment of a doctorate in natural sciences

Julius-Maximilians-Universität Würzburg,

submitted by

Jinping Lu

from

Henan, China

Würzburg

(2021)

Submitted on:

Office stamp

Members of the Thesis Committee

Chairperson:

Primary Supervisor: Prof. Dr. Irene Marten

Supervisor (Second): Prof. Dr. Erhard Wischmeyer

Date of Public Defence:

Date of Receipt of Certificates:

Corrigendum/Addendum

Parts of this thesis have been published in:

Dickinson MS, Lu JP, Gupta M, Marten I, Hedrich R, Stroud RM 2022. Molecular basis of multistep voltage activation in plant two-pore channel 1. *Proc. Natl. Acad. Sci. U S A*, **119**, e2110936119; doi: 10.1073/pnas.2110936119.

Lu JP, Dreyer I, Dickinson MS, Panzer S, Jašlan D, Navarro-Retamal C, Geiger D, Terpitz U, Becker D, Stroud RM, Marten I, Hedrich R 2023. *Vicia faba* SV channel VfTPC1 is a hyperexcitable variant of plant vacuole Two Pore Channels. *eLife* **e86384**. doi: 10.7554/eLife.86384.

Table of Content

1. Introduction	1
1.1. The plant vacuole	1
1.2. Ion channels of the plant vacuole	4
1.2.1. The fast vacuolar (FV) channel.....	5
1.2.2. The two-pore K ⁺ channel TPK	5
1.2.3. The non-selective vacuolar cation channel SV/TPC1	7
1.3. Objective of the work	16
2. Materials and methods.....	18
2.1. Generation of TPC1 constructs.....	18
2.1.1. User primer design	18
2.1.2. PCR reaction	19
2.1.3. Subcloning of TPC1-WT channel variants	20
2.1.4. Site-directed mutagenesis	21
2.1.5. Bacterial transformation by heat shock.....	23
2.1.6. Isolation and sequencing of plasmids.....	24
2.1.7. Isolation of midi plasmid-DNA for transient protoplast transformation	25
2.2. Transient transformation of mesophyll protoplasts.....	25
2.2.1. Plant materials and growth condition.....	25
2.2.2. Preparation of fresh enzyme solution	26
2.2.3. Enzymatical isolation of mesophyll protoplast	26
2.2.4. PEG-based protoplast transformation	27
2.2.5. Vacuole isolation.....	28
2.2.6. Fluorescent imaging of channel expression	29
2.3. Electrophysiology.....	29
2.3.1. Patch-clamp technique	29
2.3.2. Patch-clamp configurations	30
2.3.3. Components of a patch-clamp setup.....	32

2.3.4. Preparation of pipettes and electrodes	33
2.3.5. Sign convention	35
2.3.6. Voltage clamp experiments	35
2.3.7. Current clamp experiments	43
2.3.8. Patch-clamp solutions	45
2.3.9. Liquid junction potential	46
2.3.10. Statistical analysis	47
3. Results	49
3.1. The effect of pore mouth of AtTPC1 on voltage and luminal Ca ²⁺ sensing	49
3.1.1. Membrane targeting of the AtTPC1 pore mouth mutants	49
3.1.2. Function of AtTPC1 pore-mouth channel variants	51
3.1.3. Effect of pore mouth mutations on voltage dependency of AtTPC1 channel and luminal Ca ²⁺ sensitivity	54
3.1.4. Effect of AtTPC1 pore mouth mutations on gating charge movement.....	58
3.2. The function of the luminal Ca ²⁺ binding sites in <i>Arabidopsis thaliana</i> and <i>Vicia faba</i>	60
3.2.1. Electrical properties of <i>Vicia faba</i> TPC1	63
3.2.2. The luminal Ca ²⁺ sensor residues in Fabaceae and Brassiceae	72
3.2.3. The function of the VfTPC1 triple mutant N458E/A607E/N608D	83
3.2.4. Effect of pore-mouth amino acids on AtTPC1 channel conductance	85
4. Discussion	88
4.1. Glu605/Asp606 in the pore region of AtTPC1 represents a new luminal Ca ²⁺ binding site	88
4.1.1. AtTPC1-Glu605/Asp606 motif affects the voltage gating	89
4.1.2. The pore motif Glu605/Asp606 contributes to the low tolerance	

of AtTPC1 to high luminal Ca ²⁺	92
4.2. The hyperactivity of the native <i>Vicia faba</i> TPC1 channel is partly related to the loss of luminal Ca ²⁺ sensor Glu605/Asp606	94
4.3. Amino acids Glu605/Asp606 are not involved in determining the TPC1 channel conductivity	95
4.4. High impact of the voltage activation threshold on vacuole excitability	98
4.5. Is VfTPC1 involved in Ca ²⁺ release from vacuole <i>in vivo</i> ?	100
4.6. The possible role of TPC1 in nodule-infected root cells of legumes during nitrogen fixation	102
5. Summary	104
6. Zusammenfassung	106
7. Table list	109
8. Figure list	110
9. Reference	113
10. Glossary	124
11. Curriculum Vitae	127
12. Publication list	128
13. Acknowledgements	129
14. Affidavit in English and German	130

1. Introduction

1.1. The plant vacuole

Vacuoles are the largest compartment in plant cells. The discovery of vacuole by the Dutch scientist Antonie van Leeuwenhoek could be traced back to 1676 (van Leeuwenhoek, 1800) and the term 'vacuole' was coined by the French biologist Félix Dujardin to describe the large empty space within the living cytoplasm of a mature plant cell (Dujardin, 1841). With the aid of microscopy and staining, the plant vacuoles were found to be an acidic environment surrounded by a membrane which De Vries called tonoplast (de Vries, 1885). Technical progress has further enriched the research of plant vacuole. With improvements in microscopy, biochemistry, genetics, and molecular biology, specialized vacuolar compartments have been characterized in the cells of a variety of tissues (Marty, 1999; Shimada *et al.*, 2018). It is now commonly accepted that plant vacuoles can be classified into two types: protein storage vacuoles (PSVs) and lytic vacuoles (LVs). Under certain circumstances, the two types of vacuoles can be converted to each other. For instance, PSVs can turn into LVs during germination whereas in the maturing seeds, LVs can also shift into PSVs (Krüger and Schumacher, 2018).

As indicated by the name, PSVs are used for storage of proteins in storage tissues, such as seeds and fruits (Herman and Larkins, 1999). PSVs are normally marked by seed specific aquaporin α -TIPs (Höfte *et al.*, 1992; Hoh *et al.*, 1995). Compared to LVs, PSVs are less acidic organelles with the capacity to accumulate large amounts of storage proteins as well as defense proteins. The storage proteins are synthesized by the ribosome of the rough endoplasmic reticulum, transported to PSVs in vesicles either after processing in the Golgi apparatus or via a Golgi-independent pathway, where they remain until mobilization during seed germination (Vitale and Hinz, 2005; Vitale and Raikhel, 1999). In seeds PSVs possess crystalloids and globoids, which contain storage

proteins and complex salt crystals such as phytate, respectively (Weber and Neumann, 1980). During seed germination, breakdown of storage proteins released the carbon and nitrogen in reduced state and inorganic minerals such as potassium and calcium as well as phosphor are also released from phytate. By this strategy, it provided numerous nutrient elements that are crucial for embryo development (Weber and Neumann, 1980).

Lytic vacuoles (LVs) are acidic and hydrolytic vacuoles and generally marked by γ -TIP proteins (Höfte *et al.*, 1992; Hoh *et al.*, 1995; Paris *et al.*, 1996; Shimada *et al.*, 2018). LVs have a lot in common with mammalian lysosomes in that they serve as essential digestive compartments. LVs fulfill a broad spectra of important cellular functions (Wink, 1993). One of these is the regulation of turgor pressure, which for example drives cell expansion and thus regulates plant cell growth. They also sequester and store toxic compounds, such as sodium and heavy metal cadmium, to avoid toxic damages of the plant cell and tissue. Large amounts of secondary metabolites are also mainly accumulated in LVs such as phenolic compounds, cyanogenic glycosides or alkaloids, which will be released from the vacuole to defend against microbial pathogens and herbivore (Echeverria and Burns, 1989). Apart from these roles, LVs are important for nutrient supply and ionic homeostasis. The cytosolic nutrients such as K^+ , NO_3^- and PO_4^{3-} must be maintained at a certain level for optimal plant growth. To maintain normal plant growth in the presence of nutrient deficiencies, the cytosolic nutrient pool will be refilled at the expense of the vacuole nutrients (Etxeberria *et al.*, 2012; Isayenkov *et al.*, 2010).

Most plant cells contain a large lytic vacuole which can occupy as much as 90% of the cellular volume (Martinoia *et al.*, 2012). The lytic vacuole is an acidic compartment with a pH mostly around 5.0, surrounded by the cytosol with a pH about 7.5. This low pH in the vacuole lumen results from protons which are pumped from the cytosol into the vacuole by the proton pumps (V-ATPase, V-PPase) under hydrolysis of either ATP or pyrophosphate (PPi) (Fig.1.1) (Gaxiola *et al.*, 2007; Krebs *et al.*, 2010). As a result, the proton motive force

(PMF) is generated that is constituted of a pH gradient of usual 1-2 pH units (Krebs *et al.*, 2010) and a weak tonoplast potential (-10 to -30 mV) is established (Pottosin and Schönknecht, 2007; Walker *et al.*, 1996). The generated PMF provides energy for the transporters for secondary active and passive solute fluxes, such as sugars, cations, organic and inorganic anions. To transport different and specific solutes into or out of the vacuoles, plants express multiple membrane transport proteins such as pumps (e.g. V-ATPase, V-PPase), antiporters (e.g. $\text{Ca}^{2+}/\text{H}^+$ antiporter (CAX)) and ion channels (e.g. SV/TPC1, VK/TPK1 and FV channel, ALMTs) which are targeted to the tonoplast (Fig.1.1; Etxeberria *et al.*, 2012; Isayenkov *et al.*, 2010). Among them, ion channels (e.g. SV/TPC1 channel, FV/TPK1 channel and VK channel) - as one important category of tonoplast transporter - mediate the ion transport down the electrochemical gradient to maintain ion homeostasis (Etxeberria *et al.*, 2012; Isayenkov *et al.*, 2010). In the following, selected vacuolar ion channels will be described in more detail.

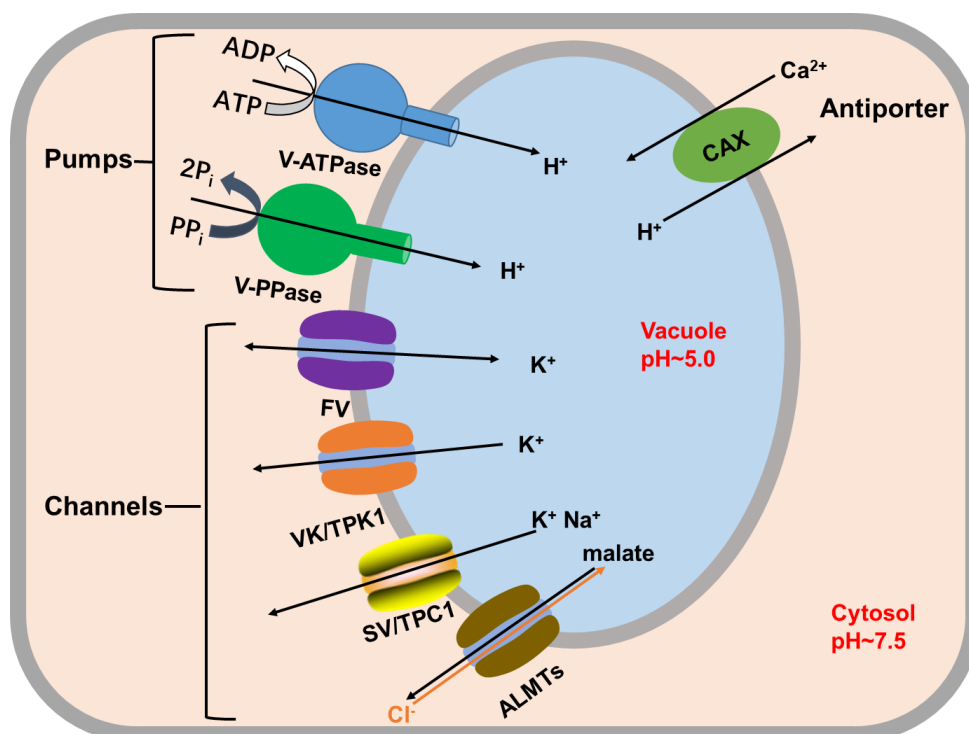


Fig. 1. 1. Schematic representation of the representative pumps, antiporters and ion channels of vacuole transport systems.

V-ATPase: ATP-driven pump for vacuolar H⁺ accumulation; V-PPase: pyrophosphate-driven pump for vacuolar H⁺ accumulation; CAX: H⁺ antiporter (CAX) for Ca²⁺ vacuolar accumulation;

ALMTs: aluminium activated malate transporters for malate and Cl⁻ homeostasis; SV/TPC1: slow vacuolar non-selective cation channel (SV/TPC1) permeable for K⁺ and Na⁺; VK/TPK1: vacuolar K⁺ channel (TPK1) for K⁺ release; FV: fast vacuolar cation channel involved in general cation homeostasis. Image was generated in accordance with (Isayenkov *et al.*, 2010) and (Etxeberria *et al.*, 2012).

1.2. Ion channels of the plant vacuole

As one class of transport proteins, ion channels are pore-forming membrane proteins that allow ions to pass through the channel pore down its electrochemical potential. The amenability of plant vacuoles to the patch-clamp technique has led to the recording of many anion and cation conductance and the characterization of the related ion channels. AtALMT4 and ALMT9 belong to the aluminium activated malate transporter (ALMT) gene family, represent the vacuolar anion channels in Arabidopsis and function as malate- or chloride-permeable anion channel (Eisenach *et al.*, 2017; Kovermann *et al.*, 2007; Meyer *et al.*, 2011). AtALMT4 mediates malate release from the vacuole and is involved in ABA-induced stomatal closure (Eisenach *et al.*, 2017), and AtALMT9 has been characterized as a malate-induced chloride channel that is required for stomatal opening (De Angeli *et al.*, 2013). In comparison, however, most work has been done on vacuolar cation channels. Depending on their kinetics, voltage dependency and cation permeability, vacuolar cation channels can be classified into fast vacuolar (FV) channels, vacuolar K⁺ (VK) channels and slow vacuolar (SV) channels (Hedrich, 2012). Since the gene encoding the FV channel is still unknown, the molecular identification of VK channel as TPKs and SV channel as TPC1 pave the way for in-depth studies of channel structure, regulation and physiological function. Therefore, in the next chapter the FV channel will be described only briefly, while the VK/TPK and SV/TPC1 channels will be presented in more detail.

1.2.1. The fast vacuolar (FV) channel

FV channel was first found in isolated sugar beet vacuoles, where at low Ca^{2+} (10^{-8} M) concentration both depolarizing and hyperpolarizing voltages elicited instantaneously potassium currents (Hedrich and Neher, 1987). In addition to its very fast activation kinetics, FV channel was found to be voltage-dependent. Both cytosolic and vacuolar Ca^{2+} and Mg^{2+} inhibited the activity of FV channel (Brüggemann *et al.*, 1999a; Tikhonova *et al.*, 1997) and polyamines have an inhibitory effect on FV channel (Brüggemann *et al.*, 1998). In regard with the selectivity, FV channel in barley mesophyll vacuole possesses high selectivity of K^+ over Cl^- (Tikhonova *et al.*, 1997). A comprehensive study revealed that FV channel conducted all the tested six monovalent ions with the permeability sequence $\text{NH}_4^+ > \text{K}^+ \geq \text{Rb}^+ \geq \text{Cs}^+ > \text{Na}^+ > \text{Li}^+$ (Brüggemann *et al.*, 1999b). However, till now the coding gene for FV channel is still illusive.

1.2.2. The two-pore K^+ channel TPK

Ward and Schroeder reported firstly the presence of a novel, largely voltage-independent highly K^+ -selective ion channel in the vacuole membrane of *Vicia faba* guard cells (Ward and Schroeder, 1994). It was further demonstrated that this vacuolar K^+ channel type can be activated by physiological increases in the cytoplasmic Ca^{2+} concentration. However, at that time, there was no evidence of the genes encoding this VK channel. Until 2007, AtTPK1 was finally identified and proven to mediate Arabidopsis VK currents in guard cells (Gobert *et al.*, 2007). *tpk1-1* and *tpk1-2* loss-of-function mutants resulted in an absence of the typical instantaneous VK currents, with no effects on the SV currents. The typical VK currents could be restored by transient expression of TPK1-GFP in the genetic background of TPK1-loss-of-function mutant lines *tpk1-1* or *tpk1-2* (Gobert *et al.*, 2007). Therefore, the authors concluded that AtTPK1 encoded a native tonoplast channel that is equivalent to the previously identified VK

conductance (Gobert *et al.*, 2007). The identified AtTPK1 belongs to a small gene family of tandem pore K⁺ channels from the Arabidopsis genome, comprising a total of five TPK isoforms (AtTPK1-5) (Becker *et al.*, 2004; Latz *et al.*, 2007). AtTPK1, 2, 3 and 5 are localized to the tonoplast, whereas AtTPK4 is the only one found to target to the plasma membrane (Becker *et al.*, 2004; Latz *et al.*, 2007; Marcel *et al.*, 2010).

The VK/TPK1 channel (Fig. 1.2) is composed of four transmembrane domains with two pore regions, one N-terminal 14-3-3 binding motif and two EF hands at the C-terminal end (Isayenkov *et al.*, 2010; Marcel *et al.*, 2010). As the name indicated, the N-terminal 14-3-3 binding motif of TPK1 is responsible for interaction with 14-3-3 proteins, the general regulating factors (GRFs). It was found that (i) AtTPK1 could interact with GRF6 upon phosphorylation of a serine residue within the 14-3-3 protein, and (ii) this interaction with the 14-3-3 protein is not involved in trafficking (Dunkel *et al.*, 2008) but (iii) strongly increases the TPK channel activity (Latz *et al.*, 2007). The C-terminal EF hands of TPK1 are thought to be responsible for the Ca²⁺ regulation of the AtTPK1 channel. While TPK2 has two EF-hands and TPK3 has only one EF-hand on the C-terminal domain, TPK4 lacks the C-terminal EF hands which is consistent with its Ca²⁺-independent regulation (Hamamoto *et al.*, 2008). In terms of the ion-permeable pore region, Arabidopsis TPK channels harbor a GYGD sequence in each pore region that defines its K⁺ selectivity. However, the tobacco TPKs does not contain a GYG signature sequence in the second pore region, instead a VHG and GHG motif was present (Hamamoto *et al.*, 2008). Nevertheless, the NtTPK1 has an ion selectivity similar to that of AtTPK1 (Hamamoto *et al.*, 2008). AtTPK1 is involved in many physiological aspects. Using a TPK1 loss-of-function mutant, it was demonstrated that TPK1 plays a very important role in control of intracellular K⁺ homeostasis, affecting the total fresh weight and root growth. The loss of TPK1 function reduced vacuolar K⁺ release and resulted in slow stomatal closure kinetics (Gobert *et al.*, 2007).

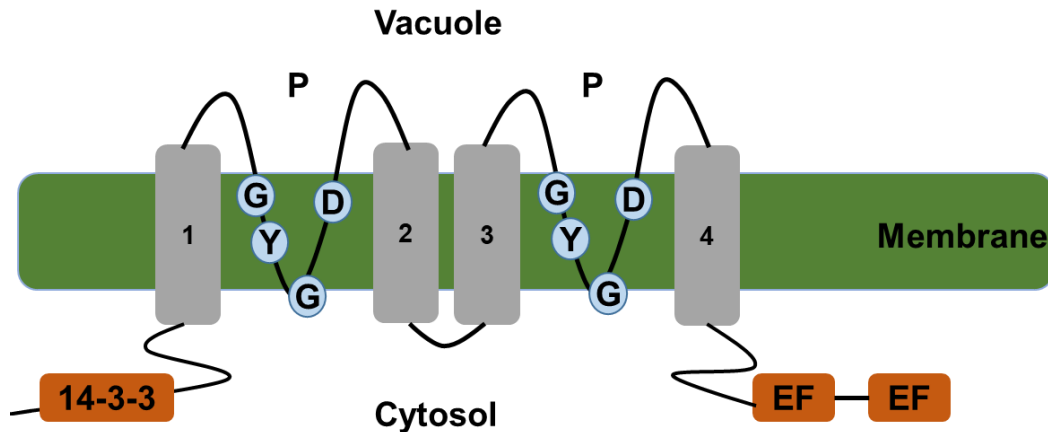


Fig. 1. 2. Schematic representation of the *Arabidopsis thaliana* TPK1 topology.

AtTPK1 is constituted of four transmembrane domains (grey column 1, 2, 3 and 4) with two pore regions (P), one N-terminal 14-3-3 binding motif and two EF hand domains on the C-terminal end. In *Arabidopsis* AtTPK1, each pore region harbors a GYG sequence defining K⁺ selectivity. The image was drawn in accordance with Isayenkov *et al.* (2010).

1.2.3. The non-selective vacuolar cation channel SV/TPC1

1.2.3.1. The plant SV channel is encoded by TPC1

The identification of the SV (Slow Vacuolar) channel could be traced back to 1987 when Hedrich and Neher performed patch-clamp studies on isolated sugar beet vacuoles (Hedrich and Neher, 1987). In this study they showed that the activity of two distinct channel types, the SV and FV channel, can be differentially modulated upon changes in cytosolic Ca²⁺ concentration. When the concentration of cytosolic Ca²⁺ was above 10⁻⁷ M, outward-rectifying currents were monitored which were slowly activated upon membrane depolarization (Hedrich and Neher, 1987). Because of its vacuolar localization and slow activation kinetics, this channel type was named SV (slow vacuolar) channel. Since then, many studies have been conducted on the SV channel. It becomes clear that the SV channel is not only present in all plant organs but also ubiquitously expressed in terrestrial and marine plants, such as sugar beet, *Vicia faba*, seagrass (Carpaneto *et al.*, 1997; Hedrich and Neher, 1987; Schulz-Lessdorf and Hedrich, 1995). In addition, it has been well documented that the

activity of the SV channel could be regulated by several factors, such as Ca^{2+} and Mg^{2+} (Carpaneto *et al.*, 2001; Pottosin *et al.*, 2004), pH (Schulz-Lessdorf and Hedrich, 1995) and redox agents (Carpaneto *et al.*, 1999). In 2005, nearly two decades after its discovery, the single-copy gene AtTPC1 (two-pore channel) was identified as the gene encoding the SV channel in *Arabidopsis thaliana* (Peiter *et al.*, 2005). The AtTPC1 protein was shown to be targeted to the plant vacuole membrane (Peiter *et al.*, 2005) and to conduct the typical SV channel currents observed by Hedrich and Neher in 1987 (Furuichi *et al.*, 2001; Hedrich and Neher, 1987; Peiter *et al.*, 2005). Since then, the molecular identification of AtTPC1 provides a molecular basis for studying the SV channel function and regulation. With the help of modern and advanced biotechnology, several mechanism underlying the control of SV/TPC1 channel activity has been revealed. Therefore, a detailed description of SV/TPC1 is given in the next chapter to provide a comprehensive overview of the current knowledge of SV/TPC1 research.

1.2.3.2. The overall structure of AtTPC1

A functional AtTPC1 channel requires two AtTPC1 polypeptides that assemble to a rectangle-shaped channel dimer, resulting in an overall equivalent tetrameric Shaker-like channel structure (Guo *et al.*, 2016; Kintzer and Stroud, 2016; Peiter *et al.*, 2005). Each AtTPC1 monomer is constituted of 733 amino acids and composed of two Shaker-like domains (DI and DII), each of which contains six transmembrane domains (S1-S6 and S7-S12). Two calcium binding EF hands are present within the cytosolic loop locate between S6 and S7, and two pore regions (P) are found between S5 and S6, and S11 and S12 (Fig 1.3). AtTPC1 has two voltage-sensing domains located in transmembrane domains S4 and S10. However, the transmembrane domain S4 in the first Shaker half (DI) was revealed to contribute less to voltage sensing and thus rather represents a degenerated voltage sensor (Guo *et al.*, 2016; Jašlan *et al.*,

2016). Instead, the major voltage-sensing function was attributed to the transmembrane domain S10 in DII, which contained voltage-sensing arginine residues at positions 537, 540 and 543 (Fig. 1.3) (Guo *et al.*, 2016; Jaślan *et al.*, 2016). Neutralization of these positive S10 charges altered the voltage-dependent gating behavior of AtTPC1.

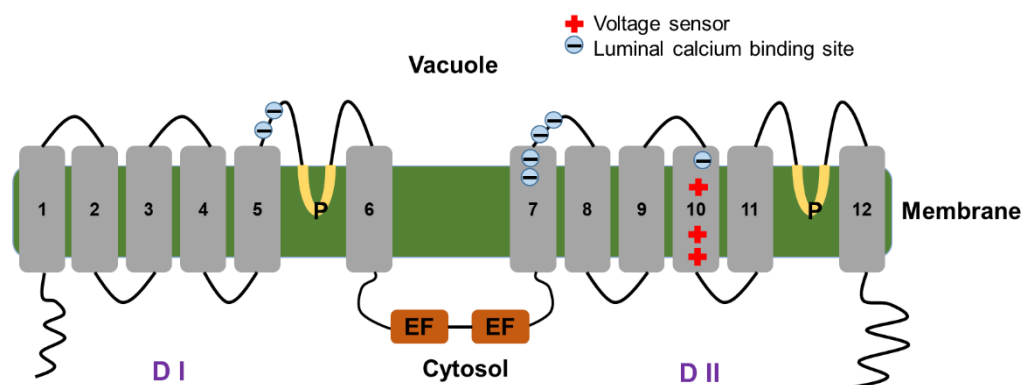


Fig. 1. 3. Schematic representation of the secondary structure of an AtTPC1 subunit.

AtTPC1 comprises two shaker-like domains (DI and DII), each with six transmembrane domains (grey column, S1-S12), two Ca²⁺ binding EF hand domains exposed to the cytosol and two pore-forming regions (P) located between S5 and S6, and S11 and S12. The red '+' in S10 indicates major voltage sensing residues and the circled "-" highlights the residues (Glu239, Asp240, Asp450, Asp454, Glu456, Glu457, Glu528) that are involved in luminal calcium sensing of the channel protein. Image was generated in accordance with Dadacz-Narloch *et al.*, (2013); Guo *et al.*, (2016); Jaślan *et al.*, (2016); Kintzer and Stroud, (2016); Peiter *et al.*, (2005).

1.2.3.3. Ion selectivity of plant SV/TPC1 channel

The SV channel was originally characterized as non-selective cation channel, with permeability not only to K⁺ but also to Na⁺ (Coyaud *et al.*, 1987). SV channels from guard cells of *Allium cepa* showed the following preference for permeating the tested monovalent cations: Na⁺ > K⁺ > Rb⁺ > Cs⁺ (Amodeo *et al.*, 1994). In comparison, SV/TPC1 in *Posidonia oceanica* leaves was equally permeable to K⁺ and Na⁺ whereas in barley mesophyll cells the permeability of K⁺ was 6-times higher than Na⁺ (Carpaneto *et al.*, 1997; Hedrich *et al.*, 1986; Kolb *et al.*, 1987). It also reported that plant SV/TPC1 is not only permeable for monovalent cations but also for divalent cations (Pottosin and Dobrovinskaya,

2014; Pottosin and Schönknecht, 2007). For the SV channels from sugar beet tap roots a relative permeability sequence of $Mg^{2+} < Ca^{2+} \sim Sr^{2+} \sim Ba^{2+}$ was determined (Johannes and Sanders, 1995). Ward and Schroeder (1994) estimated a permeability ratio for Ca^{2+} to K^+ of about 5:1 for SV/TPC1 channels from *Vicia faba* guard cell vacuoles. However, one has to consider that these experiments were performed under artificial solute conditions: 50 mM $CaCl_2$ was applied to the luminal side of the vacuole membrane and 5 mM $CaCl_2$ together with 100 mM KCl to the cytosolic side (Ward and Schroeder, 1994). Guo and colleagues conducted patch-clamp experiments with AtTPC1-transformed HEK cells with 0.3 mM Ca^{2+} and 150 mM Na^+ at the cytoplasmic side and 15 mM Ca^{2+} on the extracytosolic side of the plasma membrane, and calculated a relative permeability ratio of Ca^{2+}/Na^+ of 5 (Guo *et al.*, 2016). This is in well agreement with the permeability ratio of Ca^{2+}/K^+ deduced for the SV/TPC1 from *Vicia faba* guard cell vacuoles (Ward and Schroeder, 1994), considering that Guo *et al.* (2016) also determined a relative permeability ratio of K^+/Na^+ of 1.

1.2.3.4. Modulators of plant SV/TPC1 channel activity

SV/TPC1 channel activity can be modulated by many factors, underpinning the complex structure of the TPC1/SV channel on the one hand and suggesting its networking with multiple regulatory pathways on the other hand. Cytosolic Ca^{2+} and Mg^{2+} have been reported to positively regulate the SV channel activity. During the initial identification and characterization it was already demonstrated that SV channel activation requires cytosolic Ca^{2+} at a concentration above 10^{-7} M (Hedrich and Neher, 1987). As observed in sugar beet vacuoles, cytosolic Mg^{2+} can shift the activation of SV channel to more negative potentials in the concentration range from micromolar to 10 millimolar (Carpaneto *et al.*, 2001). Moreover, cytosolic Mg^{2+} prefers to activate the SV channel in the presence of low cytosolic Ca^{2+} concentration (Carpaneto *et al.*, 2001). This may be due to

the differential affinities of $\text{Ca}^{2+}/\text{Mg}^{2+}$ binding to the EF-hands. According to molecular modelling, EF-I appears to have a low affinity for $\text{Ca}^{2+}/\text{Mg}^{2+}$ binding, while EF-II hand exhibits a high affinity of Ca^{2+} that is crucial for Ca^{2+} -dependent channel activity (Schulze *et al.*, 2011). It was suggested that $\text{Ca}^{2+}/\text{Mg}^{2+}$ binding to EF-I hand has modulatory effects on channel gating but is not essential for channel opening such is Ca^{2+} binding at EF-II hand (Schulze *et al.*, 2011). However, both increased Ca^{2+} and Mg^{2+} concentrations at the luminal side was reported to inhibit the TPC1/SV channel, with the inhibitory effect of Ca^{2+} being stronger than that of Mg^{2+} (Pottosin *et al.*, 2004).

In addition to inhibitory effects of luminal Ca^{2+} and Mg^{2+} , luminal pH and Na^+ also negatively regulate the activity of SV channel. SV/TPC1 channels from sugar beet vacuoles showed a decreased channel activity with rising luminal H^+ concentration (Schulz-Lessdorf and Hedrich 1995). In patch-clamp studies on isolated *Arabidopsis thaliana* cell culture vacuoles, it was observed that an increase in luminal Na^+ to 100 mM shifts the voltage dependence of SV channel to positive voltages (Ivashikina and Hedrich, 2005). However, at the more physiological vacuolar Na^+ (60 mM), the inhibitory effect of luminal Ca^{2+} almost disappeared, resulting in more open SV channels (Pérez *et al.*, 2008). Therefore, it seems that the negative regulation of Na^+ on SV channel is dependent on the concentration of Na^+ and the absence of luminal Ca^{2+} .

Furthermore, N- and C-terminal tails of the SV/TPC1 channel protein represent general regulation sites of the channel activity. Arabidopsis TPC1 harbors a N-terminal dileucine motif (EDPLI), which is conserved among plant TPCs with a consensus sequence of EXXL[LI]. This dileucine motif is required for vacuolar targeting of TPC1 and functions as tonoplast sorting signals of membrane proteins. When this sorting motif was mutated or deleted, TPC1 lost the ability of vacuolar targeting and was redirected to the plasma membrane (Larisch *et al.*, 2012). Additionally, a N-terminal KAAAL domain that is predicted to form an α -helical secondary structure also ensures efficient vacuolar trafficking of AtTPC1 channel (Larisch *et al.*, 2012). In comparison, the C-terminal region of

Arabidopsis TPC1 with amino acids 703-723 forms a highly stable, antiparallel dimer with characteristics of a coiled-coil. The dimerization of this region within the C-terminus (CTH) provides the structural basis for TPC1 function (Larisch *et al.*, 2016).

1.2.3.5. Cytosolic Ca²⁺ activation site

As well documented in the 80ties (Hedrich *et al.*, 1986; Hedrich and Neher, 1987), in plants the activation of SV/TPC1 channel requires cytosolic Ca²⁺. Based on the TPC1 sequence information (Peiter *et al.*, 2005), it was suggested that two calcium-binding EF hands located in the loop between S6 and S7 at the cytosolic side are likely responsible for Ca²⁺ activation of SV/TPC1 channel. Inspired by that, Schulze and colleagues used site-direct mutagenesis to understand the molecular mechanism of the Ca²⁺-dependent activity of AtTPC1. Asp was replaced by Ala at the position of EF-I (D335A), EF-II (D376A) and in both EF-I and EF-II (D335A/D376A) (Schulze *et al.*, 2011). Although the characteristic of Ca²⁺-dependent activation was preserved, TPC1-D335A mutation showed reduced Ca²⁺ sensitivity. In contrast, double point mutation TPC1-D335A/D376 and single TPC1-D376A mutation in EF-II hand totally abolished ion conductance of the channel. These suggested that the Ca²⁺-dependent channel opening is mainly modulated by EF-II and EF-I seems not directly involved in, but probably modulates Ca²⁺ dependent activation and the activity of EF-II (Schulze *et al.*, 2011). When the crystal structure of AtTPC1 was revealed, it surprisingly showed that only the first EF hand conveys a canonical Ca²⁺-bound EF-hand structure, while the second EF hand adopts an apo state, probably owing to a lower Ca²⁺ affinity (Guo *et al.*, 2016; Kintzer and Stroud, 2016). However, in the recent review by Hedrich *et al.* (2018), a closer inspection showed an invariant glycine residue in the second EF hand is replaced by phenylalanine and this may result in variation of EF-hand motif (Hedrich *et al.*, 2018). Thus, whether the second EF hand is able to bind Ca²⁺

still remains unclear. Since the C-terminal end of S6 is an integral part of the E1 helix of the first EF hand, the binding of Ca^{2+} to EF-I hand will be directly coupled to IS6 and finally alter the pore segment movement (Capozzi *et al.*, 2006; Guo *et al.*, 2016). This might be the possible activation mechanism of cytosolic Ca^{2+} .

1.2.3.6. Luminal Ca^{2+} inhibition site

In contrast to activating cytosolic Ca^{2+} , luminal Ca^{2+} was reported to inhibit the SV/TPC1 channel (Pottosin *et al.*, 2004; Pottosin *et al.*, 1997). An increase from 0.1 to 1.0 mM calcium at the luminal side of the vacuole membrane resulted in a decreased SV/TPC1 channel activity in *Beta vulgaris* (Pottosin *et al.*, 2004). A similar effect on TPC1 was observed in other species. In *Arabidopsis thaliana* vacuoles, almost no wild-type SV/TPC1 currents were recorded at high luminal Ca^{2+} concentration of 10 mM (Dadacz-Narloch *et al.*, 2011; Lenglet *et al.*, 2017). However, screening of ethyl-methansulfonate mutants for individuals impaired in wounding-induced jasmonate biosynthesis identified the *Arabidopsis* AtTPC1 channel mutant *fou2*. The *fou2* channel mutant harbors a point mutation of Asp454 which was replaced to asparagine (D454N) (Bonaventure *et al.*, 2007a; Bonaventure *et al.*, 2007b). Electrophysiological studies of the *fou2* channel properties revealed that D454N/*fou2* is insensitive to inhibitory luminal Ca^{2+} and renders SV channel more hyperactive (Beyhl *et al.*, 2009). Based on the first structural 3D model, Dadacz-Narloch and co-authors proposed that the Asp454 mutated in *fou2* is located at the luminal side of the channel protein and is part of a luminal Ca^{2+} binding site that mediates the luminal inhibitory Ca^{2+} effect on SV channel within *fou2* mutation (Dadacz-Narloch *et al.*, 2011). In addition, the acidic residue Glu450 was proposed to be also directly involved in Ca^{2+} coordination, while Glu456, and Glu457 was suggested be indirectly involved in luminal Ca^{2+} sensing (Dadacz-Narloch *et al.*, 2011). To test these suggestions experimentally, several site-directed channel mutants were

generated by replacing these Glu, Asp residues to Gln, Asn, respectively. Transient expression of these channel mutants in the background of the TPC1 loss-of-function mutant *attpc1-2* allowed to record the SV channel responses to luminal Ca^{2+} . According to these results, Glu450 and Asp454 contribute to the direct luminal calcium binding sites of TPC1, while Glu456 and Glu457 rather connect the luminal Ca^{2+} binding site to the channel gate (Dadacz-Narloch *et al.*, 2011). Again, the importance of residue Asp454 was confirmed when the crystal structure of AtTPC1 was resolved (Guo *et al.*, 2016; Kintzer and Stroud, 2016). It showed that Asp454 together with Glu528 and Asp240 forms the luminal Ca^{2+} binding site 1, and mutation of these residues profoundly reduced luminal Ca^{2+} inhibition, suggesting their critical role for luminal inhibition by Ca^{2+} ions. Apart from that, the crystal structure of AtTPC1 revealed the existence of a second luminal Ca^{2+} binding site 2 (Glu239, Asp240 and Glu457). Since the mutation of E239Q did not significantly affect luminal Ca^{2+} sensing, the authors suggested that Ca^{2+} binding site 1, rather than 2, is the most important (Guo *et al.*, 2016). In contrast to Guo *et al.* 2016, Jaślan and co-authors, however, reported that E239Q mutation resulted in the loss of vacuolar Ca^{2+} sensitivity (Jaślan *et al.*, 2016). The discrepancy in the two studies may be caused by the different expression systems they used. In Guo *et al.* (2016), AtTPC1 was expressed in a heterologous human HEK293 cell line in which AtTPC1 was mis-targeted to the plasma membrane (Guo *et al.*, 2016). In Jaślan *et al.* (2016), the homologous Arabidopsis mesophyll protoplasts was used for transient expression of AtTPC1, preserving the normal targeting of AtTPC1 to the vacuole membrane (Jaślan *et al.*, 2016). Therefore, the mis-targeting of AtTPC1 to the plasma membrane (Guo *et al.*, 2016) may lead to the different TPC1 channel features observed in those two studies. Taken together, seven negative charged amino acids in AtTPC1 channel are proved to be involved in luminal Ca^{2+} sensing, including E239, D240, E450, D454, E456, E457 and E528 (cf. Fig. 1.3). Interestingly, based on the crystal structure analysis, Kintzer and Stroud predicted that at the luminal pore mouth two other negative amino

acid residues, such as Glu605 and Asp606, are probably able to coordinate luminal Ca^{2+} (Kintzer and Stroud, 2016).

1.2.3.7. The physiological functions of SV/TPC1

As mentioned above, the Arabidopsis SV channel is encoded by the unique gene AtTPC1 (Furuichi *et al.*, 2001; Peiter *et al.*, 2005). The molecular identification of AtTPC1 enables to study the physiological function of SV channel by modulating the expression of AtTPC1. Surprisingly, the TPC1 loss function *attpc1-2* mutant did not result in any pronounced growth and developmental phenotype (Peiter *et al.*, 2005). However, the AtTPC1 gain-of-function mutation *fou2*, equipped with a hyperactive TPC1 channel, showed a retarded growth phenotype which contains a higher level of JA compared with wild type plants (Bonaventure *et al.*, 2007a; Bonaventure *et al.*, 2007b). With such high JA level, *fou2* plants shown an enhanced defense capacity against fungal or herbivore attacks (Bonaventure *et al.*, 2007a; Lenglet *et al.*, 2017). Furthermore, the *fou2* plants also rises several-fold JA levels in response to wounding compared to wild-type plants (Bonaventure *et al.*, 2007a). Therefore, TPC1/SV channel involved in jasmonate acid (JA) signaling. In addition, TPC1/SV was reported increase whole-plant salt tolerance. Under salt treatment, the AtTPC1 overexpression plants showed higher salt tolerance, while the growth of the *tpc1-2* mutant plants was impaired, compared with wild type plants (Choi *et al.*, 2014). Apart from salinity stress, TPC1 was also reported to involve in low temperature, H_2O_2 , drought and osmotic stress response (Behringer *et al.*, 2015; Kawano *et al.*, 2004; Lin *et al.*, 2005; Wang *et al.*, 2005). In addition, TPC1 was reported to regulate external Ca^{2+} -induced stomata closure. Lack of TPC1 protein reduced stomatal closure in response to high external Ca^{2+} loads (Peiter *et al.*, 2005), and overexpression of TaTPC1 in *Arabidopsis thaliana* promoted external Ca^{2+} -induced stomatal closure (Wang *et al.*, 2005).

1.3. Objective of the work

Different types of ions such as potassium and calcium play important roles in plant performance. In plants, the vacuole is an important subcellular compartment for ion storage that can influence the cellular ion homeostasis. For uptake into the vacuole or release from this compartment, ions have to pass the vacuole membrane via specialized transport proteins. In the vacuole membrane, the TPC1/SV channel is one prominent cation channel. In the past, the structure and functional domains of TPC1 in the model plant *Arabidopsis thaliana* was thoroughly studied. Two luminal Ca²⁺ binding sites (site 1: Asp240, Asp454, Glu528; site 2: Glu239, Asp240, Glu457) have been reported to be involved in the sensitivity of TPC1 to inhibitory luminal Ca²⁺. Beyond these Ca²⁺ binding sites 1/2, based on crystal structure analysis, scientists proposed that two other amino acids in the luminal pore mouth, Glu605 and Asp606, can probably also coordinate luminal calcium ion (Kintzer and Stroud, 2016). However, at the beginning of this thesis, evidence for this was still awaited. Thus, one goal of this work was to examine in patch-clamp experiments with appropriate channel mutants whether Glu605 and Asp606, and possibly also the nearby negatively charged amino acid Asp607 contribute to a third luminal Ca²⁺ sensing site in higher plants.

Moreover, TPC1/SV channel currents from *Vicia faba* were still recorded under very high luminal Ca²⁺ conditions (Ward and Schroeder 1994), at which TPC1/SV currents from *Arabidopsis thaliana* should already be suppressed (Dadacz-Narloch *et al.*, 2011). Does it mean that the luminal Ca²⁺ sensitivity and luminal Ca²⁺ binding sites of TPC1 channels might be different in these two plant species? Amino acid sequence alignments of these TPC1 channel types revealed that the amino acid residues of the luminal Ca²⁺ binding site 1 are very conserved while polymorphic residues are present at site 2 and potential site 3. Therefore, as a second objective, electrophysiological studies using *Arabidopsis thaliana* and *Vicia faba* channel mutants should provide

information on whether these natural TPC1 channel variants exhibit differences in luminal Ca^{2+} sensitivity and luminal Ca^{2+} binding sites.

2. Materials and methods

2.1. Generation of TPC1 constructs

The TPC1 constructs used in this study were generated by using the cloning technique UserTM method (uracil-specific excision reagent) (Nour-Eldin *et al.*, 2006).

2.1.1. User primer design

To generate the plasmids harboring the different TPC1 channel constructs used in this work, User primers were designed. All User primers used in this thesis are shown in Table 2.1. User primers for VfTPC1-WT (WT: wild type) have been designed by Dr. Dawid Jaslan from the group of Prof. R. Hedrich (University of Würzburg).

Table 2. 1. Primers used in this work.

Name	Sequence (5'- 3')
AtTPC1-E605Q fwd	ACAGGATGACUACCTTTTGTTCAACTTCAATGAC
AtTPC1-E605Q rev	AGTCATCCTGUGCCAATTCGGTTTCAAAGAG
AtTPC1-E605A fwd	ATTGGCTGCGGAUGACTACCTTTTGTTC AAC
AtTPC1-E605A rev	ATCCGCAGCCAAUTCGGTTTCAA
AtTPC1-D606N fwd	AGAGAATGACUACCTTTTGTTCAACTTCAAT
AtTPC1-D606N rev	AGTCATTCTCUGCCAATTCGGTTTCAAAGAG
AtTPC1-D607N fwd	AGAGGATAATUACCTTTTGTTCAACTTCAATGAC
AtTPC1-D607N rev	AATTATCCTCUGCCAATTCGGTTTCAAAGAG
AtTPC1-EDD tr fwd	ACAGAACAATUACCTTTTGTTCAACTTCAATGAC
AtTPC1-EDD tr rev	AATTGTTCTGUGCCAATTCGGTTTCAAAGAG
VfTPC1-WT User fwd	GGCTTAAUATGACGGAGCCTCTACTCAGAG
VfTPC1-WT User rev	GGTTTAAUCCTGTACTGGAAGGATGATTTTGACAAA
VfTPC1-A607E/N608D fwd	AGAGGATGACUATTTACTTTTTAATTTCAATG
VfTPC1-A607E/N608D rev	AGTCATCCTCUGCAAGGTCTGTGGCCTCCA
VfTPC1-N459E fwd:	AAGAGAGTTCUGCTCAAAGGCTTGG
VfTPC1-N459E rev:	AGA ACTCTCTUCTATGTGCGAGCGTTGTCTCAA

fwd: forward primer, rev: reverse primer. AtTPC1-double: E605A/D606N, AtTPC1-triple: E605A/D606N/D607N, VfTPC1-triple: N459E/A607E/N608D.

For generation of the AtTPC1 and VtTPC1 mutant constructs, primers were designed that spanned the site of mutagenesis and altered the DNA sequence to produce the desired base pair and in turn amino acid changes (Fig. 2.1). Primer pairs carried the desired mutation between adenosine (A) and thymidine (T). The T nucleoside of the User primers was replaced by an uracil (U). The site of mutagenesis was located within the User tail region.

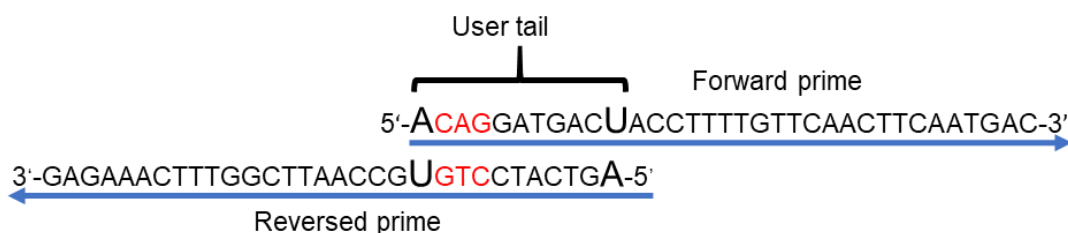


Fig. 2. 1 The principle of generation of point mutation with overlapping User primers.

As an example, base pairs between A and U highlighted in red in the User tail were exchanged to trigger a point mutation in the amino acid sequence.

2.1.2. PCR reaction

The polymerase chain reaction (PCR) was used to replicate specific DNA fragments *in vitro* (Mullis *et al.*, 1986). Within one cycle of the PCR, three different PCR steps took place. During the first step of heat denaturation of the double-stranded DNA, the hydrogen bonds between the two DNA strands were dissolved. If the temperature was subsequently lowered (step 2), the primers were able to attach to the individual DNA strands (primer hybridization). The primers were oligonucleotides that were complementary to the template DNA and served as starting points for the PCR. In the last step, the DNA polymerase filled the strands with free nucleotides, starting at the 3' end of the primer (elongation). By repeating this cycle several times, the desired DNA sequence was amplified. In the context of this work, the following standard approach (Table 2.2) was used for the PCR reaction.

Table 2. 2. PCR reaction (50 µl) standard.

Components	Volume (50 µL)
Reactions buffer (5x)	10 µL
dNTPs (10 mM)	1 µL
Forward primer (10 µM)	1 µL
Reverse primer (10 µM)	1 µL
DNA-Polymerase (0.25 U)	1 µL
DNase free H ₂ O	35 µL
Template	1 µL

The PCR reactions were carried out in the Eppendorf Mastercycler machine (Eppendorf AG, Hamburg, Germany). The following standard conditions were chosen:

Initial denaturation	2 min	98 °C	
Denaturation	30 sec	98 °C	} 30x
Primer hybridization	30 sec	55 °C	
Elongation	2 min	72 °C	
Final elongation	3 min	72 °C	

2.1.3. Subcloning of TPC1-WT channel variants

The two TPC1 wild type constructs 35S::AtTPC1-WT (Dadacz-Narloch *et al.*, 2011) and 35S::VfTPC1-WT (generated by Dr. Dawid Jaslan) were already available at the beginning of this thesis. These wild-type channel coding sequences were inserted into the modified pSAT6-eGFP-C1 vector so that the TPC1 channel was under the control of the 35S promoter and fused at its C-terminus to eGFP (Cormack *et al.*, 1996). However, after *attpc1-2* protoplasts were transiently transformed with the 35S::VfTPC1-WT construct, the transformation efficiency was too low for subsequent patch-clamp experiments. Therefore, the VfTPC1-WT coding sequence was subcloned into the vector pSAT6-eYFP-C1 with UBQ10 promoter because proteins were proven to be more stably expressed under the UBQ10 promoter than under the 35S promoter (Grefen *et al.*, 2010). For this, first the pSAT6-eYFP-C1 vector was

linearized by enzymatic digestion with *PacI* (Table 2.3) and *NtBbvCI*.

Table 2. 3. Standard *PacI* enzyme digestion.

Components	Volume (200 μ L)
Vector	40 μ L
Buffer NEBI (Fermentas, Waltham, USA)	20 μ L
<i>PacI</i> (Fermentas, Waltham, USA)	7 μ L
DNase free H ₂ O	133 μ L

The reaction of *PacI* enzyme alone (Table 2.3) was carried out overnight at 37 °C. After overnight incubation, 2 μ L *PacI* and 4 μ L *NtBbvCI* were added to the *PacI* reaction for 6-8 h at 37 °C. Then, the linearized vector was generated. In the following, the VfTPC1-PCR fragments which have been amplified with VfTPC1-WT User fwd/rev primers, were inserted into the linearized vector using the User enzyme. For this, the standard User enzyme reaction was carried out as shown in Table 2.4, the reaction was firstly incubated at 37 °C for 25 min and then at 25 °C for further 25 min. At the end, the new pSAT6-eYFP-C1 vector construct with UBQ10::VfTPC1-eYFP was generated.

Table 2. 4. Standard User enzyme reaction.

Components	Volume (10 μ L)
PCR product	4 μ L (approx. 400 ng)
Linearized vector	1.5 μ L
User TM enzyme (New England Biolabs, Ipswich, USA)	1 μ L
DNase free H ₂ O	3.5 μ L

2.1.4. Site-directed mutagenesis

To introduce point mutations to the AtTPC1-WT and VfTPC1-WT channel protein at specific sides, the complete DNA plasmid containing the coding sequence of either AtTPC1-WT (pSAT6-eGFP-C1 vector) or VfTPC1-WT (pSAT6-eYFP-C1 vector) were used as DNA template for PCR using special User primer pairs shown in Table 2.1. Two separate PCR amplification

processes were basically performed: PCR 1 with the forward primer (black arrow) and the reverse mutagenesis primer (blue arrow), and PCR 2 with the complementary forward mutagenesis primer (blue arrow) and the reverse primer (black arrow) (Fig. 2.2). After the two PCR reactions, the parental plasmids in the PCR1 and 2 assays were destroyed by DPN1 enzyme (Table 2.5) at 37°C for 30 min. Then, PCR1 and PCR2 products were ligated by User enzyme reaction (Table 2.4) to form the new construct containing the point mutations. The detailed information of all TPC1-WT and TPC1 mutants used in this study are shown in Table 2.6.

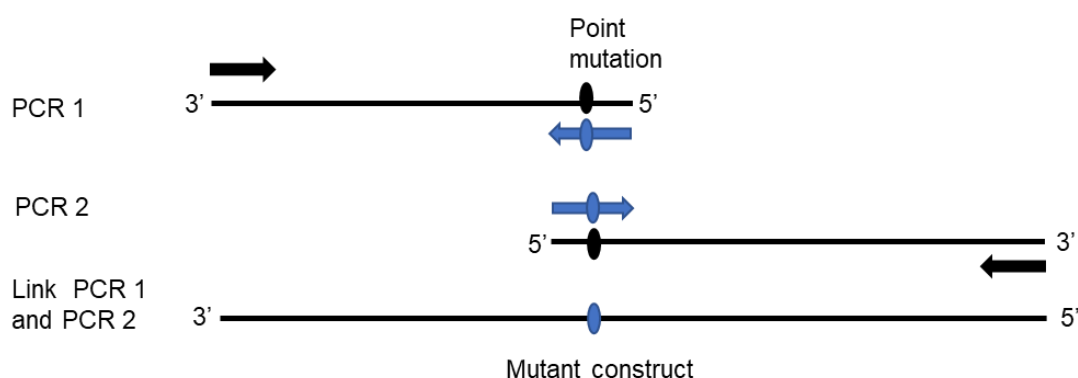


Fig. 2. 2. Principle cloning procedure for the generation of site-directed mutagenesis constructs. See details in the main text.

Table 2. 5. Standard DPN 1 enzyme digestion.

Components	Volume (10 μ L)
User reaction product	8 μ L
10X Buffer Tango (Thermo Scientific, Waltham, USA)	1 μ L
DPN 1 (Thermo Scientific, Waltham, USA)	1 μ L

Table 2. 6. Components of the DNA plasmids used in this study.

Channel variant	Promoter	C-terminal reporter	Resistance	Used vector
AtTPC1-WT	35S promoter	eGFP	Ampicilin	pSAT6-eGFP-C1
AtTPC1-E605Q	35S promoter	eGFP	Ampicilin	pSAT6-eGFP-C1
AtTPC1-E605A	35S promoter	eGFP	Ampicilin	pSAT6-eGFP-C1
AtTPC1-D606N	35S promoter	eGFP	Ampicilin	pSAT6-eGFP-C1
AtTPC1-D607N	35S promoter	eGFP	Ampicilin	pSAT6-eGFP-C1
AtTPC1-double	35S promoter	eGFP	Ampicilin	pSAT6-eGFP-C1
AtTPC1-triple	35S promoter	eGFP	Ampicilin	pSAT6-eGFP-C1
VfTPC1-WT	35S promoter	eGFP	Ampicilin	pSAT6-eGFP-C1
VfTPC1-WT	UBQ 10 promoter	eYFP	Ampicilin	pSAT6-eYFP-C1
VfTPC1-triple	UBQ 10 promoter	eYFP	Ampicilin	pSAT6-eYFP-C1

2.1.5. Bacterial transformation by heat shock

In the following *Escherichia coli* competent cells (strains MRF' or JM101') were transformed with the respective vector constructs shown in Table 2.6. Plasmid DNA (2 µL) was added to melted aliquot (50 µl) of *E. coli* competent cells, mixed and heated at 42 °C for 50 s. After incubating on ice for 3 min, the suspension was plated on 50 µg/mL ampicillin-containing LB agar plate (Table 2.7) at 37 °C overnight. As result, only bacteria harboring the plasmid with an ampicillin resistance were grown. An individual bacterial colony was then selected and incubated overnight on a shaker (New Brunswick Scientific Innova 4230 Incubator) in 5 ml LB medium (Table 2.8) with 50 µg/mL ampicillin at 37 °C.

Table 2. 7. Components of LB agar plate.

Components	Amount
Trypton (Applichem GmbH, Germany)	10 g
Yeast extract (Applichem GmbH, Germany)	5 g
Sodium chloride	10 g
Agar	15 g
de-ionized H ₂ O	To 1 L

Table 2. 8. Components of LB medium.

Components	Amount
Trypton (Applichem GmbH, Germany)	10 g
Yeast extract (Applichem GmbH, Germany)	5 g
Sodium chloride	10 g
de-ionized H ₂ O	To 1 L

2.1.6. Isolation and sequencing of plasmids

Alkaline lysis was used to extract the plasmids from the overnight *E. coli* culture (section 2.1.5). For this, 1.5 ml bacterial liquid culture was collected and used for centrifugation (10000 × *g*, 1 min). After discarding the supernatant, the pellet was resuspended in a small amount of LB medium (approx. 50 µL). By adding 400 µL Lysis buffer (Table 2.9), on the one hand the cells were disrupted. On the other hand, the denaturing properties of the buffer caused the double strands of the chromosomal DNA to be completely denatured, while the plasmid DNA remained unchanged. Then, when 200 µL 3 M sodium acetate (pH 5.2) was added, the chromosomal DNA and bacterial protein formed a complex and precipitated by centrifugation (10000 × *g*, 5 min), while the soluble plasmid DNA was enriched in the supernatant. By transferring the plasmid-containing supernatant into 800 µL isopropanol, the plasmid DNA precipitated by centrifugation at 4 °C (10000 × *g*, 5 min). After the pellet was washed with 500 µL of 70% ethanol and dried at 37 °C, the pellet was resuspended in 50 µL DNase-free H₂O and the constructs were sent to sequence. Construct sequencing was carried out by the company GATC Biotech AG (Constance, Germany), and sequence data were verified using the VectorNTI program (Invitrogen, InforMax, Karlsruhe). The verified constructs were stored at -80 °C. For further amplification, the bacterial colony culture containing the correct vector construct was cultivated in 120 ml LB / ampicillin medium for 16 hours overnight at 37 °C with continuous shaking at 180 rpm (New Brunswick Scientific Innova 4230 Incubator).

Table 2. 9. Components of lysis buffer.

Components	Amount
TE-buffer (10 mM Tris-HCl and 1 mM EDTA, pH 7.5)	9.4 mL
10 % SDS	500 μ L
10 M NaOH	100 μ L
10 mg/mL RNase (Thermo Scientific)	200 μ L

2.1.7. Isolation of midi plasmid-DNA for transient protoplast transformation

The transformed *E. coli* overnight cultures were centrifuged at $6,000 \times g$ and 4°C for 15 min. According to the company instructions, the high-yield QIAGEN Plasmid Plus Midi Kit (QIAGEN, Hilden, Germany) was used for isolation of plasmids required for the transient protoplast transformation (section 2.2). The obtained DNA was dissolved in deionized water, and the light absorbance (OD) of the sample was measured at wavelengths around 260 nm and 280 nm with a spectrophotometer (NanoDrop Products, Wilmington, USA). DNA concentration was calculated by light absorbance at 260 nm, while the ratio of OD_{260 nm} and OD_{280 nm} allowed to determine the purity of the isolated DNA.

2.2. Transient transformation of mesophyll protoplasts

2.2.1. Plant materials and growth condition

Arabidopsis thaliana loss-of-function-plants *tpc1-2* (Peiter *et al.*, 2005) were grown on soil (Special professional, Einheitserdewerke Patzer PATZER ERDEN GmbH, Germany) in plastic pots of 7 cm diameter under controlled short-day conditions in a climate chamber. The temperature was constantly hold at 22°C and 16°C during the light and dark period, respectively. Plants were illuminated for 8 hours with a light intensity of $150 \mu\text{mol s}^{-1} \text{m}^{-2}$ using fluorescent lamps from Osram (L58W/77 FLUORA; Munich, Germany) and

Philips (TLD 58W/840; Hamburg, Germany). Air humidity was maintained at 60%. The experiments were carried out with plants which were 5 to 6 weeks old.

2.2.2. Preparation of fresh enzyme solution

For enzymatical isolation of the mesophyll protoplasts (section 2.2.3), the enzyme solution was freshly prepared for each preparation. After 2 mL 0.2 M MES stock solution (pH 7.5) was heated at 60 °C for 3-5 min, 0.08 g macerozyme (Yakult Pharmaceutical Ind. Co., Ltd., Japan) and 0.3 g cellulase (Yakult Pharmaceutical Ind. Co., Ltd., Japan) was added and mixed for 2-3 min at room temperature. In the following, 0.2 mL of 2 M KCl stock solution and 10 mL Mannitol of 0.8 M stock solution were additionally added to the enzyme solution and mixed for 2-3 min. The mixed solution was heated again at 60 °C for 10 min. After cooling down to room temperature, 0.2 mL CaCl₂ (1 M stock) and 0.2 g bovine serum albumin fraction V (BSA, pH 7.0) (Applichem GmbH, Germany) were dissolved in the mixture solution, and after filtration through a 0.45 µm sterile filter (Sartorius Lab Instruments GmbH & Co. KG, Germany) the enzyme solution was ready for isolation of protoplasts.

2.2.3. Enzymatical isolation of mesophyll protoplast

In this study an adapted protocol according to Yoo *et al.* (2007) was used to isolate *Arabidopsis thaliana* mesophyll protoplasts for transient transformation. Briefly, the lower epidermis of mature *Arabidopsis* leaves (about 30 from 6-7 plants) was gently scrubbed using P1200 sandpaper (Matador, Slovakia). Then, the scrubbed leaf surface was placed on the enzyme solution in the petri dish, so that the lower epidermis was in contact with the enzyme solution (Table 2.10) for cell wall degradation. After incubation in the dark for 3 h, the sample was filtered through a W5-moistened nylon mesh of pore size 50 µm with 35 mL W5

solution (Table 2.11). The filtrate was centrifuged at $100 \times g$, $4 \text{ }^{\circ}\text{C}$ for 2-3 min without brake and acceleration. After discarding the supernatant, the pellet with the protoplasts was resuspended in 5-10 mL W5 solution and incubated on ice for 30 min. The supernatant was then carefully removed with a pipette, and the protoplast-enriched precipitate was resuspended in approximately 5 mL MMG solution (Table 2.12). The protoplast suspension was stored at room temperature and ready for transient transformation.

Table 2. 10. Components of enzyme solution.

Components	Concentration
CellulaseR-10 (Yakult, Tokyo, Japan)	1.5% (weight /volume)
MazerozymeR-10 (Yakult, Tokyo, Japan)	0.4%(weight /volume)
CaCl ₂	10 mM
Mannitol	0.4 M
KCl	20 mM
BSA fraction V, pH 7.0 (Applichem GmbH, Germany)	0.1% (weight /volume)
MES adjusted to pH 5,6 with Tris	20 mM

Table 2. 11. Components of W5 solution.

Components	Concentration
MES (pH 5.7)	2 mM
NaCl	154 mM
CaCl ₂	125 mM
KCl	5 mM
Glucose	5 mM

Table 2. 12. Components of MMG solution.

Components	Concentration
MES (pH 5.7)	4 mM
Mannitol	0.4 M
MgCl ₂	15 mM

2.2.4. PEG-based protoplast transformation

20 μg plasmid DNA was gently mixed with 200 μL mesophyll protoplast

suspension (section 2.2.3) and 220 μL PEG solution (Table 2.13). After incubation for 15 min at room temperature, 440 μL W5 solution was added to the suspension and incubated for additional 2 min. Then, 880 μL W5 solution was added to the suspension and mixed gently. After centrifugation at $100 \times g$ and $4\text{ }^{\circ}\text{C}$ for 1 min without brake and acceleration, the supernatant was removed, and the pellet was resuspended in 1.5 mL W5 solution. After adding 2 μL 50 mg/mL ampicillin, the transformed protoplast suspension was usually incubated for two days at room temperature in the dark before being used for patch-clamp experiments.

Table 2. 13. Components of the PEG solution.

Components	Amount
PEG 4000 (Sigma-Aldrich, Darmstadt, Germany)	2 g
0.8 M Mannitol	1.25 mL
1 M CaCl_2	0.5 mL
H_2O	1.5 mL

2.2.5. Vacuole isolation

Two days after transformation an aliquot of the transiently transformed protoplast suspension (50 μL) was transferred to the patch-clamp recording chamber (chamber volume approx. 600 μL) containing 200 μL vacuole-releasing (VR) solution. The VR-solution used by Lagostena *et al.* (2017) was slightly modified and consisted of 100 mM malic acid, 155 mM NMDG (N-methyl-Dglucamine), 5 mM EGTA, 3 mM MgCl_2 , 10 mM Hepes/Tris pH 7.5 and was adjusted to $450\text{ mOsmol}\cdot\text{kg}^{-1}$ with D-sorbitol. High-resistance membrane seals with liberated vacuoles were generally formed in VR solution. After the establishment of the whole-vacuole configuration in the VR solution, the VR solution was exchanged by the patch-clamp bath solution (section 2.3.8).

2.2.6. Fluorescent imaging of channel expression

In order to verify the successful transformation, expression and subcellular localization of the different eGFP- or eYFP-tagged TPC1 channel variants, eGFP/eYFP fluorescence images of transiently transformed protoplasts and isolated vacuoles were acquired with a confocal laser scanning microscope (TCS SP5; Leica, Mannheim, Germany). eGFP and eYFP were excited with an Argon laser at 490 and 514 nm, respectively, and the emission of fluorescence was recorded between 500 and 520 nm for eGFP and between 520–540 nm for eYFP. Red autofluorescence of chlorophyll was excited at 540 nm with emission and acquired between 590 and 610 nm.

To identify transformed vacuoles for patch-clamp experiments, a *precisExcite HighPower* LED lamp (Visitron Systems GmbH, Puchheim, Germany) was used to excite eGFP and eYFP fluorescence at 480 nm. Emission of fluorescence was measured between 510 and 535 nm and indicated transformed vacuoles within the released vacuole population.

2.3. Electrophysiology

2.3.1. Patch-clamp technique

Ionic current signals within and between cells are mediated by ion channels, ion pumps or electrogenic carriers embedded in membranes of all cells. These types of membrane currents can be measured with the patch-clamp technique invented by Erwin Neher and Bert Sakmann. In 1991 these researchers received the Noble prize in Physiology/Medicine for their pioneering innovation. In comparison to other electrophysiological techniques, the essential advance of this technology was the strong reduction of the previously very large background currents during the current measurements (Hamill and Sakmann, 1981; Neher and Sakmann, 1976a, b). As a result of the high signal-to-noise

ratio, since then it is possible to resolve and to record currents even in the low pA-range which are mediated by individual single ion channels in small membrane areas *in vivo*. The patch-clamp technique is not only used in animal cells, but also serves for the electrophysiological characterization of active and passive membrane transport processes in plant membranes (Hedrich *et al.*, 1989; Hedrich and Neher, 1987; Hedrich and Schroeder, 1989; Hedrich, 2012; Rienmüller *et al.*, 2012; Schulze *et al.*, 2011).

2.3.2. Patch-clamp configurations

Depending on the experimental objective, the patch-clamp technique can be used to measure the membrane currents in four different configurations (Fig. 2.3). To establish the first measuring configuration, the so-called “cell-attached” configuration, the glass microelectrode (patch pipette) is placed on the target membrane of a single cell or an internal compartment such as the vacuole. The tip diameter of the glass microelectrode is around 1-2 μm which may, however, vary depending on the used patch-clamp configuration. When gentle suction is then applied to the membrane via the patch pipette, the resistance of the measuring patch pipette eventually rises to the G Ω range. If the membrane remains intact during this sealing procedure, the “cell-attached” configuration has been achieved (Fig. 2.3), in which single ion channel fluctuations can be recorded with an inner intact compartment. The cell-attached configuration also serves as the starting point for the generation of the three other measuring configurations. If in the cell-attached mode the membrane patch in the tip of the patch pipette can be destroyed through a sudden short suction pulse, leading to the “whole-cell configuration”. This negative pressure can be simultaneously applied to the membrane patch in combination with very short rectangular voltage pulses as it was done in the present work (± 800 mV, 10 ms) (Fig. 2.3). The whole-cell configuration then enables macroscopic current recordings over the entire membrane surface under controlled solute conditions on both sides

of the membrane. If in the whole-cell mode the patch pipette is gently moved away from the patch membrane, the membrane attached to the glass pipette will rupture and immediately re-fuse and form a tight membrane patch in the tip of the patch pipette. This so-called “outside-out configuration” is suitable for measuring single ion channel currents, with the extracytosolic of the membrane facing the bath medium (Fig. 2.3). If in the cell-attached mode the patch pipette is directly pulled away from the patched cell membrane, a small vesicle forming in the patch pipette tip detaches from the remaining membrane. With short exposure of the pipette tip to air, the vesicle ruptures thus the cytoplasmic side of the membrane becomes open to the outside, the “inside-out configuration” is achieved (Fig. 2.3). In this configuration, the cytosolic side is facing the bath solution (just the reverse of the outside-out configuration). In this study, the patch-clamp technique was applied to plant mesophyll vacuoles in the whole-vacuole and outside-out mode. In both cases the cytosolic side of the tonoplast was then exposed towards the bath solution in the measuring patch-clamp chamber, while the luminal side of the vacuole membrane was facing the patch pipette solution.

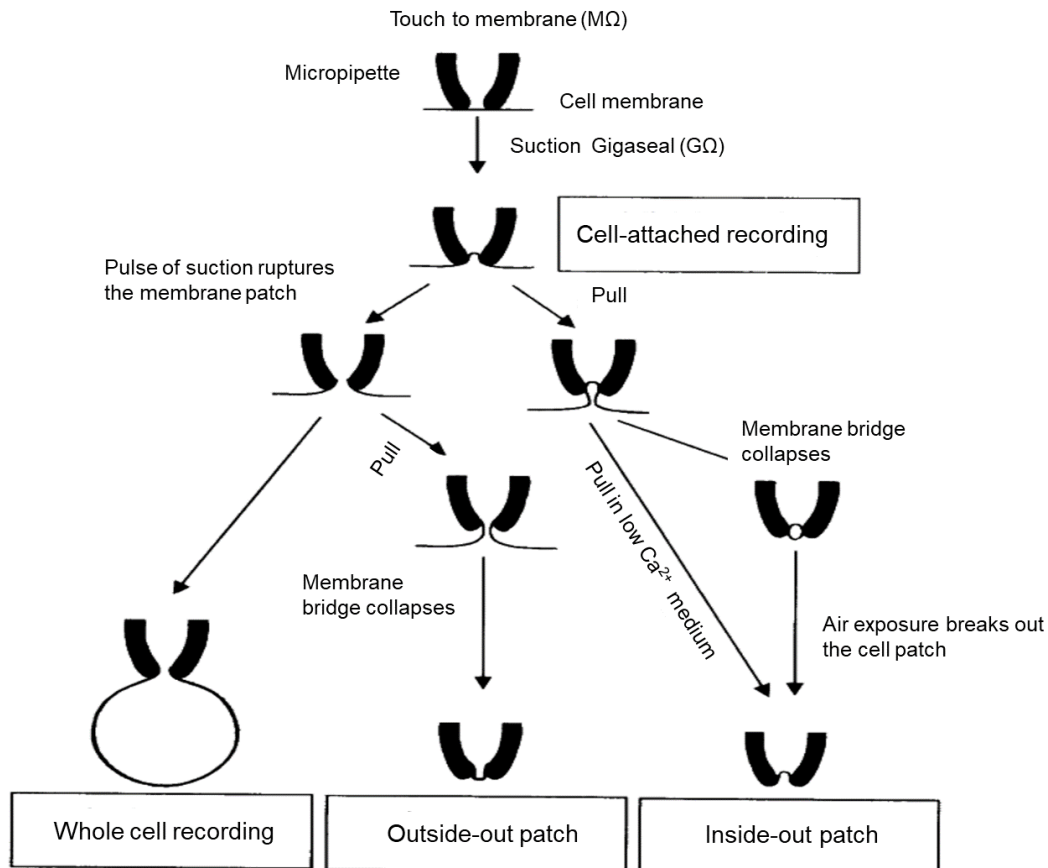


Fig. 2. 3. Four different patch-clamp configurations.

Details are described in the main text. Illustration was created in accordance with Hamill and Sakmann (1981).

2.3.3. Components of a patch-clamp setup

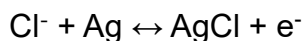
The patch-clamp setup used in this thesis was composed of the following elements. The patch-clamp measuring station was surrounded by a Faraday cage to protect it from external, system-independent electromagnetic inductions. A pneumatic-vibration-damped table was placed inside the cage, on which an inverted microscope (Axiovert 10, Carl Zeiss AG, Germany) was mounted. The measuring chamber was placed in the centre of the microscope stage (Inverted movable top plate, Scientifica, England). Additionally, a micromanipulator (Patch Star Micromanipulator, Scientifica, England) with a patch pipette holder was mounted on the microscope stage on the right side of the measuring chamber. The patch pipette holder was connected to an EPC800

or EPC10 amplifier (HEKA Elektronik Dr. Schulze GmbH, Lambrecht, Germany) to record the electrical signals. Two peristaltic pumps (Ismatec SA, Switzerland) were connected via polyvinylchlorid (PVC) tubes to the recording chamber enabling the constant perfusion – i.e. inflow and outflow - of the bath solution. The PVC tubes were disrupted by glass olives covered from the inside with Sigmacote® (Sigma, Munich, Germany), to avoid/minimize electrical connection between peristaltic pumps and measuring chamber. Accordingly, the measuring chamber was continuously perfused with the bath solution during the measurements which ensured a constant ion concentration in the chamber. To create a closed electrical circuit with grounding, a reference electrode connected to the amplifier was immersed in the bath medium in the patch-clamp chamber. For the conversion of the measured electrical signals from the patch electrode into digital signals, either the integral DA/AD converter of the EPC10 amplifier or, when using the EPC800 amplifier, the separate DA/AD converter ITC-16 (ITC-16, Instrutech Corp., Elmont, NY, USA) was used. Conversely, digital signals were converted into electrical signals via the DA/AD converter and applied to the electrodes. Digital signals were generated and recorded by the patch-clamp software Patchmaster or Pulse (HEKA Elektronik Dr. Schulze GmbH, Lambrecht, Germany) installed on the computer. For whole-vacuole mode, the sampling rate of 150 μ s at a low pass filter frequency of 2.9 or 3 kHz were applied for experiments using the EPC10 or EPC800 patch-clamp amplifier, respectively. For experiments in the outside-out mode, the sampling rate of 100 μ s at a low pass filter frequency of 1 kHz were carried out using an EPC10 patch-clamp amplifier. The computer as well as the power supplies of the microscope and the micromanipulators, the amplifier and the peristaltic pumps were placed outside the Faraday cage.

2.3.4. Preparation of pipettes and electrodes

Measuring and reference electrodes used for the patch-clamp experiments

were made of silver/silver chloride. To produce these electrodes, a silver wire (Ag^+) was immersed in a 3 M KCl solution and electrolytically chlorinated. The applied voltage covered the silver wire with a layer of silver chloride (AgCl):



The reference electrode was inserted into a bent polyethylene tube that was filled with 3 M KCl solution. The end of the tube placed in the bath medium was closed with an agarose plug consisting of 2% agarose in 3 M KCl. The agarose bridge prevented the 3 M KCl solution and cytotoxic silver ions from escaping the tube and contaminating the bath medium while at the same time the agarose plug ensured electrical conductivity of the reference electrode with the bath medium.

To create the measuring patch pipette, glass capillaries (Harvard Apparatus, UK) with a length of 10 cm and the outer/ internal diameter of 1.5/1.17 mm were used. The inner side of the glass capillaries was coated with SigmaCote® (Sigma, Munich, Germany), which was dried at 60 °C overnight. Since SigmaCote® prevents electrolytes from adhering to the glass wall of the pipette (Shoffner *et al.*, 1996), the interfering capacities of the measuring system were reduced via this treatment. The SigmaCote®-treated capillaries were pulled out in two steps with a vertical pipette puller (NARISHIGE, Tokyo, Japan). The first step thinned the capillary in the middle part, the second step finally separated the capillaries into two pipettes. The glass pipette close to the small tip was coated with Sylgard (World Precision Instruments, Sarasota, FL, USA). The Sylgard should cover those glass surfaces that were immersed in the bath solution in order to further minimize the capacity of the glass. During my experiments, the patch pipettes achieved a basic resistance in the range of 1.41 M Ω to 3.5 M Ω for whole-vacuole recordings and of 9.87 M Ω -18.34 M Ω for single channel experiments.

2.3.5. Sign convention

By convention, the voltage applied to a biological membrane reflects the electrical potential on the cytosolic side of the membrane relative to the extracellular side. The extracellular electrical potential is set to zero. The membrane potential of endomembrane has also been given for the cytosolic membrane side since 1992 (Bertl *et al.*, 1992). With regard to vacuoles, the vacuole lumen is therefore defined as an extracytosolic space. Therefore, the voltages in the vacuole side were opposite with the applied voltages for cytosolic side.

2.3.6. Voltage clamp experiments

After the whole-vacuole or outside-out configuration was established, the membrane currents were recorded in the so-called voltage clamp mode.

2.3.6.1. Whole-vacuole experiments

2.3.6.1.1. Activating voltage pulses

In the whole-vacuole mode, a TPC1-channel-activating voltage-pulse protocol (Fig. 2.4) was applied to clamp the tonoplast to certain membrane voltages, and the corresponding current responses were recorded. The membrane voltage was hold at -60 mV for 200 ms to keep the population of vacuolar TPC1 channels in a closed state. Then, the clamped voltage was instantaneously varied to voltages in the range of -80 mV to +110 mV in 10-mV increments. These voltage pulses lasted 1 s to observe the voltage-dependent activation of TPC1 currents. In the last segment the membrane was instantaneously clamped to -60 mV for 300 ms to induce deactivation of TPC1 channels and to record the relaxing tail currents.

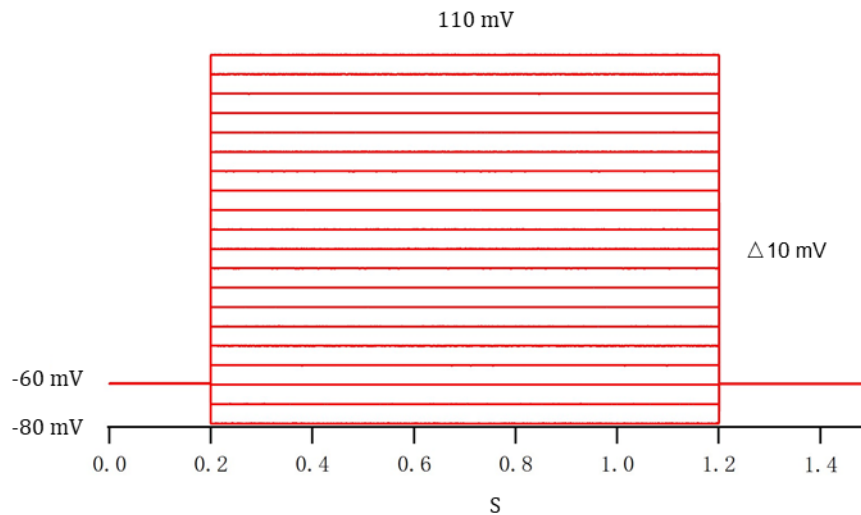


Fig. 2. 4. TPC1-activating voltage-pulse protocol for whole-vacuole current recordings.
See details in the main text.

2.3.6.1.2. Deactivating voltage pulses

After pre-activation of TPC1 currents upon an activating voltage pulse to either +80 mV or +100 mV lasting 300 ms, 200 ms-lasting voltage pulses in the range from +60 mV to -60 mV were applied in 5-mV decrements. Then, the relaxation of the TPC1 currents were recorded (Fig. 2.5).

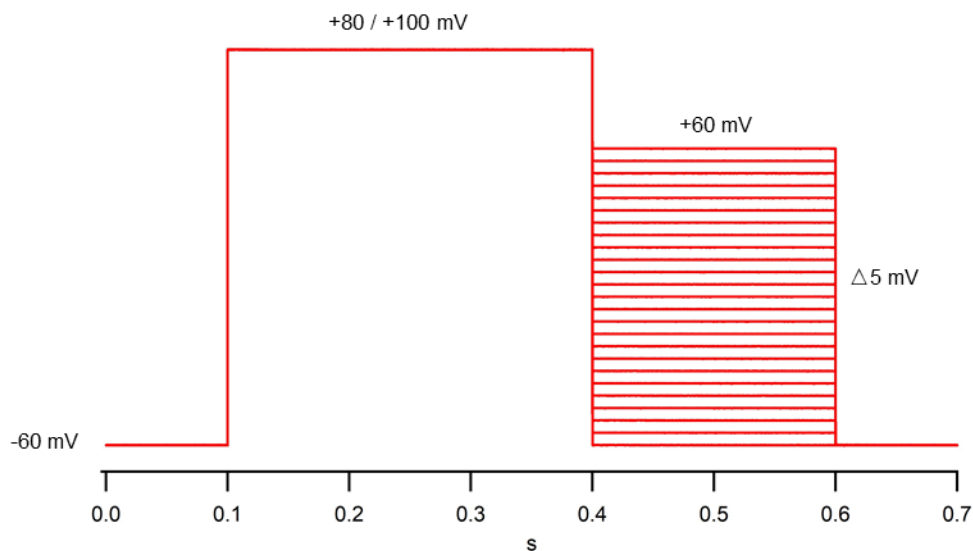


Fig. 2. 5. TPC1-deactivating voltage-pulse protocol for whole-vacuole current recordings.
See details in the main text.

2.3.6.1.3. Analysis of current recordings

The current source data were pre-analyzed with Patchmaster or Pulse. Then,

the further processing of the data analyses was carried out with the software program IGOR Pro 6 (Wave Metrics Inc., Lake Oswego, USA). In order to be able to compare the macroscopic currents measured from an individual vacuole with those of another one, the whole cell currents were normalized to the membrane capacity (C_m) which was compensated and recorded in experiments with an EPC800 or EPC10 amplifier. The C_m can be taken to assess the vacuole size, because the membrane operates as a plate capacitor and therefore the C_m is proportional to the membrane surface (Hille, 1992). During my PhD work, the whole-vacuole patch-clamp current data were analyzed according to four criteria: steady-state current density ($I_{ss}/C_m(V)$), relative channel open probability reflected by conductance voltage curve (G/G_{max}), half-activation and half-deactivation times ($t_{act-0.5}$, $t_{deact-0.5}$).

2.3.6.1.4. Determination of the steady-state current density

The TPC1 channel represents a voltage-dependent channel, that is activated with positive-going voltages, i.e. more TPC1 channels are open with increasing membrane depolarization. The current amplitude at a certain membrane voltage $I_{total}(V)$ depends on three factors as given by the following equation (1):

$$I_{total}(V) = N_{total} \cdot i(V-E_N) \cdot P_o(V) \quad (1)$$

with

- i) the total number of channels (N_{total}) present in the membrane.
- ii) single-channel current amplitude $i(V-E_N)$ depending on the voltage driving force $V-E_N$ which is defined by the difference between the applied membrane voltage V and the electrochemical equilibrium potential E_N , i.e. the Nernst potential for the transported ion specie.
- iii) the voltage-dependent channel open probability $P_o(V)$ at a certain voltage.

When the number of open channels becomes stable in response to a voltage pulse, according to equation (1), the corresponding total current amplitude $I_{total}(V)$ would remain unaltered. Such unchanged total current was defined as the

steady-state current (I_{ss}). To determine the steady-state TPC1 currents (I_{ss}), the current amplitudes recorded during the last 10 ms of each 1-s-lasting voltage pulse were selected and averaged (Fig. 2.6A). For each whole-vacuole experiment, the obtained I_{ss} values were normalized to the membrane capacity (C_m) of the individual vacuole given as $I_{ss}/C_m(V)$. Subsequently, $I_{ss}/C_m(V)$ were presented as a function of the membrane voltage in a current/voltage (I/V) graph (Fig. 2.6B).

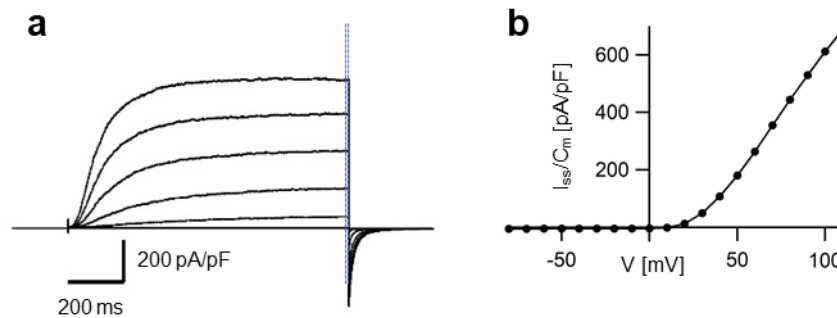


Fig. 2. 6. Representative analysis of the steady-state current density.

(a) Whole-vacuole current responses to different voltage pulses were normalized to the membrane capacity. The steady-state current densities were determined at the end of the voltage pulses for 10 ms, as marked by the blue dashed lines. (b) Current-voltage relations from the steady-state current densities which were determined from current traces shown in A and plotted against the respective clamped membrane voltage.

2.3.6.1.5. Analysis of the relative channel open probability

To calculate the voltage-dependent relative channel open probability (rel. $P_o(V)$), tail currents were analyzed (Fig, 2.6a). For this, after prepulse-voltages in the range of -80 to +110 mV were applied, tail currents were recorded at -60 mV. Since at -60 mV, the driving force ($V-E_N$) for the ion movement through open TPC1 channels was identical, the tail current amplitude only depended on the number of channels which were open in the steady-state in response to the prepulse-voltage. Thus, according to the equation (1) $I_{total}(V) = N_{total} \cdot i(V-E_N) \cdot P_o(V)$, the relative number of open channels at a certain voltage given by $N_{total} \cdot P_o(V)$ can be calculated. If one now assumes that the number of channels present in the membrane N_{total} is constant, the tail current amplitude (I_t) is a measure for the voltage-dependent relative channel open probability (rel. P_o

(V)). In my study, the tail currents recorded at the beginning 10 ms of whole tail currents excluding capacitance currents were selected and averaged as tail current amplitudes (I_t) (Fig 2.7). Then tail current amplitudes (I_t) were plotted against the corresponding prepulse-voltage (Fig. 2.7).

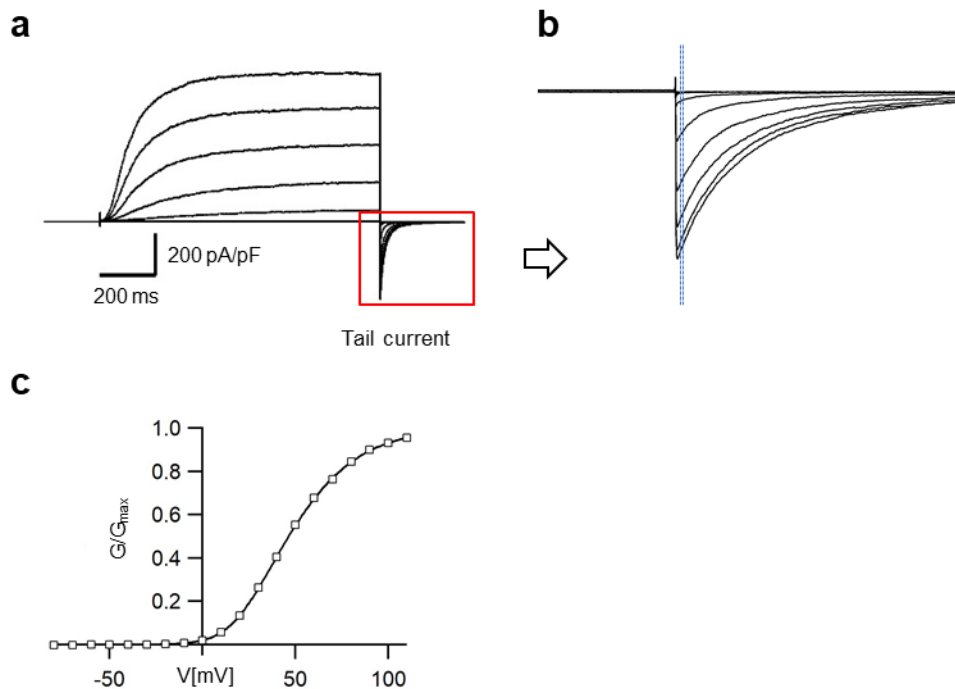


Fig. 2. 7. Representative analysis of relative channel open probability.

(a) Whole-vacuole currents recorded in response to different voltage pulses. After the prepulse voltage were applied in the range of from -80 mV to +110 mV in 10 mV steps, tail currents (marked by the red square) were induced by jumping to the deactivating holding voltage of -60 mV. (b) Magnified tail currents from A. The tail current amplitudes were determined at the point marked by the blue dashed lines. (c) Conductance-voltage curves ($G/G_{\max}(V)$) were determined via tail currents. After normalizing to the maximum tail current amplitude predicted by the Double Boltzmann equation, tail current densities given by black squares were plotted to the respective voltages. Solid line gives the best fit of the data points.

According to Pottosin *et al.* (2004) and Dadacz-Narloch *et al.* (2011), a three-step model for TPC1 channel gating consisting of two closed and one open state was assumed ($C_2 \rightleftharpoons C_1 \rightleftharpoons O$). Therefore, the slope of the tail current data points was fitted with a two-phase Boltzmann equation as followed:

$$I_t(V) = I_{\max} \cdot \frac{1}{1 + \exp\left(-z_1 \cdot \frac{V - V_1}{k_B \cdot T}\right) \cdot \left(1 + \exp\left(-z_2 \cdot \frac{V - V_2}{k_B \cdot T}\right)\right)}$$

with $k_B \cdot T \approx 25.26$ mV at room temperature. V_1 and V_2 give the midpoint activation voltages for the $C_1 \rightleftharpoons O$ and the $C_2 \rightleftharpoons C_1$ transitions, respectively. z_1 and z_2 represent the equivalent gating charges of these transitions.

The tail currents (I_t) and the fits were then normalized to the maximal predicted currents (I_{max}) of the best Boltzmann fit to obtain the normalized conductance-voltage curves ($G/G_{max}(V) = I_t/I_{max}(V)$) which can represent the relative channel open probability.

2.3.6.1.6. Analysis of the half-activation times

The half-activation time $t_{1/2}$ of TPC1 channel is the time at which the current amplitude reached 50% of the maximum current amplitude elicited upon a certain voltage pulse. To determine the half-activation time, first the instantaneous current (I_{inst}) amplitude was subtracted. Subsequently, the current response was normalized to maximal steady-state current amplitude and the time $t_{act-0.5}$ was calculated at which the half-maximum current amplitude $I_{0.5}$ was reached (Fig. 2.8).

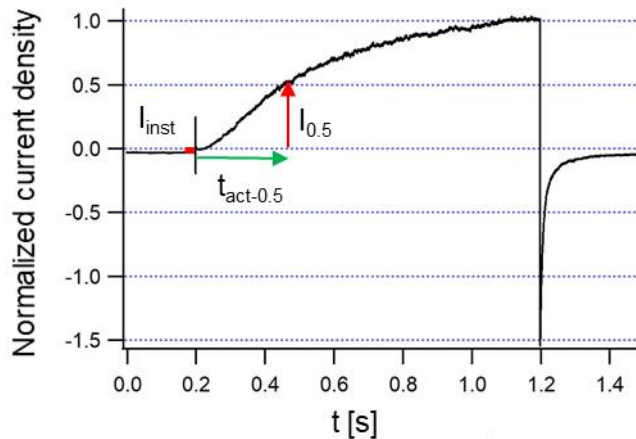


Fig. 2. 8. Principle of analysis of the half-activation time.

The determination of the half-activation time is illustrated here using a current response evoked upon a +110-mV stimulation. After subtraction of the instantaneous currents (I_{inst} , red line indicated) the current was normalized to the maximal steady-state current amplitude. Red arrow line indicates half-maximal current amplitude ($I_{0.5}$) and the green arrow line the half-activation time $t_{act-0.5}$.

2.3.6.1.7. Analyses of the Half-deactivation times

The half-deactivation time $t_{\text{deact-0.5}}$ of TPC1 channel is the time when the current amplitude reached 50% of the maximum deactivating current amplitude at a certain voltage. To determine the half-deactivation time, first the leak current (I_{leak}) amplitude was subtracted. Subsequently, because of the superimposed effect of residual capacitance peaks, the initial deactivating current amplitude was mixed with capacitance current. Since in the present study the capacitive currents lasted 0.0008-0.0011 s for all measurements, the actual maximum deactivating current was determined after the longest sustained capacitance current (0.0011 s). Then, the deactivating current response was normalized to actual maximum deactivating current amplitude, and the $t_{\text{deact-0.5}}$ was calculated at which the half-maximum deactivating current amplitude $I_{\text{deact-0.5}}$ was reached (Fig. 2.9).

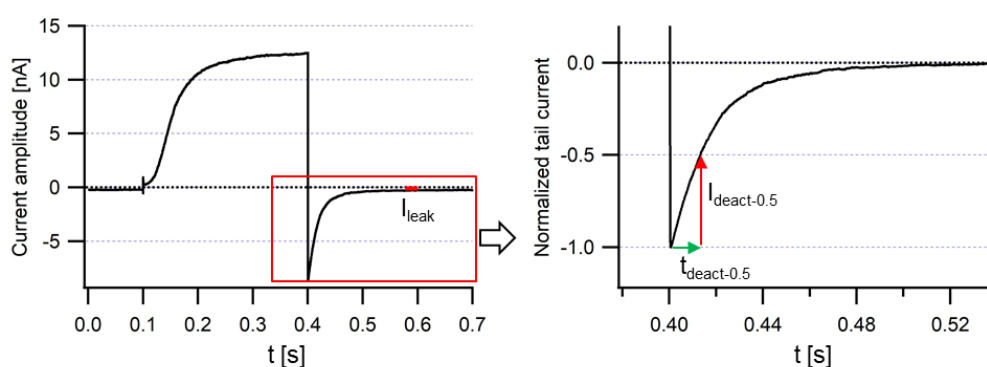


Fig. 2. 9. Representative analysis of the half-deactivation time.

The half-deactivation time was determined by applying deactivating voltage pulses (section 2.3.6.1.2). Here is an illustration that current relaxation was induced upon jump from the voltage +100 mV to -60 mV. After subtraction of the leak currents (I_{leak} , red line indicated), the current was normalized to the real maximal current amplitude. Red arrow line indicated half-maximal current amplitude ($I_{\text{deact-0.5}}$) and the green arrow line showed the half-activation time $t_{\text{deact-0.5}}$.

2.3.6.2. Single channel experiments

2.3.6.2.1. Pulse protocol

Single channel recordings were performed in the outside-out configuration (section 2.3.2) in which the luminal side of the vacuolar membrane was facing the pipette solution. For current recordings, the following voltage-pulse protocol

was applied to the membrane patch (Fig. 2.10). First, the membrane was clamped to -60 mV for 300 ms to deactivate the channels. Then, a 30-s-lasting activation pulse to either +10 mV, +15 mV, +20 mV, +25 mV or 30 mV was applied.

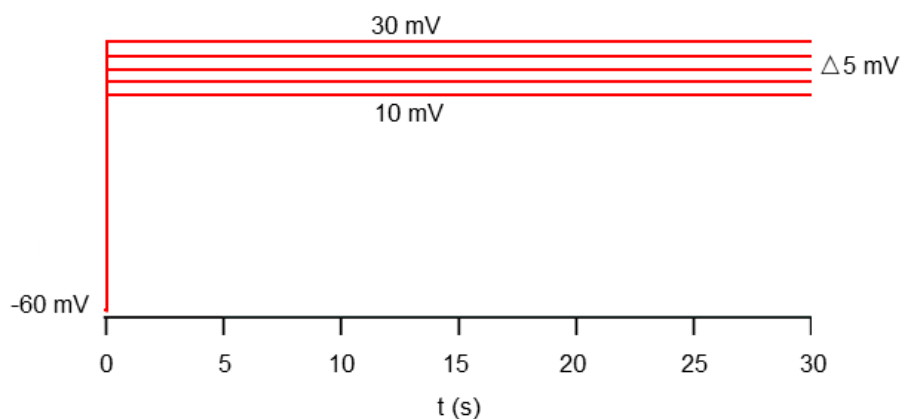


Fig. 2. 10. Activating voltage-pulse protocol applied for single channel recordings.
See details in the main text.

2.3.6.2.2. Analysis of the single channel conductance

To determine the single-channel conductance, single channel currents were recorded at different membrane voltages and the respective single channel amplitude i was determined via an all-point current amplitude histogram (Fig. 2.11). In the histogram, the derived first peak represented the current baseline, at which the channels are in the closed state C . The second peak in the current amplitude histogram gives the current level at which one TPC1 channel was open (O_1), and the third peak represents two simultaneous TPC1 channel openings (O_2). The peak maxima were determined by fitting the histogram with a Gaussian equation, and the single channel amplitude i was calculated between the peak maxima (Fig. 2.11a, b). The deduced single channel amplitudes i were plotted to the respective voltage. The total data set derived from experiments on several individual vacuoles was subjected to global fitting with a linear function ($y = ax + b$). Here, the slope "a" obtained represents the channel conductance (Fig. 2.11c).

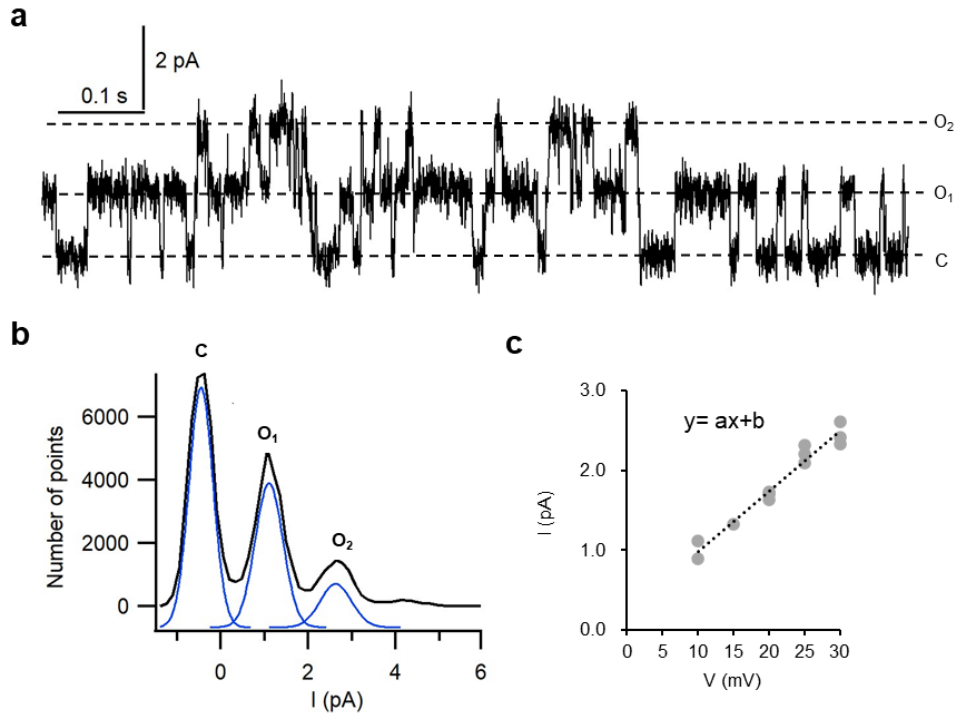


Fig. 2. 11. Analysis of single channel conductance.

(a) Single channel current trace evoked upon +25 mV voltage stimulation were analyzed for different current levels such as C, O₁, O₂ indicating closed channels, 1 or 2 simultaneously open channels, respectively. (b) The current amplitude histogram (black) derived for the single channel current trace shown in (a) were fitted with a Gaussian equation (blue). Maxima represent current levels where the channels were closed (C) or 1 or 2 channels (O₁, O₂) open. (c) i/V graph for single channel currents determined from several vacuoles at corresponding voltages. Black dotted line gives the global fit of the total data points.

2.3.7. Current clamp experiments

After establishing the whole-vacuole configuration, the current clamp mode was chosen to monitor the membrane voltage.

2.3.7.1. Current pulses

In current clamp measurements, the membrane depolarization of the vacuole membrane was mimicked by current injections. Consequently, with increasing current injection, the depolarization was stronger and more TPC1 channels were activated. Before current injection, the vacuole membrane was first set to -60 mV to keep the TPC1 channel in the closed state by clamping the current

to an appropriate level. In the following, instantaneous current injection pulses ranging from 10 up to 1000 pA were applied for 200 ms before returning to the initial current clamp state (-60 mV) (Fig. 2.12). The vacuole membrane voltages were recorded for 10 s after each current injection pulse.

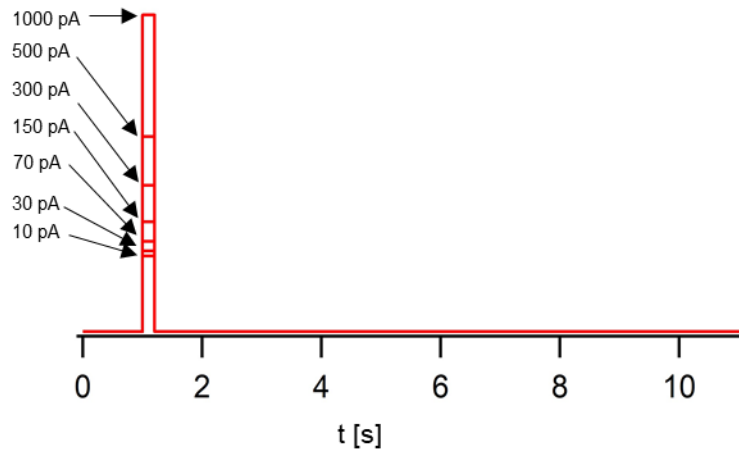


Fig. 2. 12. Current pulse protocol applied for voltage recordings.
See details in the main text.

2.3.7.2. Analysis of the voltage recordings

The amplitude of the voltage responses to the current injection pulse at its beginning and at the end, i.e. the initial stimulus voltage spike and the stimulus voltage plateau, respectively, was determined. Furthermore, the lifetime of the post-stimulus depolarization phase (t_{plateau}), which indicates the time in which 50% of the initial depolarized voltage level repolarized to the holding voltage, was calculated (Fig. 2.13).

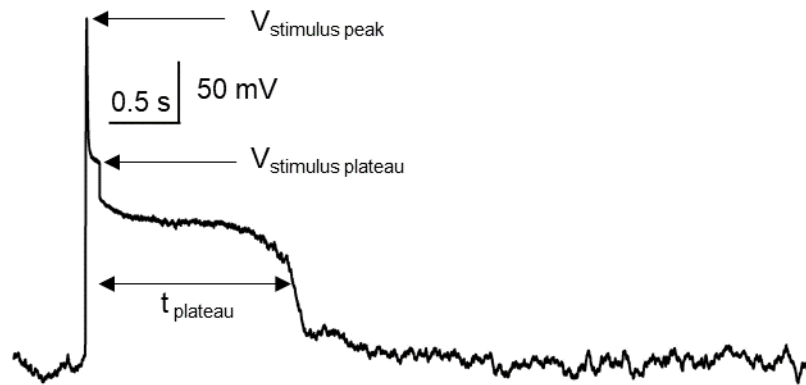


Fig. 2. 13. Analysis of voltage recordings before, during and after current injection.

The analysis of voltage recordings is illustrated here using the voltage response to a 500 pA current pulse. The stimulus peak voltage amplitude ($V_{\text{stimulus peak}}$) was determined at the beginning of the injected current pulse and the stimulus plateau voltage ($V_{\text{stimulus plateau}}$) at the end of the injection current pulse. The post-stimulus plateau phase (t_{plateau}) denotes the time at which 50% of the depolarized voltage repolarized to the holding voltage (-60 mV).

2.3.8. Patch-clamp solutions

The solutions used for the whole-vacuole and single channel measurements with transiently transformed vacuoles were listed in Table 2.14-16.

Table 2. 14. Solutions for whole-vacuole voltage clamp measurements.

Bath solution	Pipette solution	Pipette solution	Pipette solution
	0 mM Ca^{2+}	10 mM Ca^{2+}	50 mM Ca^{2+}
150 mM KCl	150 mM KCl	150 mM KCl	150 mM KCl
1 mM CaCl_2	0 mM CaCl_2	10 mM CaCl_2	50 mM CaCl_2
-	2 mM MgCl_2	2 mM MgCl_2	2 mM MgCl_2
-	0.1 mM EGTA	-	-
10 mM HEPES	10 mM HEPES	10 mM HEPES	10 mM HEPES
pH 7.5 adjusted	pH 7.5 adjusted	pH 7.5 adjusted	pH 7.5 adjusted
with Tris	with Tris	with Tris	with Tris
$\pi = 500$ adjusted	$\pi = 500$ adjusted	$\pi = 500$ adjusted	$\pi = 500$ adjusted
with D-sorbitol	with D-sorbitol	with D-sorbitol	with D-sorbitol

Table 2. 15. Solutions for whole-vacuole current clamp measurements.

Bath solution	Pipette solution
150 mM KCl	150 mM KCl
1 mM CaCl ₂	0.2 mM free CaCl ₂
2mM MgCl ₂	2 mM MgCl ₂
10 mM HEPES	10 mM HEPES
pH 7.5 adjusted with Tris	pH 7.5 adjusted with Tris
π = 500 adjusted with D-sorbitol	π = 500 adjusted with D-sorbitol

0.2 mM free Ca²⁺ was adjusted by addition of 4.1 mM EGTA and 4.3 mM Ca²⁺ according to the MAXCHELATOR

(<https://somapp.ucdmc.ucdavis.edu/pharmacology/bers/maxchelator/webmaxc/webmaxcE.htm>)

Table 2. 16. Solutions for single channel measurements.

Bath solution	Pipette solution
100 mM KCl	100 mM KCl
0.5 mM CaCl ₂	0.5 mM CaCl ₂
-	2 mM MgCl ₂
10 mM HEPES	10 mM MES
pH 7.5 adjusted with Tris	pH 5.5 adjusted with Tris
π = 400 adjusted with D-sorbitol	π = 400 adjusted with D-sorbitol

2.3.9. Liquid junction potential

When two different ionic solutions with different ionic mobility contact each other, a potential difference could develop at the junction of the two solutions. This potential is called liquid junction potential (LJP). At the beginning of the experiments when the pipette solution was directly in contact with the bath solution, the offset potential (V_{offset}) of the patch-clamp amplifier was adjusted and set to 0 mV. Therefore, LJP between these two solutions – if present – was

counteracted by the offset potential (V_{Offset}). However, after the Gohmic seal was established, LJP vanished because of the missing contact between the pipette solution and bath solution. Thus, the original V_{Offset} (0 mV) is incorrect. In the other words, the clamped voltage (V_{clamp}) applied during an experiment did not represent the effective clamped membrane voltage (V_m). Therefore, the V_{clamp} needed be corrected by the LJP. LJP was experimentally determined according to Neher, 1992 and Ward and Schroeder, 1994 and used for offline correction of the clamped voltage using the following equation (2):

$$V_m = V_{\text{clamp}} - \text{LJP} \quad (2)$$

During this work, LJP was less than 1 mV in the current clamp and voltage clamp measurements recorded with 0 mM Ca^{2+} and 10 mM Ca^{2+} in the pipette solutions. Therefore, LJP was ignored in those measurements, i.e. the clamped voltage was not corrected for LJP. For whole-vacuole current measurements performed with 50 mM Ca^{2+} in the pipette solution, the LJP was -3.8 mV. Accordingly, the clamped membrane voltage was corrected by -3.8 mV using equation (2) to calculate the effective membrane voltage (V_m).

2.3.10. Statistical analysis

All electrophysiological data are given as means \pm SEM. Significant differences $V_{1/2}$ values under 0 mM luminal Ca^{2+} conditions were analyzed with one-way-ANOVA followed by the Dunnett's post hoc comparison test. To enable the statistical analysis (one-way-ANOVA with Dunnett's post hoc comparison test) of the Ca^{2+} -induced shift in the $V_{1/2}$ values, the means of the V_1 and V_2 values determined in the absence of luminal Ca^{2+} were subtracted from the individual V_1 and V_2 values, respectively, derived under 10 mM luminal Ca^{2+} conditions. Significant difference with z_1 and z_2 values were analyzed with one-way ANOVA followed by Dunnett's post hoc comparison test. Significance of Ca^{2+} -induced changes in $z_{1/2}$ values were tested with Student's t- test. One-way-ANOVA with

turkey's post hoc comparison test was used to test the significant difference of t_{plateau} . Statistical analysis was done with SPSS 2020 (IBM, New York, USA).

3. Results

3.1. The effect of pore mouth of AtTPC1 on voltage and luminal Ca²⁺ sensing

In order to elucidate the molecular mechanism of luminal Ca²⁺ binding in the plant TPC1/SV channel, I examined in the first part of my work whether pore mouth residues could additionally function as a luminal calcium-binding site. To this end, I generated several single and triple AtTPC1 mutants with respect to the luminal pore mouth by replacing Glu605, Asp606, and the adjacent negatively charged amino acid Asp607 individually or together with the corresponding neutral amino acid glutamine (Q) or asparagine (N). In addition, Glu605 was mutated to alanine (A) to investigate whether the size of amino acid, i.e. the length and bulkiness of the side chain residues, influences the binding of luminal Ca²⁺. The derived AtTPC1 mutants were designated E605A/Q, D606N, D607N and E605Q/D606N/D607N (EDD). In the following, the effect of these AtTPC1 mutations on targeting and channel function was studied.

3.1.1. Membrane targeting of the AtTPC1 pore mouth mutants

In order to verify the subcellular localization of the different AtTPC1 channel variants in the vacuole membrane and to be able to identify successfully transformed vacuoles for subsequent electrophysiological experiments, AtTPC1-WT as well as all AtTPC1 pore mutants (E605A/Q, D606N, D607N and E605Q/D606N/D607N) were C-terminally fused with eGFP (section 2.1.1). After transient transformation the subcellular localization of the eGFP-labelled Arabidopsis channel variants in fluorescent *attpc1-2* protoplasts was examined with a confocal laser scanning microscope (section 2.2.6). As illustrated in

Figure 3.1, eGFP fluorescent signals were observed locally as a circle at the periphery of the protoplasts, indicating that AtTPC1 channel variants were localized either in the plasma membrane or vacuole membrane. However, for some AtTPC1-transformed protoplasts, the red autofluorescent chloroplasts were outside this green fluorescent circle, suggesting that AtTPC1 channel variants were located in the vacuole membrane. To provide further evidence for the vacuolar targeting, the vacuoles were released from the transformed protoplasts by hypoosmotic shock (section 2.2.5).

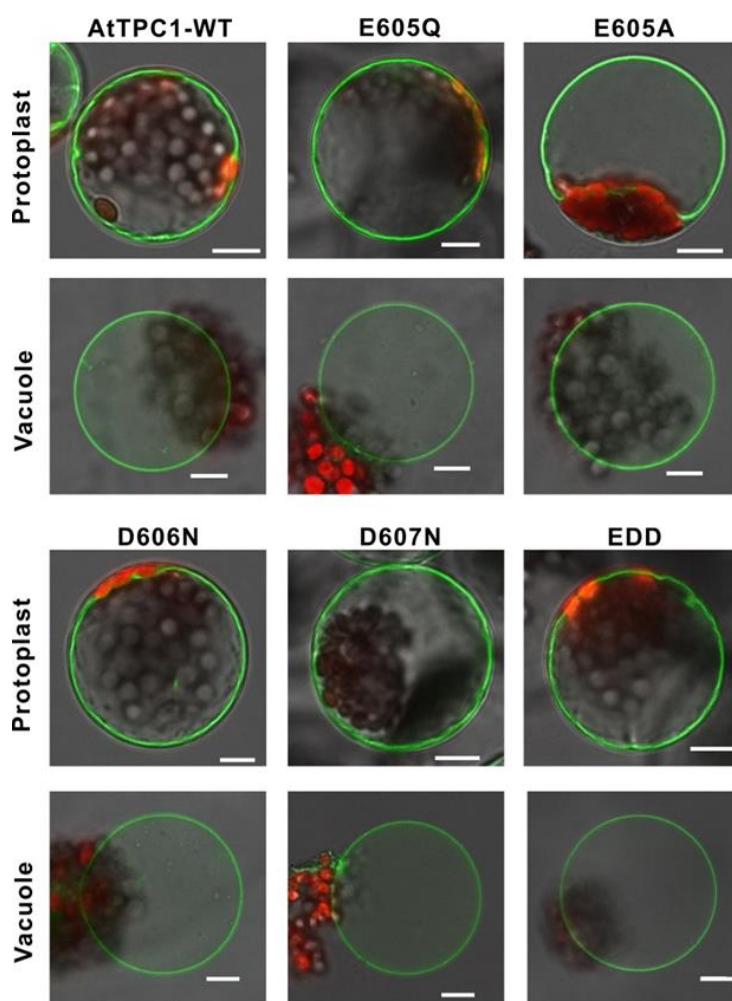


Fig. 3. 1. Subcellular localization of *Arabidopsis thaliana* TPC1 channel variants. Confocal images of mesophyll protoplasts and released vacuoles of the *Arabidopsis thaliana* loss-of-function mutant *attpc1-2* transiently transformed with different AtTPC1 channel variants which were fused to the green fluorescent protein (eGFP). For all channel variants the green fluorescence signal was restricted to the vacuole membrane. Fluorescent images and bright field images were merged. Scale bar = 10 μ m. WT represents wild type and EDD the triple mutant E605Q/D606N/D607N.

Red autofluorescent chloroplasts adhered to the outside of the vacuole membrane, while green fluorescence of eGFP was observed at the periphery of the vacuole (Fig. 3.1). These observations indicate that the transiently expressed AtTPC1 pore mutant channels - like AtTPC1-WT channel - were all targeted to the vacuole membrane. Thus, the C-terminal eGFP fusion to the AtTPC1 channel proteins did not affect the localization of the TPC1 channel in the tonoplast. Therefore, these vacuoles were suitable for performing patch-clamp studies of the TPC1 channel properties.

3.1.2. Function of AtTPC1 pore-mouth channel variants

In order to investigate the function of AtTPC1 pore mutant channels transiently expressed in *attpc1-2* mesophyll vacuoles, macroscopic TPC1 currents were measured in the whole-vacuole patch-clamp configuration. Patch-clamp experiments were conducted in the presence of 150 mM K⁺ at both sides of the vacuole membrane. Additionally, 1 mM Ca²⁺ were present at the cytosolic side of the vacuole membrane to enable voltage-dependent TPC1 channel activation. When the vacuolar Ca²⁺ concentration was adjusted with EGTA to 0 mM and the voltage pulses in the range of - 80 mV to +110 mV were applied, slowly activating outward currents were measured with AtTPC1-WT as well as the different AtTPC1 channel mutants (Fig. 3.2a). Thus, these current recordings indicated that all AtTPC1 channel mutants are functional in the *attpc1-2* vacuole.

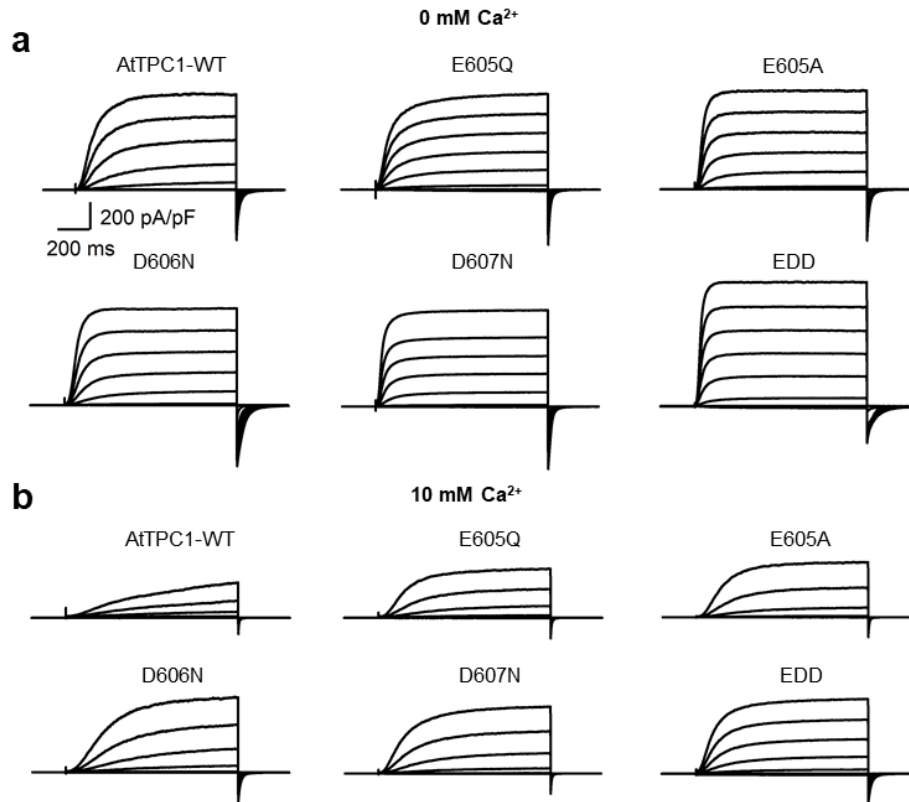


Fig. 3. 2. Macroscopic current responses of vacuoles transformed with AtTPC1 channel variants to voltage depolarization.

Macroscopic current responses of individual vacuoles to 1-s-lasting voltage pulses applied in the range of -80 to +110 mV in 20 mV increments in the absence (**a**) and presence (10 mM, **b**) of luminal Ca^{2+} . Currents were normalized to the membrane capacitance (C_m) of the respective vacuole. The holding voltage was -60 mV. The number of experiments performed on individual vacuoles per channel variant was $n=5$ for WT (wild type), E605Q, E605A, D606N and $n=4$ for D607N and EDD under luminal Ca^{2+} -free conditions. For 10 mM luminal Ca^{2+} , the number of experiments was $n=5$ for WT, E605Q and $n=4$ for E605A, D606N, D607N and EDD. EDD represents the triple AtTPC1 mutant E605Q/D606N/D607N.

After increasing luminal Ca^{2+} from 0 mM to 10 mM, the slowly activating outward currents for all TPC1 channel variants were reduced (Fig. 3.2b). When the steady-state current responses were normalized to C_m as a measure for the vacuole size and plotted against respective voltages, the well-known depolarization-dependent activation behavior of TPC1 channels became even more visible due to the non-linear current-voltage curves ($I_{ss}/C_m(V)$) (Fig. 3.3a).

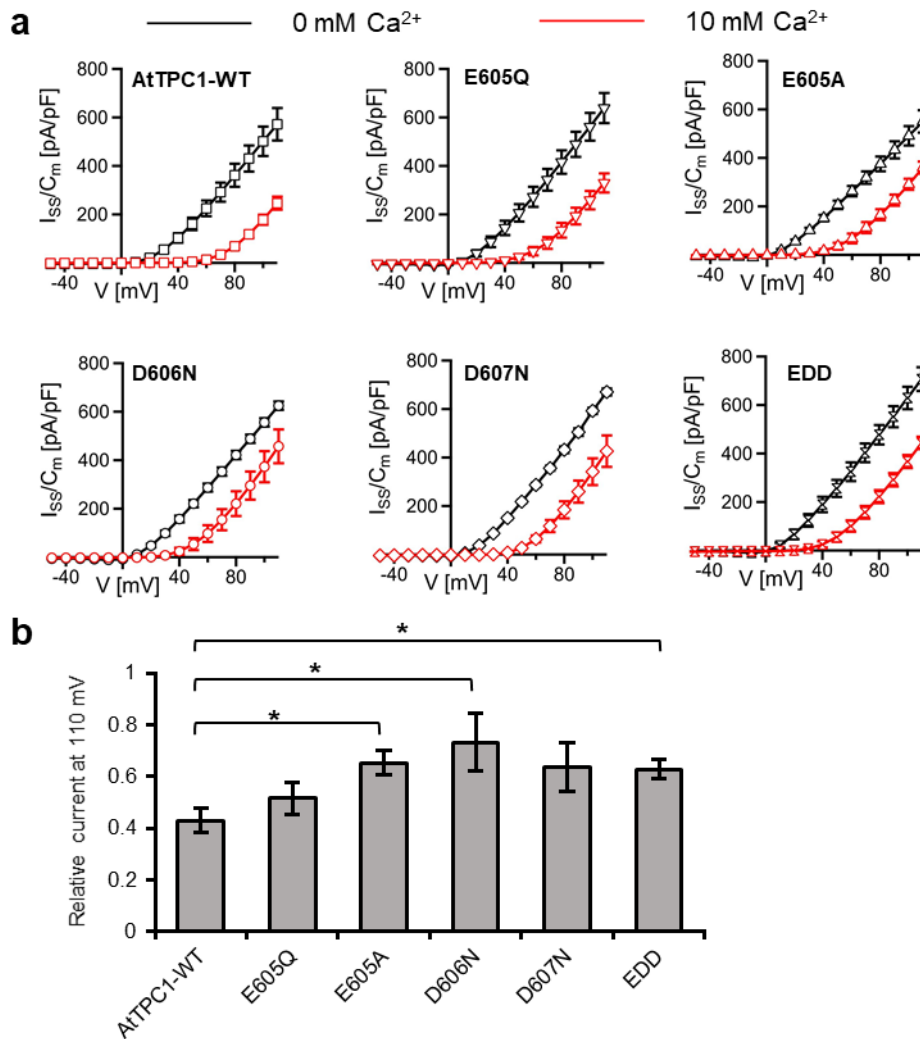


Fig. 3. 3. Effect of voltage and luminal Ca²⁺ on TPC1 currents mediated by different *Arabidopsis thaliana* channel variants.

(a) Normalized steady-state currents ($I_{ss}/C_m(V)$) plotted against the clamped membrane voltages (V) in the presence (red symbols and lines, 10 mM) and absence (black symbols and lines) of luminal Ca²⁺. Symbols represent means \pm SEM. **(b)** Bar diagram shows the current densities for AtTPC1 channel variants which were measured at +110 mV under 10 mM vacuolar Ca²⁺ and normalized to the current density determined at 0 mM vacuolar Ca²⁺. Significant differences in the current density between the AtTPC1-WT and the channel mutants were tested with Student's *t*-test. Significant differences between tested groups are indicated by asterisks (* $p < 0.05$). Number of experiments for each channel variant for both Ca²⁺ conditions was the same as in Figure 3.2. EDD represents the triple mutant E605Q/D606N/D607N.

Moreover, when the luminal Ca²⁺ level was increased from 0 mM to 10 mM, the current density of the AtTPC1 pore mutants reflected by the $I_{ss}/C_m(V)$ curve seem to diminish less than that of AtTPC1-WT (Fig. 3.3a). To quantify the luminal Ca²⁺-induced current decrease in the different AtTPC1 channel variants,

the current densities measured at +110 mV under 10 mM Ca^{2+} were normalized to that at 0 mM Ca^{2+} of all channel variants (Fig. 3.3b). As a result, the wild type TPC1 currents were suppressed by about 60% at +110 mV in the presence of 10 mM luminal Ca^{2+} . The Ca^{2+} -induced decrease in the current density of the single mutant E605Q and D607N was about 50% and 40%, respectively, and thus slightly lower than that of the wild type. In comparison, the Ca^{2+} -induced current suppression of the single TPC1 pore mutants E605A and D606N were only 35%, 25%, respectively, which was significantly smaller compared with AtTPC1-WT (Fig. 3.3b). Moreover, the current responses of the EDD(E605Q/D606N/D607N)-transformed vacuoles were reduced by 40% in the presence of high luminal Ca^{2+} which was also significantly lower than AtTPC1-WT but similar to the single mutants E605A and D606N. Taken together, the results suggest that these five AtTPC1 pore mutants are all functional channels but at least some of them probably exhibit a different sensitivity to inhibitory high luminal Ca^{2+} .

3.1.3. Effect of pore mouth mutations on voltage dependency of AtTPC1 channel and luminal Ca^{2+} sensitivity

In order to further investigate the luminal Ca^{2+} tolerance of these AtTPC1 pore mutants, the voltage-dependent relative channel open probability represented by conductance-voltage curves (G/G_{max} (V)) was determined in tail current experiments. Tail currents were elicited by an instantaneous jump from different pre-pulse voltages in the range of -80 mV to +110 mV to the negative voltage of -60 mV, resulting in the deactivation of the TPC1 channels. Due to the unified driving force for the ion movement at -60 mV, the instantaneous tail current amplitude only depended on the number of open channels activated upon the previous voltage pulse and therefore was used to determine the conductance-

voltage curve ($G/G_{\max}(V)$) (section 2.3.6.1.6, Fig. 3.4).

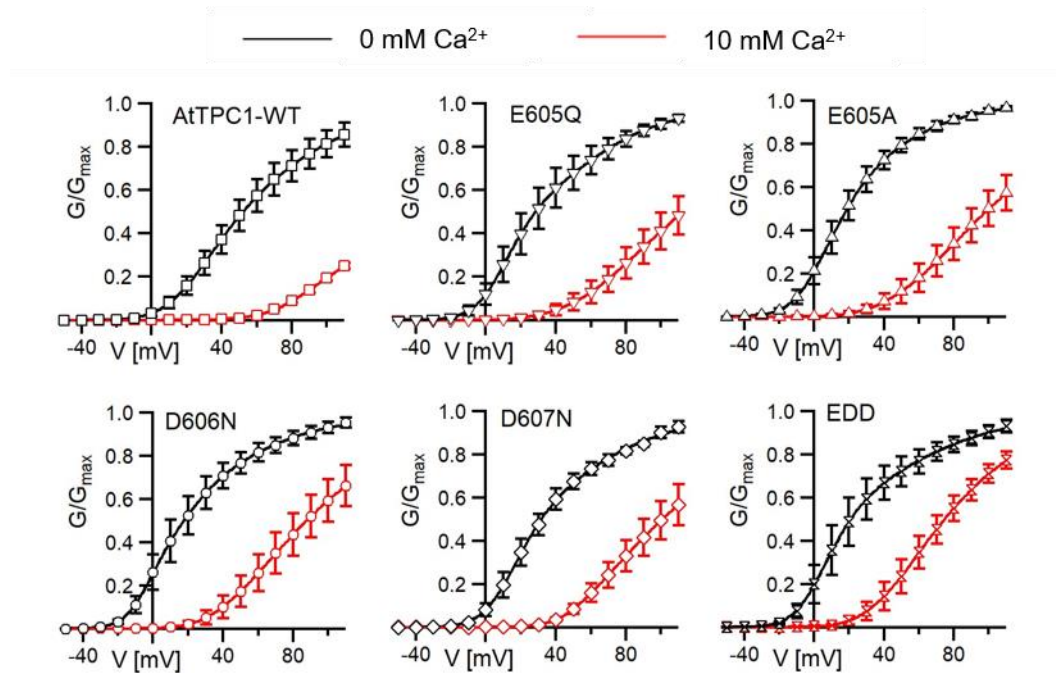


Fig. 3. 4. The voltage dependence of *Arabidopsis thaliana* TPC1 channel variant.

Normalized conductance-voltage curves ($G/G_{\max}(V)$) of WT and pore mouth mutants in the presence (red symbols and solid lines, 10 mM Ca^{2+}) and absence (black symbols and solid lines) of luminal Ca^{2+} . Symbols represent means \pm SEM, and solid lines provide the best fits of the $G(V)$ curve to a double Boltzmann function. Number of experiments for each channel variant for both Ca^{2+} conditions is the same as in Fig.3.2. EDD represents the triple mutant E605Q/D606N/D607N.

In the absence of luminal Ca^{2+} , the voltage activation threshold of the AtTPC1 mutants E605A, D606N and EDD, as reflected by the incipient increase of the $G/G_{\max}(V)$ curve, was approximately -30 mV, whereas that of E605Q and D607N was approximately -20 mV. In contrast, the channel opening of AtTPC1-WT appeared to start from a positive membrane potential (Fig. 3.4a). This indicated that the voltage activation threshold for channel opening of the AtTPC1 pore mutants have shifted to more negative voltages compared to AtTPC1-WT (Fig. 3.4a). To further quantify this shift in the voltage-dependent relative channel open probability, the slope of the $G/G_{\max}(V)$ data points derived for the different channel variants were described with a double Boltzmann equation according to Pottosin *et al.* (2004). Thereby, a three-state model for channel gating consisting of two closed state and one open channel state (C_2

$\rightleftharpoons C_1 \rightleftharpoons O$) was assumed and midpoint activation voltages V_2 ($C_2 \rightleftharpoons C_1$) and V_1 ($C_1 \rightleftharpoons O$) were determined (Fig. 3.4b, c). When the $G/G_{\max}(V)$ curves determined from AtTPC1-WT-transformed vacuoles were fitted with the double Boltzmann equation, the midpoint activation voltage V_1 for the $C_1 \rightleftharpoons O$ transition of 51.2 ± 9.6 mV was calculated which was comparable to that recorded from *tpc1-2* vacuoles transiently transformed with Arabidopsis wild type TPC1 (60 ± 4.6 mV; Jašlan *et al.*, 2016). In comparison, the V_1 values determined for the single mutants E605Q and D607N were 18.9 ± 11.7 mV and 23.2 ± 4.9 mV, respectively, and thus tended to be smaller than that of AtTPC1-WT (Fig. 3.5a). Interestingly, the midpoint activation voltage V_1 of the single mutants E605A (7.4 ± 5.0 mV) and D606N (6.8 ± 9.4 mV) was similar to that of the triple mutant EDD (7.3 ± 13.7 mV) but significantly lower than that of AtTPC1-WT (Fig. 3.5a). In addition, midpoint activation voltage V_2 , reflecting the $C_2 \rightleftharpoons C_1$ transition, was also altered in all different AtTPC1 variants compared with AtTPC1-WT (Fig. 3.5b). The V_2 values of the single mutants E605Q (14.4 ± 2.4 mV) and D607N (17.6 ± 3.1 mV) also tended to be lower than that of AtTPC1-WT (24.0 ± 3.8 mV). The V_2 values of single mutants E605A (8.8 ± 4.4 mV) and D606N (5.6 ± 4.5 mV) were significantly smaller than that of AtTPC1-WT (24.0 ± 3.8 mV). Similarly, the V_2 value of AtTPC1 pore triple mutant EDD (E605Q/D606N/D607N; $V_2 = 11.3 \pm 2.5$ mV), although not significantly different from AtTPC1-WT, also tended to be smaller than AtTPC1-WT as the single mutants E605Q and D607N (Fig. 3.5b). These results indicated that the removal of negative charged amino acids near the pore mouth facilitated channel opening of Arabidopsis TPC1 at more negative voltages in the absence of luminal Ca^{2+} . The single mutations E605A or D606N are sufficient to promote the channel activation, an effect which is not further enhanced by the additional two mutations in the triple mutant EDD(E605Q/D606N/D607N). Besides, both E605Q and E605A shifted the TPC1 channel activation to more negative voltage; among them E605A had a higher – significant – impact on changing the TPC1 channel activation than E605Q (Fig. 3.4b). This result suggests that it is not only the charge but also

the size of E605 amino acid side chain near the pore mouth of AtTPC1 that influences the voltage-dependent TPC1 channel opening.

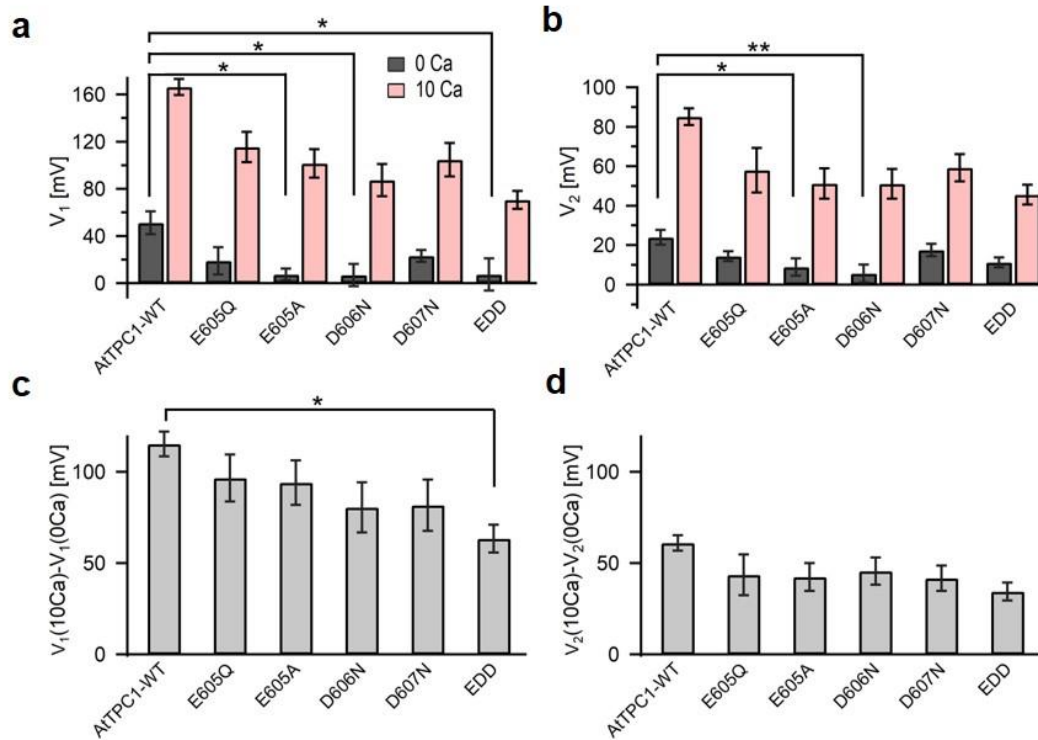


Fig. 3. 5. The voltage dependence of *Arabidopsis thaliana* TPC1 channel variant. (a, b) Midpoint activation voltages V_1 and V_2 were calculated in the presence of 0 mM (grey) and 10 mM Ca^{2+} (pink) in the vacuole lumen. Significant differences were only analyzed for $V_{1/2}$ values under luminal Ca^{2+} -free conditions with one-way ANOVA followed by Dunnett's post hoc comparison test. (c, d) Changes in $V_{1/2}$ values upon a rise in luminal Ca^{2+} from 0 to 10 mM. Significant differences tested with one-way ANOVA followed by Dunnett's post hoc comparison test. Significant differences between tested groups in (a-d) are indicated by asterisks (* $p < 0.05$, ** $p < 0.01$). Number of experiments for each channel variant for both Ca^{2+} conditions is the same as in Fig.3.2. EDD represents the triple mutant E605Q/D606N/D607N. All data points are mean values \pm SEM.

When the luminal Ca^{2+} concentration was increased from 0 to 10 mM Ca^{2+} , the midpoint activation voltages V_1 and V_2 values for the AtTPC1-WT and AtTPC1 pore mutants shifted to more positive potentials (Fig. 3.5c, d). To enable statistical analysis of the Ca^{2+} -induced shift in the $V_{1/2}$ values, the means of the V_1 and V_2 values determined in the absence of luminal Ca^{2+} were subtracted from the individual V_1 and V_2 values, respectively, derived under 10 mM luminal Ca^{2+} conditions (Fig. 3.5c, d). The midpoint activation voltage V_1 derived for

AtTPC1-WT increased by 115.2 ± 6.7 mV at 10 mM Ca^{2+} condition while the Ca^{2+} -induced rise in V_1 values of the AtTPC1 pore mutants tend to be less pronounced (Fig. 3.5c). Under high luminal Ca^{2+} the V_1 values of the single mutants E605Q/A, D606N and D607N were elevated by 96.6 ± 13.0 mV, 94.1 ± 12.2 mV, 80.5 ± 13.7 mV and 81.7 ± 14.1 mV, respectively, compared with 0 mM Ca^{2+} (Fig. 3.5c). However, statistical analysis indicated that only the combined triple mutation EDD (E605Q/D606N/D607N) significantly lowered the luminal Ca^{2+} -induced shift in V_1 value; i.e. the related ΔV_1 value of 63.4 ± 7.7 mV was significantly smaller in EDD compared to AtTPC1-WT (Fig. 3.5c). Likewise to the V_1 results, the Ca^{2+} -induced rise of the midpoint activation voltage V_2 also tends to be smaller for all AtTPC1 pore mutants compared to AtTPC1-WT. The lowest Ca^{2+} -induced shift in V_2 was again determined for the AtTPC1 triple pore mutant EDD, but without statistical significance to AtTPC1-WT (Fig. 3.5d). Taken together, only the neutralization of all three amino acids together (E605Q/D606N/D607N) significantly reduced the susceptibility to inhibitory luminal Ca^{2+} . Thus, these results suggest that the amino acids E605, D606 and D607 near the pore mouth probably work together and are involved in sensing luminal Ca^{2+} .

3.1.4. Effect of AtTPC1 pore mouth mutations on gating charge movement

The TPC1 channel represents a voltage-dependent ion channel, in which conformational changes of the voltage sensor domain regulate channel opening (Guo *et al.*, 2016; Hedrich *et al.*, 1986; Kintzer and Stroud, 2016). The voltage sensor reacts to the membrane voltage like a 'switch', i.e. the transition of the channel from "off" to "on" depends on the change in the electrical field across the membrane. Such dependence on the membrane voltage exists in the channels because gating charges established by charged amino acid

residues respond to changes in the electric field and are then transferred across the membrane (Bezanilla, 2018; Tao *et al.*, 2010). The voltage sensitivity can be described by the equivalent gating charge z which gives the apparent number of gating charges that are moved throughout the membrane when the ion channel opens or closes. Due to my previous studies, AtTPC1 pore mouth mutations, especially the single mutant E605A, D606N and the triple mutant EDD(E605Q/D606N/D607N), significantly shifted voltage-dependent activation of the TPC1 channel to more negative voltage in contrast to AtTPC1-WT in the absence of Ca^{2+} . To further examine whether AtTPC1 pore mouth mutations also affect the voltage sensitivity or not, the number of apparent equivalent gating charges z_1 and z_2 transferred during the assumed conformational transitions $C_1 \rightleftharpoons O$ and $C_2 \rightleftharpoons C_1$, respectively, was derived by the double Boltzmann fits of the G/V curves (section 2.3.6.1.6; Pottosin *et al.*, 2004). When the luminal Ca^{2+} was 0 mM, the z_1 values, reflecting the gating charge movement during the $C_1 \rightleftharpoons O$ transition, were quite similar in AtTPC1-WT and the AtTPC1 pore mouth mutants (Fig. 3.6a). In contrast, the z_2 values describing the gating charge movement during the $C_1 \rightleftharpoons C_2$ transition of the AtTPC1 pore mutants were higher than those of AtTPC1-WT (Fig. 3.6b). This was especially the case for the single mutant E605Q, D606N as well as the triple mutant EDD (E605Q/D606N/D607N). At increased luminal Ca^{2+} level (10 mM), there was no longer a difference between the z_2 values of all AtTPC1 channel mutants and WT (Fig. 3.6a). Interestingly, z_1 values of the AtTPC1 pore mutants appeared to be larger than that of AtTPC1-WT. In particular, the single mutant D606N and triple mutant EDD were characterized by significantly higher z_1 values compared to AtTPC1-WT (Fig. 3.6b). In summary, AtTPC1 pore mouth mutants, especially E605Q, D606N and EDD mutants, apparently moved more equivalent gating charges z_2 during AtTPC1 channel closing and opening at 0 mM luminal Ca^{2+} . When the luminal Ca^{2+} was increased to 10 mM, the equivalent gating charges z_1 of the AtTPC1 pore mutants D606N and EDD were strongly elevated compared to AtTPC1-WT. These results indicate that

the single or triple mutations E605Q, D606N and EDD near the AtTPC1 pore mouth affected the voltage sensitivity of AtTPC1 channel in the absence and presence of luminal Ca^{2+} .

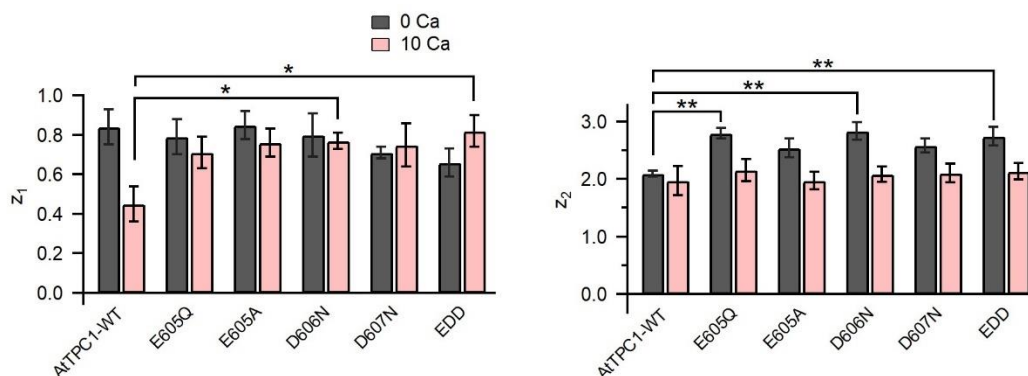


Fig. 3. 6. The gating charge movement of AtTPC1 channel variants.

The number of apparent equivalent gating charges z_1 and z_2 at 0 mM (grey) and 10 mM luminal Ca^{2+} (pink) derived from the double Boltzmann fits of the G(V) curve shown in Fig. 3.4a. Significant differences in the gating charges between the wild type and the channel mutants were analyzed for each Ca^{2+} condition with one-way ANOVA followed by Dunnett's post hoc comparison test. Significant differences between tested groups are indicated by asterisks (* $p < 0.05$; ** $p < 0.01$). Number of experiments for each channel variant for both Ca^{2+} conditions is the same as in Fig. 3.2. EDD represents the triple mutant E605Q/D606N/D607N. All data points are mean values \pm SEM.

3.2. The function of the luminal Ca^{2+} binding sites in *Arabidopsis thaliana* and *Vicia faba*

According to the results above (section 3.1), the amino acids E605/D606/D607 near the AtTPC1 pore mouth likely function as a third luminal Ca^{2+} binding site in TPC1 from *Arabidopsis thaliana*. The other two luminal Ca^{2+} binding sites have been reported to be present with different conservations in higher plants: the luminal Ca^{2+} binding site 1 (Asp454, Glu528, Asp240) are very conserved, while the amino acids from site 2 (Glu239, Glu457, Asp240) show some diversity (Dreyer *et al.*, 2021). Given now the fact that TPC1/SV currents have been recorded from *Vicia faba* guard cell vacuoles even under extremely high luminal Ca^{2+} loads (50 mM) (Ward and Schroeder, 1994), the TPC1 channel

variants of *Vicia faba* and *Arabidopsis thaliana* may differ in their luminal Ca^{2+} sensitivity. Therefore, to gain initial insights in this structural and functional diversity of TPC1 channels, it was first examined whether these two species may differ in their luminal Ca^{2+} binding sites at polymorphic sites. For this, the TPC1-like amino acid sequences from Brassicaceae and Fabaceae with respect to the total three luminal Ca^{2+} binding sites was aligned (Fig. 3.7). Among the 11 aligned Brassicaceae TPC1 channels, the known Ca^{2+} binding sites 1 and 2 are fully conserved, the same is also almost true for Ca^{2+} binding site 3: only two out of the 11 Brassicaceae TPC1 channels (BrTPC1, LeTPC1) show a neutralization of a residue at a site homologous to AtTPC1-Asp506. In comparison, the tested fabacean TPC1 channels show some neutralizations at polymorphic sites within Ca^{2+} binding sites 2 and 3. The negatively charged Glu457 of AtTPC1 was often replaced by the neutral charged asparagine (N) at the homologous site in the fabacean channels. Remarkably, this Glu457Asn polymorphism was additionally accompanied by the neutralization of one or two negatively charged residues within the Ca^{2+} binding site at the luminal pore entrance (site 3). For instance, a hallmark triple polymorphism of AtTPC1 was present in the faba bean TPC1 channel which harbored either alanine (A) or asparagine (N) at the homologous sites (Asn458, Ala607, Asn608). Thus, these variations in the luminal Ca^{2+} binding sites suggest that VfTPC1 indeed could exhibit a different luminal Ca^{2+} sensitivity compared to AtTPC1. To further prove this assumption, in the following I examined the luminal Ca^{2+} dependency of VfTPC1 channel gating in patch-clamp experiments compared with AtTPC1.

Ca ²⁺ sensor sites		1/2			3		
Brassicaceae	AtTPC1	239	E D	454 D I E E	528 E	605 E D D	
	CgTPC1	238	E D	453 D I E E	527 E	604 E D D	
	AhTPC1	238	E D	453 D I E E	527 E	604 E D D	
	BsTPC1	238	E D	453 D I E E	527 E	604 E D D	
	AlyTPC1	238	E D	453 D I E E	527 E	604 E D D	
	AliTPC1	239	E D	454 D I E E	528 E	605 E D D	
	TaTPC1	239	E D	454 D I E E	528 E	605 E E D	
	BoTPC1	242	E D	457 D I E E	531 E	608 E E D	
	BrTPC1	239	E D	454 D I E E	528 E	605 E N D	
	IaTPC1	240	E D	455 D I E E	529 E	606 E D D	
	LeTPC1	239	E D	454 D I E E	528 E	605 E N D	
	AnTPC1	239	E D	454 D I E E	528 E	605 E D D	
	Fabaceae	VfTPC1	241	E D	455 D I E N	530 E	607 A N D
		LsTPC1	241	E D	455 D I E N	530 E	607 A N D
TpTPC1		240	E D	454 D V E E	529 E	606 A N D	
MtTPC1		241	E D	455 D V E D	530 E	607 A N D	
CaTPC1		240	E D	454 D I E N	529 E	606 V N D	
LjTPC1		242	E D	456 D I Q E	531 E	607 A N D	
PITPC1		241	E D	455 D I E N	530 E	607 E N D	
GmTPC1		241	E D	455 D I E N	530 E	607 E N D	
LaTPC1		240	E D	454 D I Q N	528 E	605 D N D	
PvTPC1		241	E D	455 D I E N	530 E	607 E N D	
VuTPC1		241	E D	455 D I E N	530 E	607 E N D	
AiTPC1		241	E D	455 D I Q N	529 E	606 D N D	
BtTPC1		240	E D	454 D I E N	528 E	605 D D D	
CoTPC1		224	E D	436 D V E D	510 E	587 D N D	
			* *	* : . .	*	. . *	

Fig. 3. 7. Polymorphism of functional TPC1 channel domains with a role in luminal Ca²⁺ coordination.

Sequence alignment of the three luminal Ca²⁺ sensing sites in TPC1 channels from the species Brassicaceae and Fabaceae. The different color code represented the different amino acids. "*" means that the residues in that column are identical in all sequences in the alignment. ":" means that conservative substitutions have been observed. "." means that non-conservative substitutions are observed. TPC1 sequences from following species were used: *Arabidopsis thaliana* (AtTPC1), *Capsella grandiflora* (CgTPC1), *Arabidopsis halleri* (AhTPC1), *Boechera stricta* (BsTPC1), *Arabidopsis lyrata* (AlyTPC1), *Alyssum linifolium* (AliTPC1), *Thlaspi arvense* (TaTPC1), *Brassica oleracea* (BoTPC1), *Brassica rapa* (BrTPC1), *Iberis amara* (IaTPC1), *Lepidium sativum* (LeTPC1), *Arabis nemorensis* (AnTPC1), *Vicia faba* (VfTPC1), *Lathyrus sativus* (LsTPC1), *Trifolium pratense* (TpTPC1), *Medicago truncatula* (MtTPC1), *Cicer arietinum* (CaTPC1), *Lotus japonicus* (LjTPC1), *Phaseolus lunatus* (PITPC1), *Glycine max* (GmTPC1), *Lupinus albus* (LaTPC1), *Phaseolus vulgaris* (PvTPC1), *Vigna unguiculata* (VuTPC1), *Arachis ipaensis* (AiTPC1), *Bauhinia tomentosa* (BtTPC1), *Copaifera officianalis* (CoTPC1).

3.2.1. Electrical properties of *Vicia faba* TPC1

3.2.1.1. The subcellular localization of VfTPC1 channel

In order to define the electrical properties of VfTPC1, the vacuolar localization of VfTPC1 first had to be confirmed. To this end, I subcloned the VfTPC1 coding sequence into an eYFP-vector to express VfTPC1 under the control of the UBQ10 promoter instead of the 35S promoter (section 2.1.3). Using this UBQ10::VfTPC1 construct for the transient protoplast transformation, the transformation efficiency was highly increased. As a result, the vacuolar localization of VfTPC1 could be defined. Using confocal laser scanning microscopy, the VfTPC1 channels were found to localize exclusively to the vacuole membrane, as visualized by the fluorescent signal of the eYFP-tag fusion to the C-terminus of VfTPC1 (Fig. 3.8).

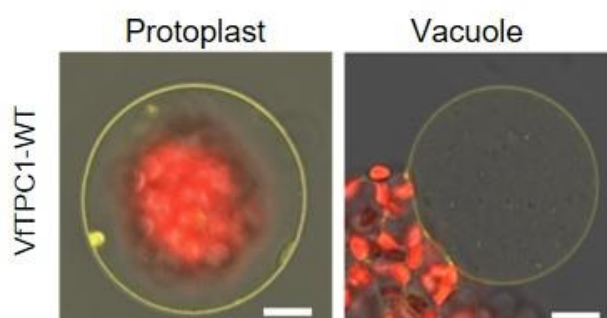


Fig. 3. 8. The localization of *Vicia faba* TPC1 channels.

Mesophyll protoplasts from the *attpc1-2* and released vacuoles after transient transformation with eYFP-tagged UBQ10::VfTPC1-WT channel construct. Bright field and fluorescent images were merged. Red fluorescence corresponds to chloroplast autofluorescence. The yellow fluorescence represents the eYFP fluorescence, Scale bars = 10 μm .

3.2.1.2. The functional features of VfTPC1 channel

Since VfTPC1 was correctly targeted to the vacuole membrane, VfTPC1 could be successfully characterized in patch-clamp experiments. For that, the whole-vacuole configuration was again established under symmetrical 150 mM K^+ conditions with 0 mM luminal Ca^{2+} . Under these conditions, macroscopic outward-rectifying SV/TPC1-like currents were elicited from VfTPC1-WT

transformed vacuoles upon application of depolarizing voltage pulses (Fig. 3.9a). These current recordings indicated that VfTPC1 channel was also functional in the background of *Arabidopsis thaliana attpc1-2* vacuoles. Therefore, I was able to further study and compare the channel properties of VfTPC1 with those of AtTPC1 in terms of activation and deactivation kinetics, voltage dependence and luminal calcium sensitivity.

3.2.1.2.1. The activation and deactivation kinetics of VfTPC1

In the absence of luminal Ca^{2+} , the activation of VfTPC1-WT channel appeared to be much faster than that of AtTPC1-WT outward currents in the range of +40 mV to +110 mV (Fig. 3.9a). Therefore, the half-activation times $t_{\text{act-0.5}}$ were determined for both channel types (Fig. 3.9b). $t_{\text{act-0.5}}$ of VfTPC1 was in the range of 30-60 ms in the applied voltage range. In contrast, $t_{\text{act-0.5}}$ of AtTPC1 was 90-215 ms in response to voltage pulses in the same range. Thus, more than 3-fold faster half-activation times were derived for VfTPC1-WT currents compared with AtTPC1-WT currents (Fig. 3.9b). For instance, a $t_{\text{act-0.5}}$ value of 39.1 ± 3.6 ms was determined for VfTPC1-WT at +80 mV which was obviously about 3-fold smaller than that of AtTPC1-WT ($t_{\text{act-0.5}} = 120.4 \pm 22.9$ ms). In a previous work on *Arabidopsis thaliana* TPC1 channels, $t_{\text{act-0.5}}$ was 19.0 ± 2.7 ms at +80 mV for the hyperactive AtTPC1 channel mutant *fou2* but 100 ± 7.8 ms for AtTPC1-WT (Jaslan *et al.*, 2016). These results suggest that VfTPC1 is a fast activating channel like the *fou2* channel (Dadacz-Narloch *et al.*, 2013; Jaślan *et al.*, 2016).

In contrast to the activation kinetics, the deactivation times of VfTPC1 channels at -60 mV appeared to be much longer than those of AtTPC1 channel (Fig. 3.9a). For detailed quantification, I also analyzed the half-deactivation times $t_{\text{deact-0.5}}$ over a broad voltage range (Fig. 3.9d). For this, after pre-activation of TPC1 currents upon an instantaneous voltage pulse to either +80 mV or +100 mV, the current relaxation was recorded at voltages from -60 to 0 mV, and the

corresponding half-deactivation times ($t_{\text{deact-0.5}}$) were determined (section 2.3.6.1.8). For AtTPC1-WT, a half-deactivation time $t_{\text{deact-0.5}}$ of about 7-24 ms was determined in the range of -10 mV to -60 mV. In comparison, $t_{\text{deact-0.5}}$ of VfTPC1 varied between 30-54 ms in the same voltage range, which was more than 2-times higher than AtTPC1-WT (Fig. 3.9d). Thus, VfTPC1 deactivates slower than AtTPC1.

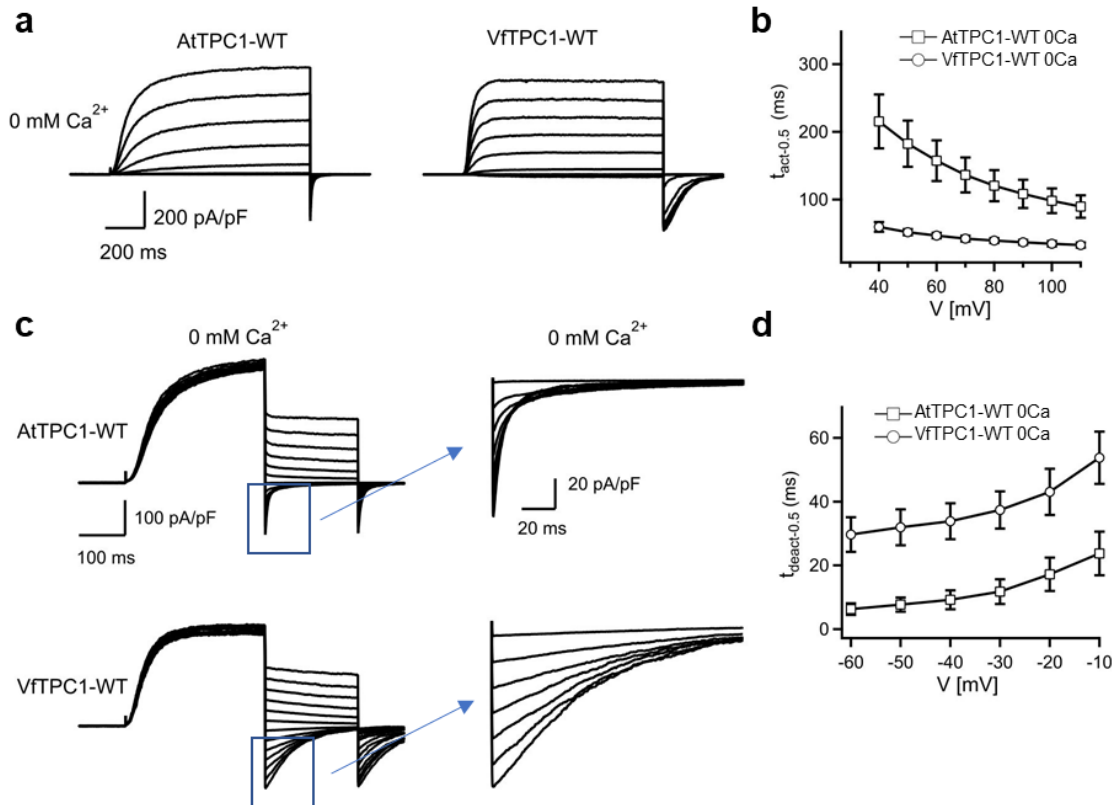


Fig. 3. 9. The activation and deactivation of *Arabidopsis thaliana* TPC1 and *Vicia faba* TPC1 channels.

(a) Activating macroscopic TPC1 currents recorded from mesophyll vacuoles transformed with either AtTPC1-WT or VfTPC1-WT channel at 0 mM luminal Ca^{2+} . TPC1 currents were monitored in response to depolarizing voltages pulses of -80 mV to +110 mV in 20 mV increments at indicated luminal Ca^{2+} concentrations. The holding voltage was -60 mV. **(b)** Half-activation times ($t_{\text{act-0.5}}$) of the AtTPC1-WT and VfTPC1-WT were determined from (a). **(c)** Deactivating TPC1 currents were monitored in response to voltages pulses of -60 mV to +60 mV in 10 mV decrements after pre-activation of TPC1 currents upon a voltage pulse of either +80 mV or +100 mV at 0 mM Ca^{2+} concentrations. **(d)** Half-deactivation times ($t_{\text{deact-0.5}}$) of the AtTPC1-WT and VfTPC1-WT were calculated from deactivating TPC1 currents. The experiments for channel activation with AtTPC1-WT are identical with those shown in section 3.1. The number of experiments (n) for channel activation $n_{0\text{Ca}}=5$ for VfTPC1-WT. The number of experiments was for channel deactivation $n_{0\text{Ca}}=5$ for AtTPC1-WT, $n_{0\text{Ca}}=4$ for VfTPC1-WT. All data points are mean \pm SEM.

3.2.1.2.2. The voltage dependence of the VfTPC1 channel

A closer look at the current-voltage curves ($I_{ss}/C_m(V)$) further revealed that besides the outward currents, inward currents were also elicited upon voltage pulses in the range of -40 and 0 mV from vacuoles that harbored VfTPC1-WT but not AtTPC1-WT (Fig. 3.10a, b). This indicated a shift in the voltage activation threshold for VfTPC1-WT channel opening by about 30 mV to more negative voltages. For further quantification, the conductance-voltage curve ($G/G_{max}(V)$) was also determined for VfTPC1, confirming a negative-going shift of the VfTPC1-WT GV curve compared to AtTPC1-WT (Fig. 3.10c). When the GV curves were fitted with double Boltzmann equation (Fig. 3.10c), the derived midpoint activation voltages V_1 and V_2 describing the transitions between the different channel states (C_1 , C_2 , O) were significantly different between VfTPC1 and AtTPC1 (Fig. 3.10d). The V_1 values for VfTPC1 was -3.5 ± 12.3 mV, which was about 55 mV more negative than the V_1 value of AtTPC1-WT (51.2 ± 9.6 mV). The corresponding V_2 values for VfTPC1-WT and AtTPC1-WT were 11.6 ± 3.2 mV and 24.0 ± 3.8 mV, respectively. Thus, the voltage activation threshold of VfTPC1-WT channel was strongly shifted to more negative voltages compared to that of AtTPC1 channel (Fig. 3.10d). These results were comparable with the *fou2* channel (Jašlan *et al.*, 2016), as the similar midpoint activation voltage V_1 of 60 ± 4.6 mV and 9 ± 1.1 mV was reported for wild type AtTPC1 and *fou2*, respectively. These results indicate that the voltage-dependent activation of VfTPC1-WT is similar to that of the hyperactive channel *fou2* (Beyhl *et al.*, 2009; Hedrich and Marten, 2011; Hedrich *et al.*, 2018).

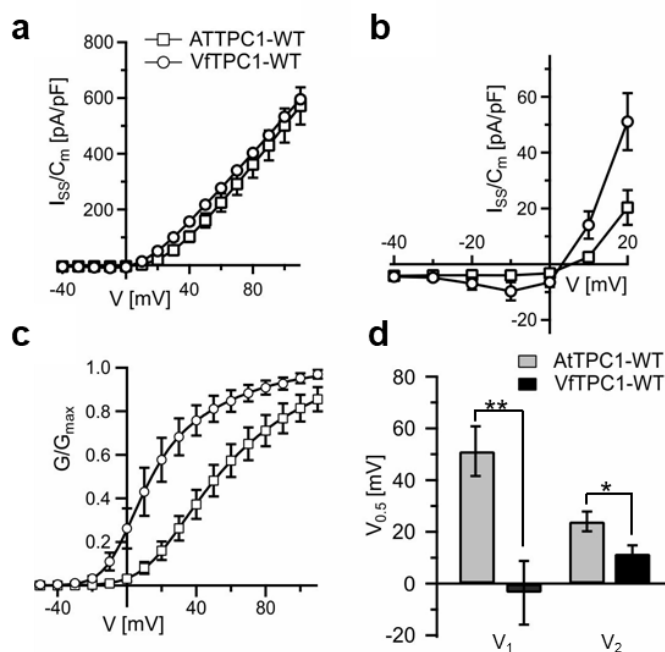


Fig. 3. 10. The voltage dependence of TPC1 channel from *Vicia faba* and *Arabidopsis thaliana*.

(a) Normalized steady-state currents ($I_{ss}/C_m(V)$) plotted against the clamped membrane voltages (V) in the absence luminal Ca^{2+} . (b) Enlarged section of the current-voltage curve ($I_{ss}/C_m(V)$) for AtTPC1-WT and VfTPC1-WT channel shown in (a). (c) Normalized conductance-voltage curves ($G/G_{max}(V)$) of AtTPC1-WT and VfTPC1-WT was defined at 0 mM luminal Ca^{2+} . (d) Midpoint activation voltages V_1 and V_2 were derived from the double Boltzmann fits of the $G(V)$ curves shown in (c). Significant differences were analyzed for the $V_{1/2}$ values between AtTPC1-WT and VfTPC1-WT with Student's t -test (* $p < 0.05$, ** $p < 0.01$). Number of experiments for VfTPC1-WT is the same as in Fig. 3.9. The data for AtTPC1-WT are identical to those shown in section 3.1. All data points are mean values \pm SEM.

3.2.1.2.3. The effect of the luminal Ca^{2+} inhibition on VfTPC1 channel

When the luminal Ca^{2+} concentration was increased from 0 to 10 mM or 50 mM Ca^{2+} , the TPC1 current amplitudes of both natural channel variants decreased, but to different extents (Fig. 3.11a). Compared with AtTPC1, the Ca^{2+} -induced reduction in the VfTPC1 currents, however, was much less pronounced (Fig. 3.11a). Therefore, in comparison with AtTPC1-WT, the current densities ($I_{ss}/C_m(V)$) were analyzed with VfTPC1-WT (Fig.3.11b). The current densities ($I_{ss}/C_m(V)$) determined from AtTPC1-WT vacuoles were reduced by about 60% at +110 mV in the presence of 10 mM Ca^{2+} compared to Ca^{2+} -free conditions. A same high luminal Ca^{2+} level (10 mM), however, caused only a decrease in

the VfTPC1-WT currents by approximately 20% (Fig. 3.11b). Even more, the AtTPC1-WT currents were completely blocked when the luminal Ca^{2+} was further raised to 50 mM luminal Ca^{2+} . However, at 50 mM Ca^{2+} , the VfTPC1 current density still reached about 50% of the current density measured under luminal Ca^{2+} -free conditions (Fig. 3.11). In summary, VfTPC1 behaved more tolerant to inhibitory luminal Ca^{2+} than AtTPC1.

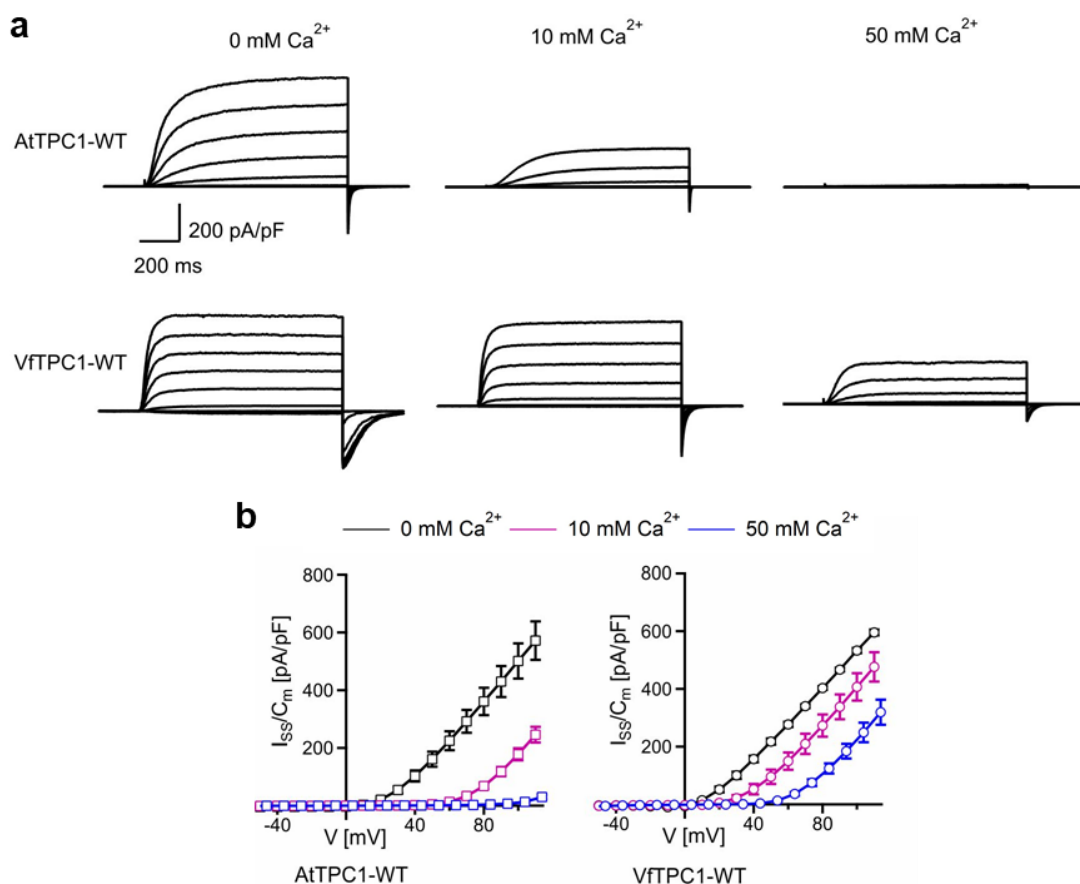


Fig. 3. 11. The current responses of vacuoles harboring either *Arabidopsis thaliana* TPC1 or *Vicia faba* TPC1 channels under low and high luminal Ca^{2+} .

(a) Macroscopic TPC1 currents were monitored in response to depolarizing voltages pulses of -80 mV to +110 mV at indicated luminal Ca^{2+} concentrations. **(b)** Normalized steady-state currents ($I_{ss}/C_m(V)$) plotted against the membrane voltages (V) in the presence (10 mM, 50 mM) and absence of luminal Ca^{2+} . The data for AtTPC1-WT at 0 and 10 mM Ca^{2+} are identical to those shown in section 3.1. The data for VfTPC1-WT at 0 mM Ca^{2+} are same as those shown in Fig. 3.9-3.10. AtTPC1-WT $n_{50\text{Ca}}=4$; VfTPC1-WT $n_{10/50\text{Ca}} = 6$. All data points are mean values \pm SEM.

Furthermore, in order to prove that VfTPC1-WT channel is insensitive to high luminal Ca^{2+} compared to AtTPC1-WT channel, the conductance-voltage

curves ($G/G_{\max}(V)$) and the midpoint activation voltage V_1 and V_2 were analyzed (Fig. 3.12). Compared to 0 mM Ca^{2+} , at 10 mM Ca^{2+} the midpoint activation voltages V_1 and V_2 value shifted by about 115 mV and 61 mV for AtTPC1 but only by about 61 mV and 26 mV for VtTPC1, respectively, to more positive voltages (Fig. 3.12b, c, d, e). When the luminal Ca^{2+} increased from 10 to 50 mM, a further positive-going shift of the conductance-voltage curve ($G/G_{\max}(V)$) was observed with VtTPC1-WT, as indicated by a 40 mV- and 23 mV-rise in V_1 and V_2 , respectively (Fig. 3.12b, c, d, e). However, the AtTPC1 currents were too small at 50 mM luminal Ca^{2+} (Fig. 3.11a) to reliably determine the conductance-voltage curves ($G/G_{\max}(V)$). In summary, these results clearly document that (i) VtTPC1-WT can much better tolerate high luminal Ca^{2+} than AtTPC1-WT and (ii) VtTPC1 represents a native hyperactive TPC1 channel as the artificial hyperactive channel *fou2*.

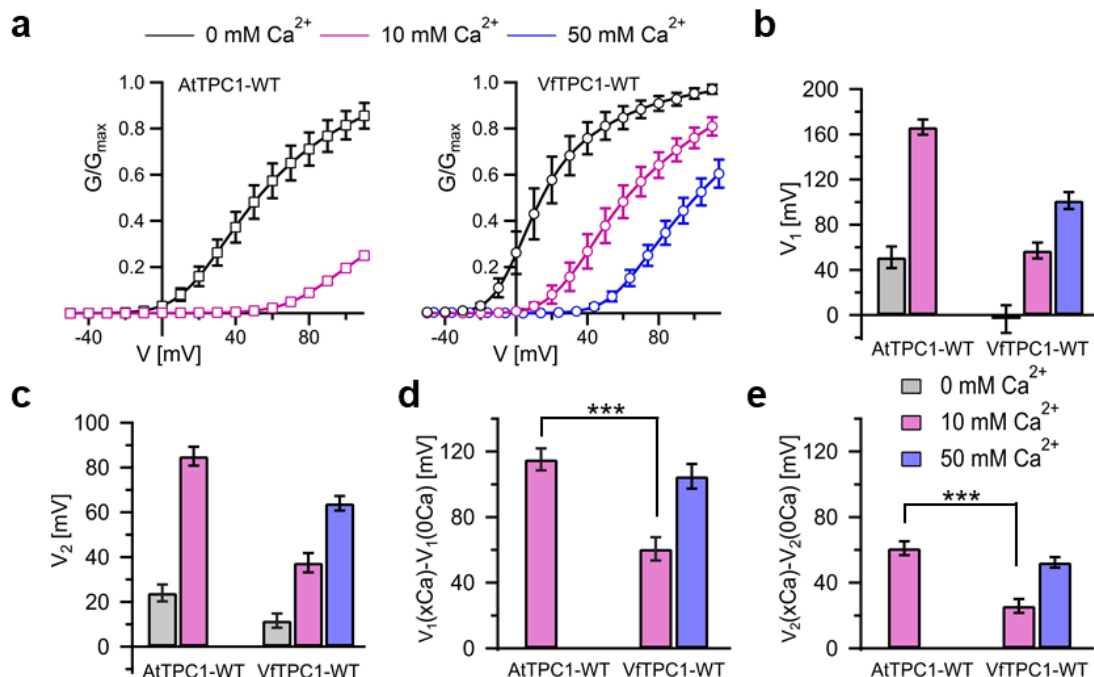


Fig. 3. 12. The voltage dependence of TPC1 channels from *Vicia faba* and *Arabidopsis thaliana* under low and high luminal Ca^{2+} .

(a) Normalized conductance-voltage curves ($G/G_{\max}(V)$) of AtTPC1-WT and VtTPC1-WT in the presence (10 mM, 50 mM) and absence of luminal Ca^{2+} . (b, c) Midpoint activation voltages V_1 and V_2 in the presence of 0 mM, 10 mM and 50 mM Ca^{2+} in the vacuole lumen. Significant differences were only analyzed for $V_{1/2}$ values under 0 mM luminal Ca^{2+} conditions with one-way ANOVA followed by Dunnett's post hoc comparison test. (d, e) Changes in $V_{1/2}$ values upon a rise in luminal Ca^{2+} from 0 to 10 mM. Significant differences tested with Student's *t*-test (***) p

< 0.001). The data for AtTPC1-WT at 0 mM and 10 mM Ca²⁺ are identical to those shown in section 3.1. The data for VfTPC1-WT at 0 mM Ca²⁺ are same as those shown in Fig. 3.10. The number of experiments for AtTPC1-WT under 50 mM Ca²⁺ and VfTPC1-WT under indicated Ca²⁺ conditions is the same as in Fig.3.11. All data points are mean values ± SEM.

3.2.1.2.4. Effect of VfTPC1 channels on the excitability of vacuoles

Recently, the electrical excitability of the vacuole membrane in *Arabidopsis thaliana* was studied (Jaślan *et al.*, 2019). It was shown that TPC1 plays a key role for vacuole membrane excitability which was influenced by its channel activity. The hyperactivity of the AtTPC1 channel mutant *fou2* led to hyperexcitability of the vacuole (Jaślan *et al.*, 2019). Since VfTPC1-WT exhibited *fou2*-like hyperactive channel characteristics (section 3.2.1), it was interesting to test the effect of VfTPC1-WT on vacuolar excitability. For this, current clamp experiments in the whole-vacuole configuration (Jaślan *et al.*, 2019) were conducted with vacuoles released from *attpc1-2* mesophyll protoplasts transiently transformed with either VfTPC1-WT or AtTPC1-WT. Under natural conditions the free Ca²⁺ level in the vacuolar lumen appears to be in the range of 0.2–2 mM (Schonknecht, 2013). Thus, to mimic more physiological luminal Ca²⁺ conditions, the electrical polarization of the vacuole membrane was measured in the presence of 0.2 mM luminal Ca²⁺. For TPC1-dependent vacuolar excitation, instantaneous current injection pulses ranging from 10 up to 1000 pA were applied to the vacuole membrane from a holding voltage of -60 mV. The vacuole membrane responded to the current injections with a highly depolarized voltage stimulus peak ($V_{\text{stimulus peak}}$) which quickly relaxed to a less depolarized voltage stimulus plateau ($V_{\text{stimulus-plateau}}$) that persisted until the end of the injection pulse (section 2.3.6.2.2, Fig 3.13a, b). After injection, the vacuole membrane remained a post-stimulus depolarized plateau phase for a short time before relaxed to the holding voltage. As illustrated in Figure 3.13a, c, at a current injection of 10 pA, the lifetime of the post-stimulus plateau phase (t_{plateau}) was very small (~0.06 s) with AtTPC1-WT vacuoles, and even at the highest current injection (1 nA), the lifetime t_{plateau}

was still less than 0.5 s. In contrast, t_{plateau} was 10 s in VfTPC1-WT vacuoles even with the lowest injected current (10 pA). In other words, at 10 pA, the vacuoles transformed with VfTPC1-WT channels already remained depolarized during the entire recording period of 10 s (Fig. 3.13b, c). In addition, both the voltage stimulus peak ($V_{\text{stimulus peak}}$) and in particular the voltage stimulus-plateau ($V_{\text{stimulus-plateau}}$) appeared more depolarized with AtTPC1-WT channel than with the VfTPC1-WT channel (Fig. 3.13d, e). These results indicate that VfTPC1-WT equipped vacuoles were also hyperexcitable, behaving very much like the *fou2* vacuoles.

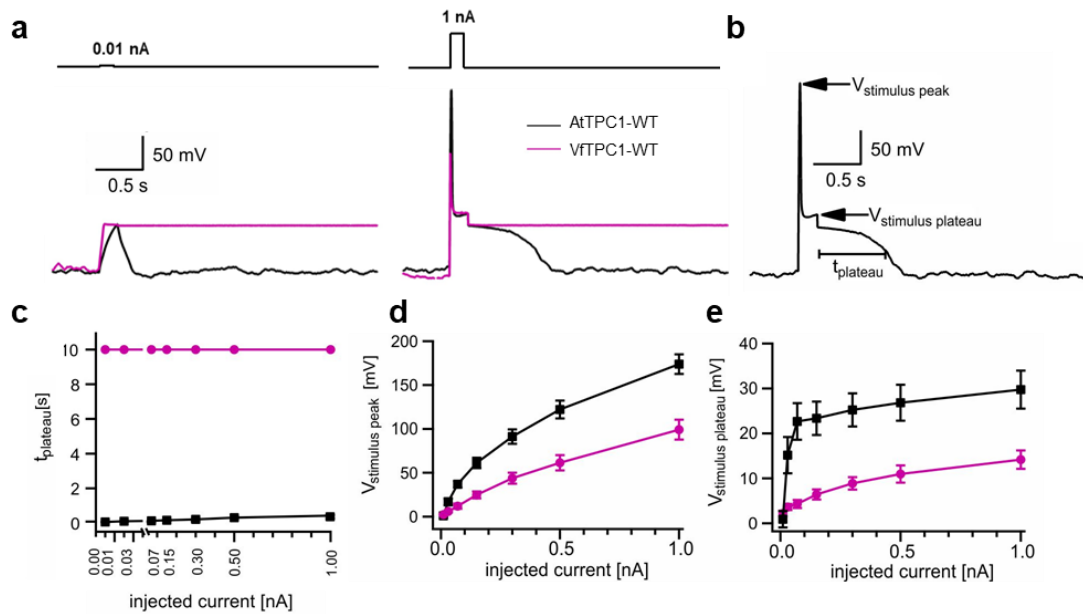


Fig. 3. 13. Dependency of vacuole excitability on species-dependent TPC1 channel variants.

(a) Representative membrane voltage responses of vacuoles to current injections (10 and 1000 pA) of 300 ms duration. (b) The current-induced voltage responses were analyzed with respect to the stimulus spike ($V_{\text{stimulus spike}}$), the stimulus plateau ($V_{\text{stimulus plateau}}$) and the lifetime of the post-stimulus plateau phase (t_{plateau}). (c) Lifetime of the post-stimulus depolarization phase plotted against the corresponding injected current pulse. (d, e) Amplitudes of stimulus peak (d) and stimulus plateau (e) voltages during current injection recorded from vacuoles equipped with the indicated TPC1 channel variants. Number of experiments for each channel type was $n = 6$. All data points are means \pm SEM.

3.2.2. The luminal Ca²⁺ sensor residues in Fabaceae and Brassiceae

The VfTPC1 channel properties differed from that of AtTPC1; the Fabaceae channel type behaved like the hyperactive Arabidopsis TPC1 channel *fou2* that contained an impaired luminal Ca²⁺ binding site. The amino acid sequence alignment revealed (section 3.2, Fig.3.7) that the negatively charged amino acids Glu457, Glu605 and Asp606 involved in luminal Ca²⁺ sensing in AtTPC1 were replaced by the neutral residues like aspartate and glutamate at homologous sites in VfTPC1 (Asn458, Ala607, Asn608). Therefore, it was important to know whether the amino acid polymorphism at these luminal Ca²⁺ sensing sites (Fig.3.7) defines the different channel activity of VfTPC1 and AtTPC1. To this end, by replacing the E605 and D606N in the luminal Ca²⁺ sensing site 3 of AtTPC1 with the corresponding homologue sites A605 and D606 of VfTPC1, a double AtTPC1 mutant (E605A/D606N) was generated to dissect whether the luminal Ca²⁺ sensing site 3 alone could convert AtTPC1 to the hyperactive VfTPC1 channel type. In parallel, a triple AtTPC1 mutant (E457N/E605A/D606N) was also generated by replacing all three polymorphic sites of AtTPC1 (E457, E605 and D606) with the corresponding homologue sites of VfTPC1 to dissect whether the triple or double polymorphic sites are necessary for defining the hyperactive property of VfTPC1. In the other way around, a triple VfTPC1 mutant (N459E/A607E/N608D) was also generated by replacing of N459, A607 and N608 of VfTPC1 with the corresponding homologue sites of AtTPC1 to dissect whether the VfTPC1 mutant will lose its hyperactive feature and behave more like AtTPC1. After transient transformation of the Arabidopsis TPC1-loss-of-function mutant *tpc1-2* with these channel mutants, the localization and the features of these different TPC1 mutants were then studied again with patch-clamp technique.

3.2.2.1. Electrophysiological characterization of the AtTPC1 double/triple mutants E605A/D606N and E605A/D606N/E457N

Similar with AtTPC1-WT, both the double and triple mutants (E605A/D606N, E457N/E605A/D606N, respectively) were properly targeted to the vacuole membrane of *attpc1-2* (Fig. 3.14a) and gave also rise to the typical SV/TPC1 channel currents upon depolarization (Fig.3.14b) in the absence of luminal Ca^{2+} . Thus, these mutations did not destroy AtTPC1 channel function, so that the electrical properties of the double mutant (E605A/D606N) and triple mutant (E457N/E605A/D606N) could be characterized in more detail.

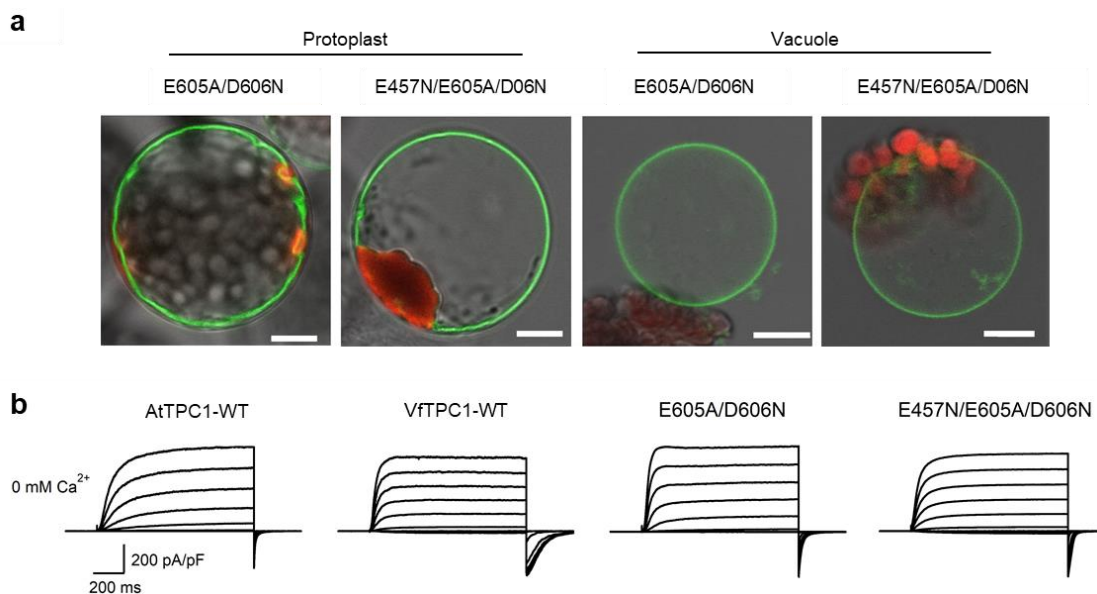


Fig. 3. 14. Subcellular localization and electrophysiological characterization of AtTPC1 channel variants under 0 mM luminal Ca^{2+} conditions.

(a) Confocal images of mesophyll protoplasts and released vacuoles from the *tpc1-2* transiently transformed with the indicated AtTPC1 channel variants. The green fluorescence signal was restricted to the vacuole membrane. Fluorescent images and bright field images were merged. Scale bar = 10 μm . (b) Macroscopic current responses of individual vacuoles to different voltage pulses applied in the range of -80 to +110 mV in 10 mV increments in absence of luminal Ca^{2+} . The experiments of AtTPC1-WT and VfTPC1-WT shown here are the same as in section 3.2.1. The experiment number was $n_{0\text{Ca}} = 5$ AtTPC1 -E605A/D606N and $n_0 = 5$ for AtTPC1 triple mutant-E457N/E605A/D606N.

A closer look at the current-voltage curves ($I_{\text{ss}}/C_m(V)$) further revealed that besides the outward currents, inward currents were also elicited upon voltage pulses in the range of -30 and 0 mV from vacuoles that harbored VfTPC1-WT

but not AtTPC1-WT (Fig. 3.10a, b). This indicated a shift in the voltage activation threshold for VfTPC1-WT channel opening by about 30 mV to more negative voltages

In the absence of luminal Ca^{2+} , the current densities of AtTPC1 double (E605A/D606N) and triple mutant (E457N/E605A/D606N) which were elicited in response to the applied voltages, were similar with AtTPC1-WT as well as VfTPC1-WT (Fig. 3.15a). However, a closer look at the IV curve at negative voltages revealed that vacuoles decorated with the AtTPC1 double and triple mutants showed inward current responses to voltage pulses from -30 to 0 mV. This observation pointed to a shift of the voltage activation threshold of AtTPC1 double and triple mutant compared with wild type AtTPC1 to more negative voltages by about 30 mV, just as with VfTPC1 (Fig. 3.15b). To further quantify the affected voltage activation threshold, the conductance-voltage curves ($G/G_{\text{max}}(V)$) of the TPC1 channel variants were described with double Boltzmann fits (Fig. 3.15c). Based on this, the midpoint voltage V_1 of the AtTPC1 double (6.9 ± 5.5 mV) and the triple mutant (0.4 ± 14.2 mV) was close to that of VfTPC1 with -3.5 ± 12.3 mV (Fig. 3. 15d). Thus, compared with the V_1 value of AtTPC1 (51.2 ± 9.6 mV), the voltage dependence of AtTPC1 double (E605A/D606N) and triple (E457N/E605A/D606N) mutants was negatively shifted by about 44 mV and 55 mV, respectively, and thus was similar to that of VfTPC1 (55 mV). Similarly, V_2 values of the AtTPC1 double and triple mutants were also decreased in a VfTPC1-like manner compared to AtTPC1-WT (Fig. 3. 15d). The V_2 values for AtTPC1 double and triple mutants were 12.0 ± 1.9 mV and 6.2 ± 3.4 mV, respectively, and thus close to that of VfTPC1-WT (11.6 ± 3.2 mV). These results indicated that the voltage-dependent activation of AtTPC1 double (E605A/D606N) and triple (E457N/E605A/D606N) mutants were moved to more negative potentials, and mimicked that of VfTPC1-WT.

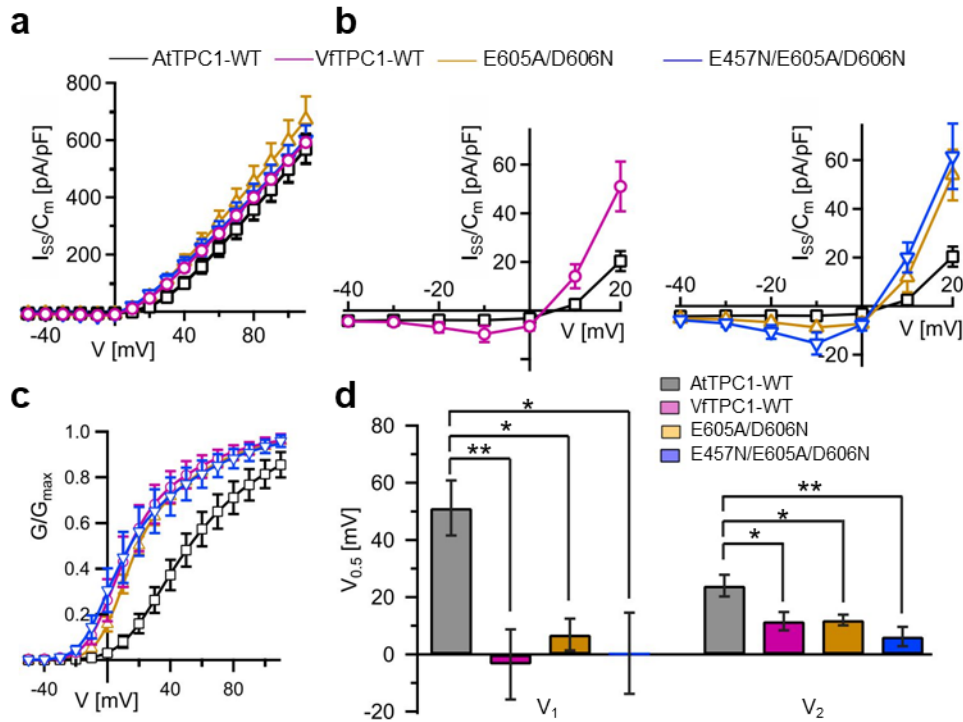


Fig. 3. 15. The voltage dependence of TPC1 channel variants.

(a) Normalized steady-state currents ($I_{ss}/C_m(V)$) plotted against the clamped membrane voltages (V) in the absence of luminal Ca^{2+} . (b) Enlarged section of the current-voltage curves ($I_{ss}/C_m(V)$) for TPC1 channel variants shown in (a). (c) Normalized conductance-voltage curves ($G/G_{max}(V)$) of TPC1 channel variants defined at 0 mM luminal Ca^{2+} . (d) Midpoint activation voltages V_1 and V_2 were derived from the double Boltzmann fits of the $G(V)$ curves shown in (c). Significant differences were only analyzed for $V_{1/2}$ values under luminal Ca^{2+} -free conditions with one-way ANOVA followed by Dunnett's post hoc comparison test (* $p < 0.05$, ** $p < 0.01$). The data of AtTPC1-WT and VfTPC1-WT showed here are same as section 3.2.1. The number experiments of the other TPC1 channel variants were the same as in Fig. 3.14. All data points are means \pm SEM.

In addition, the half-activation times ($t_{act-0.5}$) of AtTPC1 double (E605A/D606N) and triple (E457N/E605A/D606N) mutants behaved more VfTPC1-like (Fig. 3.16a, b). The half-activation time $t_{act-0.5}$ of the double mutant was in the range of 49-100 ms in response to the activating voltages such as 40 up to 110 mV. Almost over this entire voltage range i.e. from 40 to 90 mV, the $t_{act-0.5}$ value was significantly lower for the AtTPC1 double mutant than for AtTPC1-WT (Fig. 3.16a, b). The $t_{act-0.5}$ of AtTPC1 triple mutant was in the range of 65-118 ms in response to the applied voltage from 40 to 110 mV, which was similar with that of AtTPC1 double mutant. Therefore, the $t_{act-0.5}$ of AtTPC1 double and triple was

close to that of VfTPC1 in the range of 30-60 ms over the applied voltages.

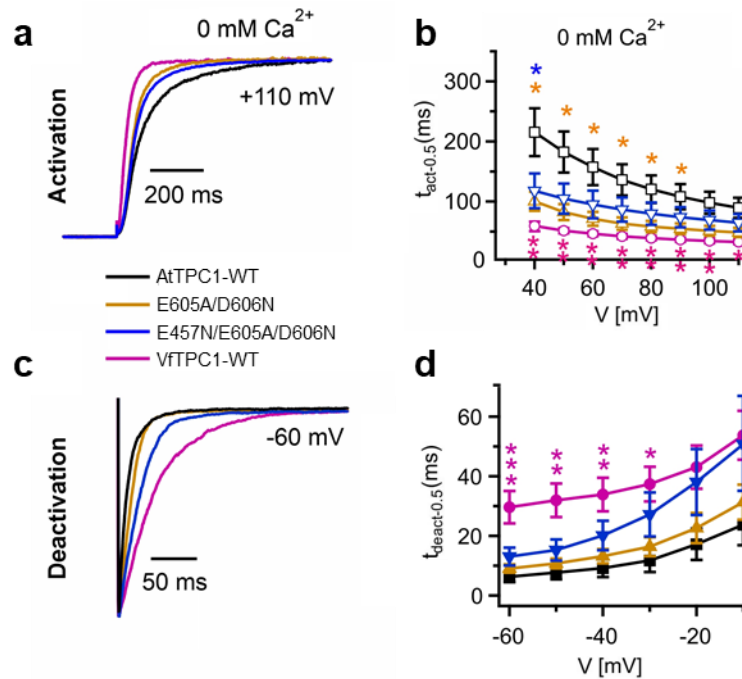


Fig. 3. 16. Activation and deactivation kinetics of AtTPC1 channel variants.

(a) Representative current relaxation induced upon a voltage pulse from -60 mV to +110 mV at 0 mM luminal Ca^{2+} . (b) Half-activation times ($t_{\text{act-0.5}}$) of the TPC1 currents plotted against the respective membrane voltages at 0 mM luminal Ca^{2+} . (c) Representative current relaxation induced upon a voltage pulse from +80 mV or +100 mV to -50 mV at 0 mM luminal Ca^{2+} . (d), Half-deactivation times ($t_{\text{deact-0.5}}$) of the TPC1 currents against the respective membrane voltages at 0 mM Ca^{2+} . In (b, d) significant differences between AtTPC1-WT and other TPC1 channel variants were analyzed for $t_{\text{de/act-0.5}}$ values under luminal Ca^{2+} -free conditions with one-way ANOVA followed by Dunnett's post hoc comparison test (* $p < 0.05$, ** $p < 0.01$, *** $p < 0.001$). The data of AtTPC1-WT and VfTPC1-WT showed here are same as section 3.2.1. The number experiments for channel activation with AtTPC1-E605A/D606N and AtTPC1-E457N/E605A/D606N are same as shown in Fig.3.14. The number experiments for channel deactivation with AtTPC1-E605A/D606N $n_{0\text{Ca}} = 4$ and AtTPC1-E457N/E605A/D606N $n_{0\text{Ca}} = 4$. All data points are means \pm SEM.

Furthermore, the half-deactivation time $t_{\text{deact-0.5}}$ for AtTPC1 double mutant (E605A/D606N) for the deactivating voltages from -60 to -10 mV were in the range of 10-30 ms and therefore was similar with AtTPC1-WT (7-24 ms). In contrast, $t_{\text{deact-0.5}}$ of 30-54 ms for VfTPC1-WT with was significantly larger than AtTPC1-WT (Fig. 3.16c, d). In comparison, the $t_{\text{deact-0.5}}$ of AtTPC1 triple mutant (E457N/E605A/D606N) increased to 13-50 ms in the same voltage range, but

still was not significantly different from AtTPC1-WT (Fig. 3.16c, d). Therefore, the impact of these mutations on the deactivation was not so pounced. Taken together, these AtTPC1 double and triple mutant are significantly different to AtTPC1-WT and more VfTPC1-like with respect to the activation kinetics, even though these mutants do not mimic the deactivation of VfTPC1.

When the two mutants faced 10 mM rather than 0 luminal Ca^{2+} , the current densities of all TPC1 variants decreased but to different extents. The highest decline was observed with AtTPC1-WT, whereas the decrease of the AtTPC1 double and triple mutants was minor as with VfTPC1-WT (Fig. 3.17). To further check the susceptibility of these two AtTPC1 mutants to luminal Ca^{2+} inhibition, the luminal Ca^{2+} concentration was further raised up to 50 mM. As a result, the current amplitude level of the AtTPC1 double mutant (E605A/D606N) and triple mutant (E457N/E605A/D606N) still had a similar strong TPC1 channel activity even at this extreme luminal Ca^{2+} level, which resembled that of VfTPC1-WT (Fig. 3.17). However, under such high luminal Ca^{2+} concentration, almost no TPC1 currents were observed with AtTPC1-WT channel (Fig. 3.17). These results suggested that AtTPC1 double and triple mutant probably has a similar tolerance to high luminal Ca^{2+} as the VfTPC1-WT channel.

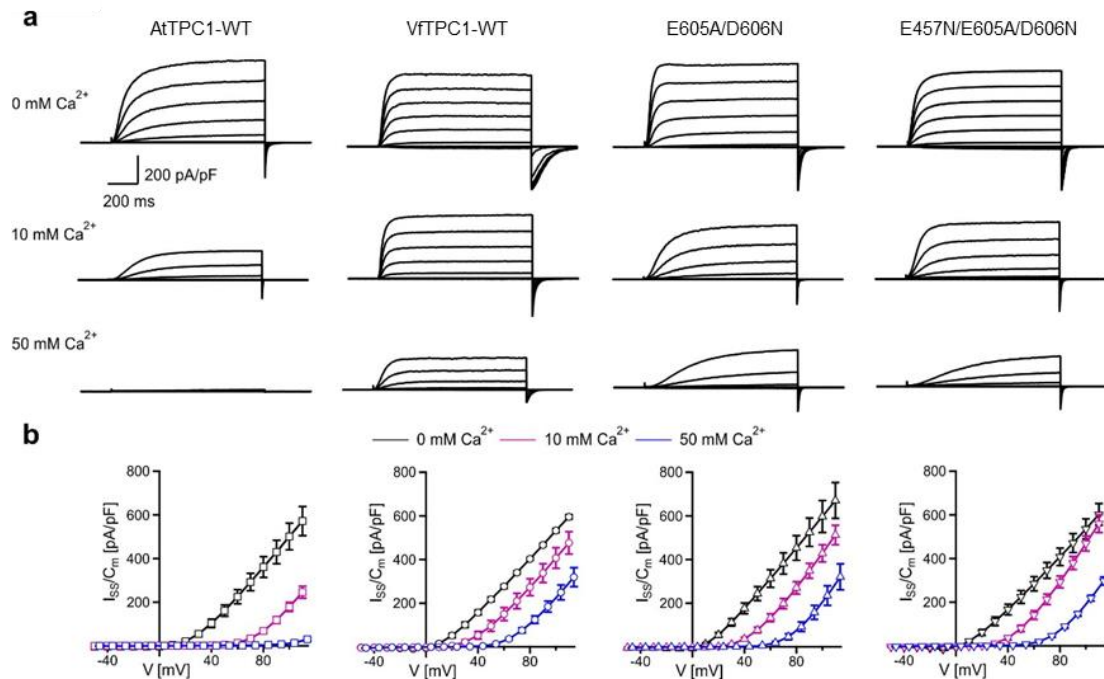


Fig. 3. 17. Effect of luminal calcium on current response of TPC1 channel variants.

(a) Macroscopic current responses of individual vacuoles to different voltage pulses applied in the range of -80 to +110 mV in the presence (10 mM, 50 mM) and absence of luminal Ca²⁺. (b) Normalized TPC1 currents density ($I_{ss}/C_m(V)$) for different TPC1 channel variants were plotted against the clamped membrane voltage under different luminal Ca²⁺ conditions. Enlarged section of the current-voltage curves ($I_{ss}/C_m(V)$) for TPC1 channel variants shown in (a) at 0 mM luminal Ca²⁺. The data of AtTPC1-WT and VfTPC1-WT showed here same as section 3.2.1. The data of AtTPC1-E605A/D606N and AtTPC1-E457N/E605A/D606N at 0 mM Ca²⁺ is the same as in Fig. 3.14-3.15. AtTPC1-E605A/D606N $n_{10Ca} = 5$, $n_{50Ca} = 4$; AtTPC1-E457N/E605A/D606N $n_{10Ca} = 5$, $n_{50Ca} = 4$. All data points are means \pm SEM.

To further quantify the luminal Ca²⁺ tolerance of these two AtTPC1 mutants, the conductance-voltage curves $G/G_{max}(V)$ as well as the midpoint activation voltages $V_{1/2}$ were determined (Fig. 3.18a, b, c). Compared to 0 mM Ca²⁺, the midpoint activation voltages $V_{1/2}$ of the AtTPC1 double and triple mutants were elevated under high luminal Ca²⁺ (10 mM or 50 mM) compared to luminal Ca-free conditions (Fig. 3.18 b, c). However, the rise in the midpoint activation voltages $V_{1/2}$ observed for the AtTPC1 double and triple mutants were significantly smaller than for AtTPC1-WT (Fig. 3.18d, e). As the bar diagrams in Figure 3.18d illustrates, the V_1 values of AtTPC1 double and triple mutant were increased by 75.5 ± 9.5 mV and 71.2 ± 4.6 mV, respectively, and thus comparable to that of VfTPC1 with 60.7 ± 7.1 mV. In addition, the Ca²⁺-induced shift in the V_2

value of the AtTPC1 double mutant was 28.5 ± 4.4 mV which was quite similar to the V_2 value of VfTPC1 (25.9 ± 4.3 mV). The V_2 value for the AtTPC1 triple mutant was with 35.6 ± 2.8 mV slightly higher than that of the AtTPC1 double mutant (Fig. 3.18 e). These results indicated that (i) the AtTPC1 double and triple mutants tend to mimic the luminal Ca^{2+} sensitivity of VfTPC1 rather than AtTPC1, and (ii) the additional D457N replacement in the AtTPC1 triple mutant did not further promote the luminal Ca^{2+} insensitivity compared to the AtTPC1 double mutant. Moreover, at 50 mM Ca^{2+} , the corresponding shifts in the $V_{1/2}$ values of the AtTPC1 double (E605A/D606N) and triple mutants (E457N/E605A/D606N) were similar to those of VfTPC1 (Fig. 3.18b, c, d, e). These results demonstrated that AtTPC1 double and triple mutant exhibit high luminal Ca^{2+} tolerance even at extreme high luminal Ca^{2+} level, as does VfTPC1.

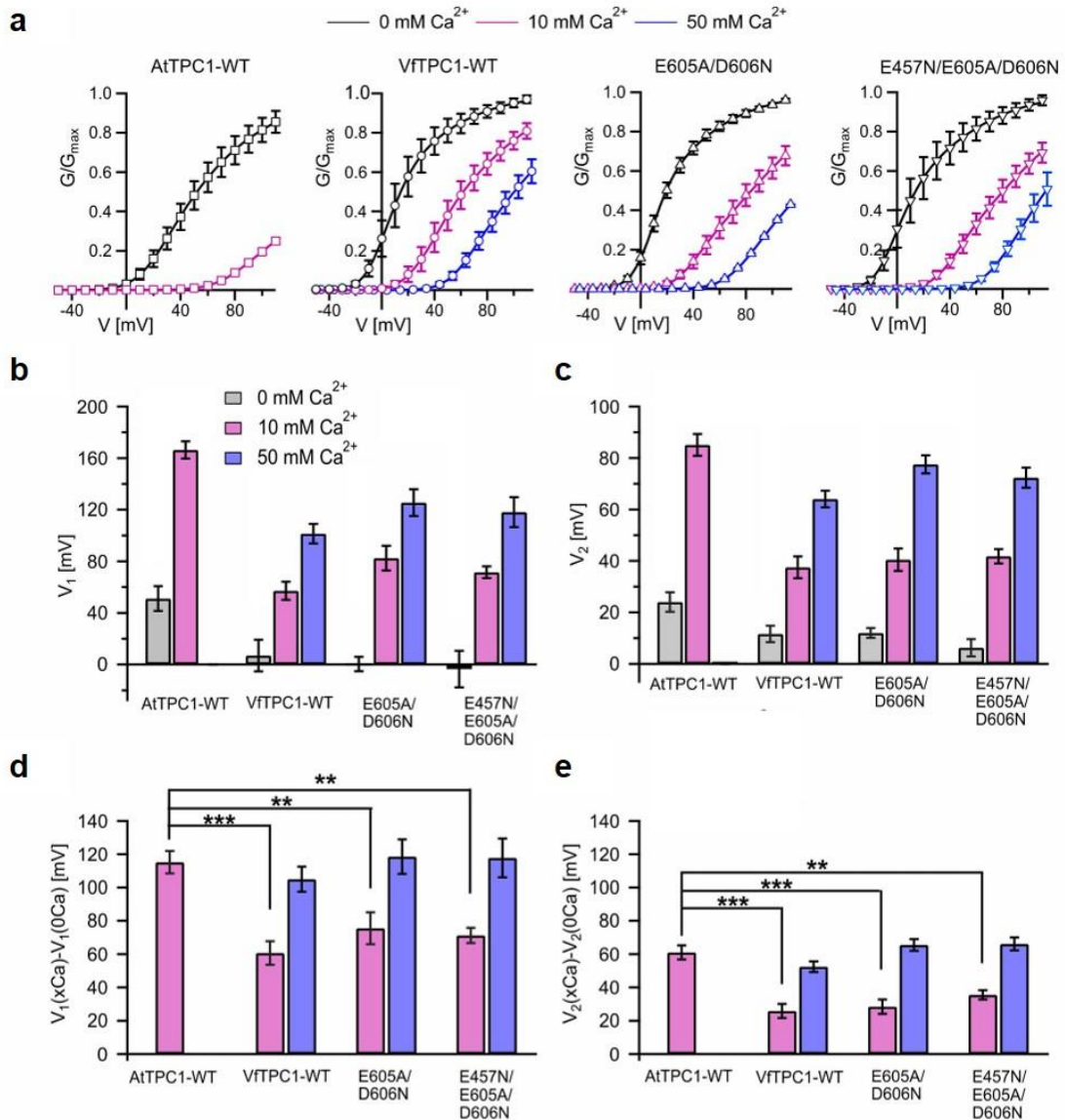


Fig. 3. 18. The voltage-dependent channel activity of TPC1 channel variants in response to different luminal Ca²⁺.

(a) Normalized conductance-voltage curves (G/G_{max} (V)) determined for the different TPC1 channel variants. **(b, c)** The midpoint voltages $V_{1/2}$ are given for the different channel variants at the indicated Ca²⁺ condition. **(d, e)** The differences in the midpoint voltages $V_{1/2}$ shown in (b, c) between 0 and 10 or 50 luminal Ca²⁺ are shown. The changes in $V_{1/2}$ values related to a rise from 0 to 10 Ca²⁺ in different AtTPC1 channel variants compared to AtTPC1-WT were statistically analyzed with one-way ANOVA together with a Dunnett's post hoc comparison test (** $p < 0.01$; *** $p < 0.001$). The data of AtTPC1-WT and VfTPC1-WT showed here are same as section 3.2.1. The data of AtTPC1-E605A/D606N and AtTPC1-E457N/E605A/D606N at 0 mM Ca²⁺ is the same as in Fig. 3.14-3.15. The number of experiments of AtTPC1-E605A/D606N and AtTPC1-E457N/E605A/D606N at 10 mM and 50 mM Ca²⁺ are identical with Fig. 3.17. All data points are the means \pm SEM.

3.2.2.2. The excitability of vacuoles of AtTPC1 triple mutant E457N/E605A/D606N

The hyperactivity of the VfTPC1 channel mutant caused a hyperexcitability of the vacuole (section 3.2.2.4). Since the characteristics of the AtTPC1 triple mutant were VfTPC1-like (section 3.3.1), the effect of the AtTPC1 triple mutant on vacuole excitability was examined. For this, current clamp experiments in the whole-vacuole configuration (Jašlan *et al.*, 2019) were performed as previously for VfTPC1-WT (section 3.3.1). As illustrated in Figure 3.19a, b, the voltage stimulus peak ($V_{\text{stimulus peak}}$) and the voltage stimulus-plateau ($V_{\text{stimulus plateau}}$) of the AtTPC1 triple mutant decreased almost to the level of VfTPC1 compared to AtTPC1-WT; especially the voltage stimulus-plateau of AtTPC1 triple mutant was close to VfTPC1-WT. In addition, the most obvious effect of the AtTPC1 triple mutant on the vacuole membrane was the lifetime of the depolarized post-stimulus plateau (t_{plateau}) (Fig. 3.19c, Table 3.1). The AtTPC1 triple mutant strongly prolonged the lifetime at all current injections compared to AtTPC1-WT. At lowest current injection like 10 or 30 pA, the t_{plateau} of AtTPC1 triple mutant was already significantly longer than AtTPC1-WT. With further increase in the injected current stimulus, the t_{plateau} approached closer and closer to the VfTPC1-WT. For instance, when the injected currents were higher than 70 pA, most of AtTPC1-triple mutant vacuoles sustained post-stimulus depolarization over the entire recording period (10 s) (Fig. 3.19c, Table 3.1). These results suggested that the electrical excitability of the vacuole membrane harboring the AtTPC1-triple channel mutant was close to that of VfTPC1-WT vacuoles which were hyperexcitable.

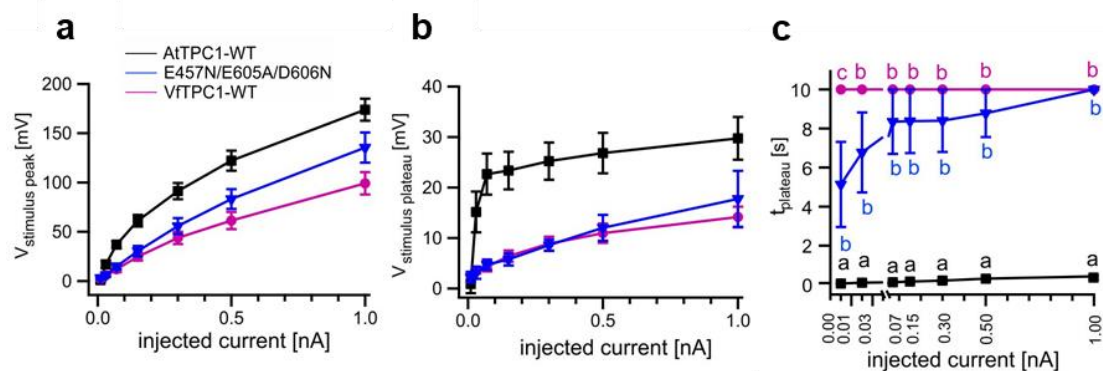


Fig. 3. 19. Dependency of vacuole excitability on TPC1 channel variants.

(a, b) Voltage amplitudes of stimulus peak ($V_{\text{stimulus peak}}$, a) and stimulus plateau ($V_{\text{stimulus plateau}}$, b) for TPC1 channel variants against the corresponding injected current pulse. (c) Lifetime of the post-stimulus depolarization phase (t_{plateau}) plotted against the corresponding injected current pulse for different TPC1 channel variants. Numbers of experiments for each channel type was $n = 6$. All data points are means \pm SEM. The data for AtTPC1-WT and VfTPC1-WT are identical to those shown in Fig 3.13.

Table 3. 1. The lifetime of the post-stimulus plateau phase (t_{plateau}) of TPC1 channel variants from all independent experiments.

Injected current (pA)	VfTPC1-WT t_{plateau} (s)		AtTPC1-triple mutant E457/E605A/D606N t_{plateau} (s)					mean \pm SEM (n = 6)
	Exp. 1-6	mean \pm SE M (n = 6)	Exp. 1-3	Exp. 4	Exp. 5	Exp. 6		
10	10.00	10.00\pm0	10.00	0.28	0.48	0.04	5.13\pm2.18	
30	10.00	10.00\pm0	10.00	10.00	0.59	0.04	6.77\pm2.04	
70	10.00	10.00\pm0	10.00	10.00	10.00	0.09	8.35\pm1.65	
150	10.00	10.00\pm0	10.00	10.00	10.00	0.23	8.37\pm1.63	
300	10.00	10.00\pm0	10.00	10.00	10.00	0.40	8.40\pm1.60	
500	10.00	10.00\pm0	10.00	10.00	10.00	2.70	8.78\pm1.22	
1000	10.00	10.00\pm0	10.00	10.00	10.00	10.00	10.00\pm0.00	
Injected current (pA)	AtTPC1 wild type t_{plateau} (s)							mean \pm SEM (n = 6)
	Exp. 1	Exp. 2	Exp. 3	Exp. 4	Exp. 5	Exp. 6		
10	0.05	0.05	0.06	0.02	0.12	0.05	0.06\pm0.13	
30	0.08	0.06	0.12	0.04	0.25	0.09	0.11\pm0.03	
70	0.10	0.07	0.15	0.05	0.26	0.12	0.13\pm0.03	
150	0.14	0.08	0.22	0.05	0.28	0.21	0.16\pm0.04	
300	0.19	0.08	0.31	0.06	0.36	0.28	0.21\pm0.05	
500	0.38	0.08	0.40	0.06	0.48	0.45	0.31\pm0.08	
1000	0.55	0.09	0.53	0.09	0.62	0.68	0.42\pm0.11	

3.2.3. The function of the VfTPC1 triple mutant N458E/A607E/N608D

In the previous chapter, the AtTPC1 triple mutant (E457N/E605A/D606N) was studied, in which the three polymorphic sites (E457/E605/D606) in the Arabidopsis TPC1 were replaced by the homologous neutral amino acids alanine or asparagine of VfTPC1. As a result, the AtTPC1 gating behavior was altered and mimicked that of VfTPC1-WT, such as reduced sensitivity towards luminal calcium and a voltage activation threshold shifted to more negative potentials (section 3.2.2), which. Therefore, it was interesting to test if in the opposite direction the substitution of the three polymorphic sites (N458, A607, N608) in VfTPC1 to negatively charged amino acids such as glutamic acid or aspartic acid found at homologous sites in the AtTPC1-WT channel, leads to the AtTPC1-like voltage dependency and luminal calcium insensitivity. For this, the VfTPC1 triple mutant N458E/A607E/N608D channel was generated as C-terminal fusion construct with eYFP and again transiently expressed in the background of the TPC1-loss-of-function mutant *attpc1-2*. Like the VfTPC1-WT channel and the AtTPC1 channel mutants, the VfTPC1 triple mutant was targeted to the vacuole membrane (Fig. 3.20a). In subsequent patch-clamp experiments, the function of the VfTPC1 triple mutant was approved (Fig. 3.20b). During macroscopic current recordings at 0 mM vacuolar calcium, depolarizing voltage pulses to VfTPC1-triple vacuoles resulted in similar current responses as with VfTPC1-WT vacuoles (Fig. 3.20b). After analyzing the voltage current curve ($I_{ss}/C_m(V)$), the current densities of VfTPC1-triple mutant were analogous to those of VfTPC1-WT (Fig. 3.20c). Inward currents directed into the cytosol at negative voltages were also preserved in VfTPC1-triple mutant channels, and the voltage activation threshold of these mutant inward currents appeared to be slightly shifted to more negative membrane potentials compared to VfTPC1-WT (Fig. 3.20d). To clearly define the voltage dependency of the VfTPC1-triple mutant under 0 mM luminal Ca^{2+} condition, the

conductance-voltage curves ($G/G_{\max}(V)$) and the midpoint activation voltages V_1 and V_2 were determined (Fig. 3.20e, f). As the bar diagram in Figure 3.20f demonstrates, the V_1 and V_2 values of the VtTPC1-triple mutant were 4.2 ± 10.6 mV and 8.3 ± 4.7 mV, respectively, which was still close to those of VtTPC1-WT ($V_1 = -3.5 \pm 12.3$ mV, $V_2 = 11.6 \pm 3.2$ mV). Thus, replacement of the three polymorphic sites (N458, A607, N608) in VtTPC1 channel did not dramatically change the voltage dependency of the fabacean channel.

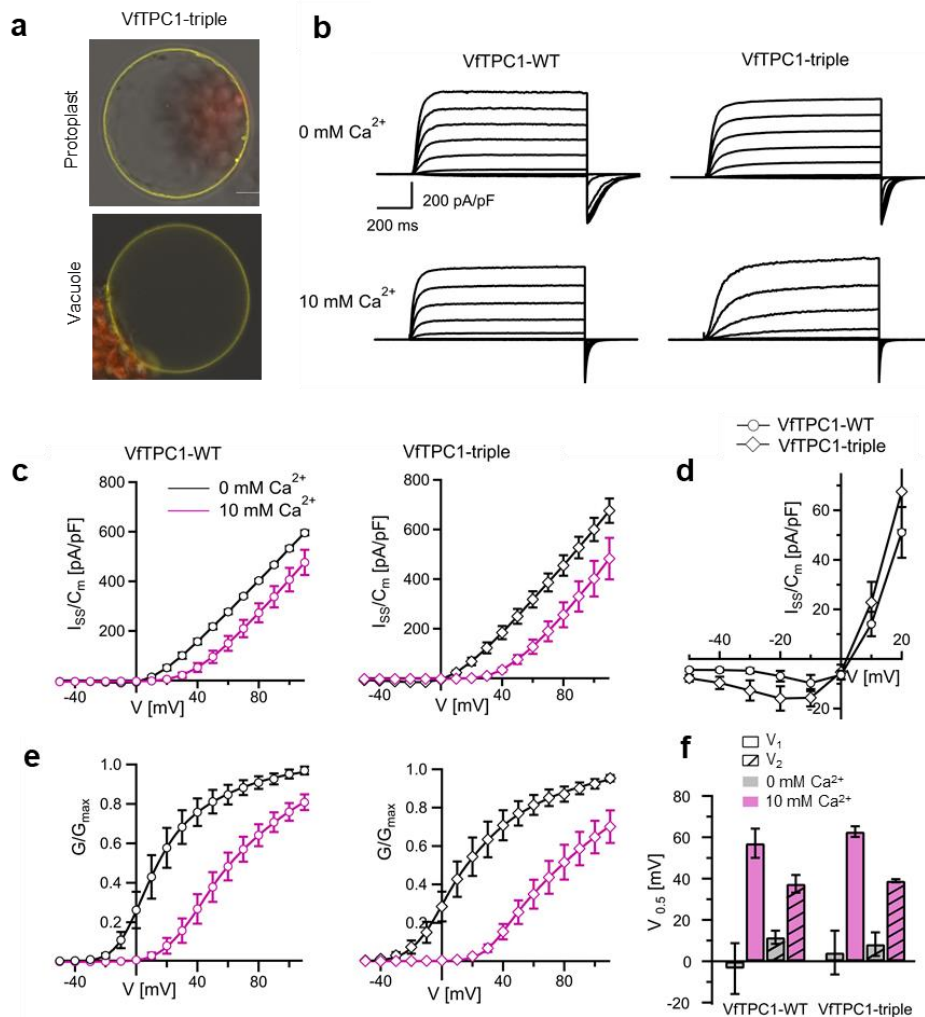


Fig. 3. 20. The voltage-dependent channel activity of VtTPC1 triple mutant (N458E/A607E/N608D).

(a) Mesophyll protoplasts and released vacuoles from the *attpc1-2* after transient transformation with eYFP-tagged VtTPC1-triple channel construct. Bright field and fluorescent images were merged. Red fluorescence corresponds to chloroplast autofluorescence. The yellow fluorescence represents the eYFP fluorescence, Scale bars = 10 μ m. (b) Macroscopic TPC1 current recordings from *tpc1-2* mesophyll vacuoles transformed with indicated VtTPC1 channel variants. (c) Normalized steady-state currents ($I_{ss}/C_m(V)$) plotted against the clamped membrane voltages in the presence (10 mM) and absence of luminal Ca^{2+} . (d) Enlarged section

of the current-voltage curves ($I_{ss}/C_m(V)$) for TPC1 channel variants shown in (d) at 0 mM luminal Ca^{2+} . (e) Normalized conductance-voltage curves ($G/G_{max}(V)$) of TPC1 channel variants in the presence and absence of luminal Ca^{2+} . (f) Midpoint activation voltages $V_{1/2}$ are given for the different channel variants at the indicated Ca^{2+} condition. For VfTPC1 triple $n_{0 Ca} = 8$ and $n_{10 Ca} = 5$. The data for VfTPC1-WT are identical to those shown in section 3.2.1. All data points are means \pm SEM. VfTPC1 triple mutant means N458E/A607E/N608D.

In addition, the luminal calcium insensitivity of VfTPC1 triple mutant was also examined under high vacuolar calcium conditions. For this, the TPC1 current traces of the VfTPC1 triple mutant was recorded at 10 mM vacuolar calcium and compared with those of VfTPC1-WT channel (Fig. 3.20b, c). Similar with VfTPC1-WT, TPC1 outward currents were still largely elicited upon depolarization with the VfTPC1 triple mutant in the presence of 10 mM luminal calcium (Fig. 3.20b, c). The conductance-voltage curve ($G/G_{max}(V)$) and the midpoint activation voltages V_1 and V_2 of the VfTPC1 triple mutant and VfTPC1-WT were also similar (Fig. 3.20e, f). The midpoint activation voltages V_1 and V_2 of the VfTPC1 triple mutant were 62.74 ± 2.6 mV and 38.9 ± 0.8 mV, respectively, which were comparable to the V_1 (57.1 ± 7.1 mV) and V_2 (37.5 ± 4.3 mV) values of the VfTPC1-WT channel (Fig. 3.20f). Taken together, the introduction of the three charged residues glutamate and aspartate from AtTPC1 into the homologous polymorphic sites 458, 607 and 608 of VfTPC1 did not convert the characteristic VfTPC1-WT features like hyperactivity and vacuolar calcium insensitivity of the VfTPC1 channel to those of AtTPC1-WT.

3.2.4. Effect of pore-mouth amino acids on AtTPC1 channel conductance

The TPC1 channel in *Vicia faba* exhibits a huge single channel conductance of 280 pS which is around 3 times higher than that of *Arabidopsis thaliana* (80 pS) (Beyhl *et al.*, 2009; Schulz-Lessdorf and Hedrich, 1995). According to the crystal structure of the AtTPC1 channel (Kintzer and Stroud, 2016), the amino acids Glu605 and Asp606 are localized near the entrance of the pore region of

the AtTPC1 channel. As outlined in previous chapters (section 3.2.2), the VtTPC1 channel harbors instead neutral residues at homologous sites (Ala607, Asn608). Therefore, it was important to investigate whether these two polymorphic amino acids near the pore mouth potentially determine the TPC1 single channel conductance. For this, the single channel fluctuations of the AtTPC1 double mutant E605A/D606N were recorded in excised membrane patches from vacuoles of transiently transformed protoplasts of *attpc1-2* plants. Transiently expressed AtTPC1-WT and VtTPC1-WT channels served as controls.

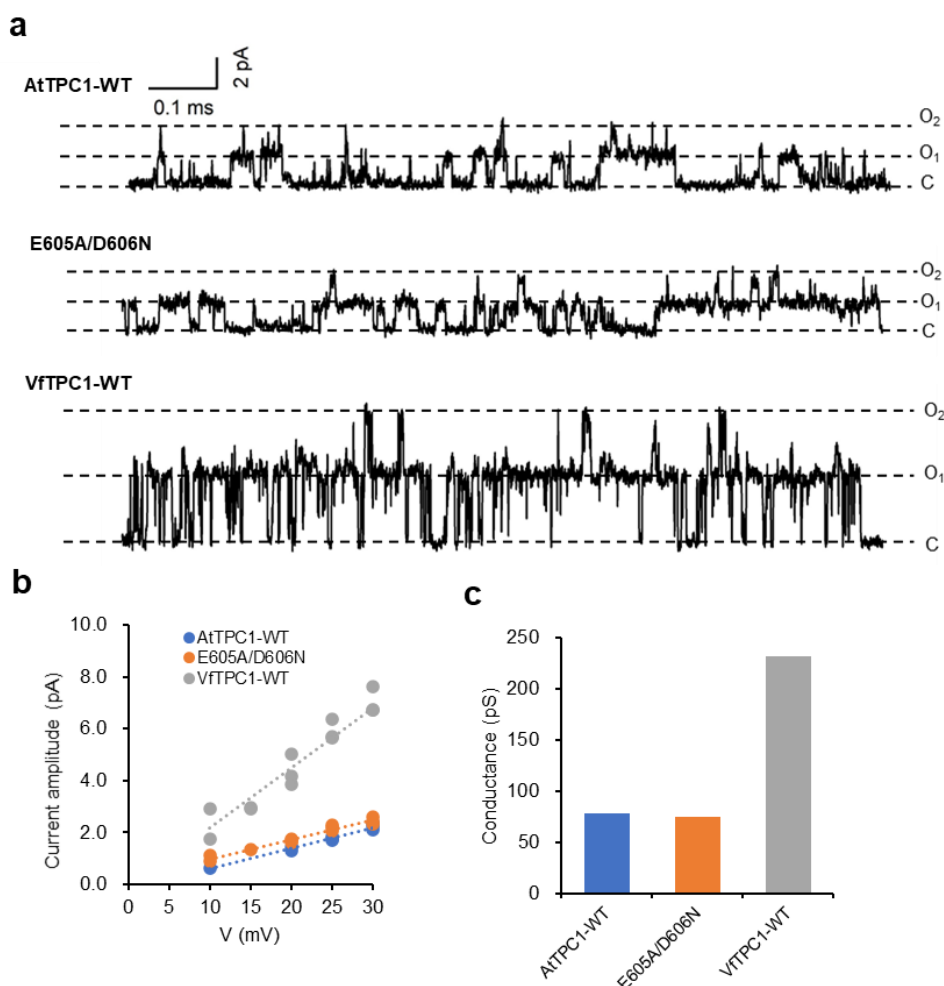


Fig. 3. 21. Single channel analysis of TPC1 channel variants.

(a) Single channel currents of indicated TPC1 channel variants evoked at +25 mV. **(b)** Single channel current amplitudes plotted against the respective voltage pulses for indicated TPC1 channel variants. Symbols for each plant line comprises 3 individual experiments. Lines reflect global regression fit for each plant line. **(c)** Bar diagram gives the calculated unitary conductance of different TPC1 channel variants from the global fit.

Under symmetrical K^+ conditions (100 mM) in the absence of vacuolar Ca^{2+} , the single-channel current amplitudes were determined from the single channel fluctuations recorded at different membrane voltages. After plotting the individual single-channel current amplitudes against respective voltages, the single channel conductance was derived from the slope of the global regression line fit (section 2.3.7). The single-channel conductance was estimated to be 79 pS for the transiently expressed AtTPC1-WT channel and 232 pS for VtTPC1-WT (Fig. 3.21). The study of the AtTPC1 double mutant (E605A/D606N) revealed an AtTPC1-like single channel conductance of about 75 pS (Fig. 3.21), indicating that these pore residues in AtTPC1 (Glu605 and Asp606) did not control the single channel conductance of AtTPC1 channel.

4. Discussion

4.1. Glu605/Asp606 in the pore region of AtTPC1 represents a new luminal Ca²⁺ binding site

The approach of transiently transforming mesophyll protoplast from *Arabidopsis thaliana* TPC1 loss-of-function mutant *attpc1-2* with TPC1 channel mutants and isolating vacuoles from them for subsequent patch-clamp studies of the TPC1 channel features was already applied 10 years ago (Dadacz-Narloch *et al.*, 2011; Jašlan *et al.*, 2016). In the present thesis, the same experimental strategy was again successfully used, this time to elucidate the role of the charged residues Glu605, Asp606 and Asp607 in the luminal pore mouth region of AtTPC1 for channel gating. This was possible because (i) like AtTPC1-WT all C-terminal eGFP-fused AtTPC1 pore-mouth mutants (E605A/Q, D606N, D607N, E605A/D606N, E605Q/D606N/D607N) did not alter their vacuolar localizations in the *attpc1-2* protoplasts (Fig. 3.1) and (ii) the transiently expressed AtTPC1 channel variants led to the recovery of typical slow-activating outward-rectifying TPC1/SV-like cation currents in the *attpc1-2* vacuoles (Fig. 3.2; Dadacz-Narloch *et al.*, 2011; Peiter *et al.*, 2005). Thus, the mutations in the luminal pore entrance neither altered the vacuolar targeting nor destroyed the function of AtTPC1. However, these AtTPC1 pore mutants differed from AtTPC1-WT in two ways: First, in the absence of luminal Ca²⁺, the open channel probability of the single channel mutants E605A, D606N and the double mutant E605A/D606N shifted significantly towards more negative membrane potentials (Fig. 3.4, 3.5). Second, the simultaneous neutralization of two amino acids (E605A/D606N) reduced the susceptibility to the inhibitory luminal gating modulator Ca²⁺ (Fig. 3.2 - Fig. 3.5). These effects were maintained but not enhanced in the triple mutant EDD (E605Q/D606N/D607N) by the additional neutralization at position 607. Thus, these results suggest that the negatively charged cluster formed by Glu605 and Asp606 but not by the

neighboring charged residue Asp607 at the entrance of the pore is involved in channel gating and functions as a novel luminal Ca²⁺ sensor. Actually, these results are consistent with the AtTPC1 crystal structure (Kintzer and Stroud, 2016), showing that Glu605 and Asp606 form an extensive asymmetric constriction site at the luminal pore to coordinate a Ca²⁺ ion. Thus, in this thesis functional experiments addressing these pore residues E605/D606 confirmed that they form a novel Ca²⁺ sensing gate (site 3) within the ion transport pathway. However, how can these pore mouth amino acids (Glu605/Asp606) affect the voltage dependence? In other words, are these pore residues really linked to the voltage sensor or are the effects of the pore mutations on voltage dependence just non-specific changes in channel gating? In addition, how do the mutated residues Glu605, Asp606 reduce the Ca²⁺ sensitivity of the AtTPC1 channel? In the following, these issues will be addressed.

4.1.1. AtTPC1-Glu605/Asp606 motif affects the voltage gating

As mentioned in the introduction (section 1.2.3.2), AtTPC1 channel is voltage-dependent and composed of two Shaker-like domains (DI and DII), each of which contains six transmembrane domains (S1-S6 and S7-S12) with two pore regions between S5 and S6, S11 and S12 (Fig.1.2). Within the structure of AtTPC1, in fact, there are two voltage sensor domains (VSDs) in AtTPC1: S1-S4 was named as VSDI and S7-S10 as VSDII (Guo *et al.*, 2016; Kintzer and Stroud, 2016). Later, studies on VSDs reveals that VSDI contributes less to voltage sensing. In contrast, only S10 in the VSDII functions as the major voltage sensor (Guo *et al.*, 2016; Jašlan *et al.*, 2016; Kintzer *et al.*, 2018; Kintzer and Stroud, 2016). The functional voltage sensor S10 is fulfilled with three functional gating charges (R3: R537; R4: R540; R5: R543; Fig. 4.1). In the resting state, the gating charges R3, R4 and R5 are well aligned and exposed

to the cytoplasmic side with the first gating charge R3 near the charge transfer center. The charge transfer center consists of three amino acids Y475/E478/D500 to interact with the positive gating charges, which facilitates the transfer of positive charges in the process of voltage sensing (Guo *et al.*, 2016; Tao *et al.*, 2010).

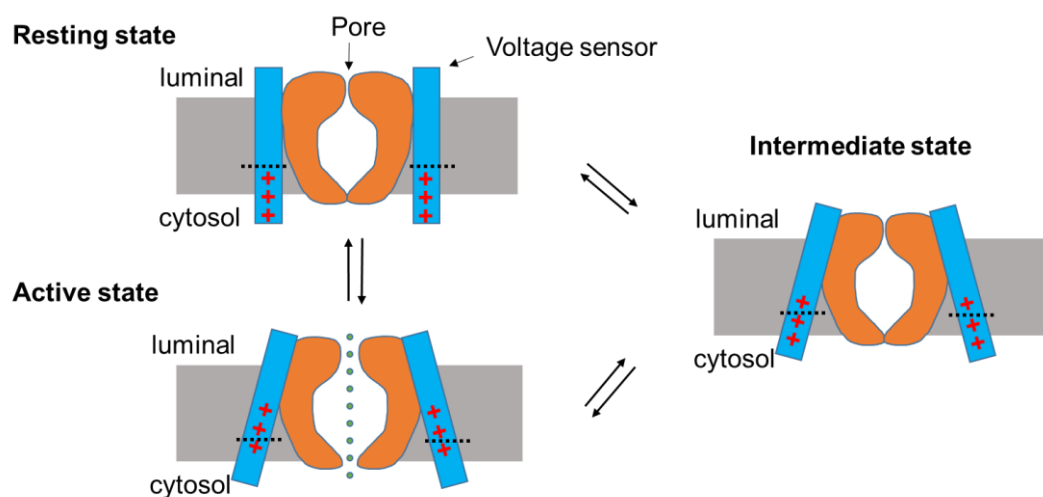


Fig. 4. 1. The working model of the voltage sensor from AtTPC1 channel.

The red crosses '+' from up to down represent three functional positively charged gating charges (R3, R4 and R5) identified in the voltage sensor S10 (Guo *et al.*, 2016; Jašlan *et al.*, 2016). Green dots illustrate the cations. The dotted line '-----' represent the charge transfer center. The resting and active states show the closing and open state of TPC1 channel, respectively. The intermediate state adopted a half-activated conformation when the luminal binding sites D240/D454/E528 or E605/D606 in AtTPC1 channel were abolished. The model was drawn according to (Guo *et al.*, 2016; Kintzer *et al.*, 2018; Kintzer and Stroud, 2018).

Upon activation, the positions of these gating charges are changed with the movement of the first two gating charges (R3, R4) directed towards the vacuolar lumen and the gating charge (R5) to the charge transfer center (Guo *et al.*, 2016; Kintzer *et al.*, 2018; Kintzer and Stroud, 2018). Thus, the effective movement of these gating charges across the membrane barrier finally leads to the conformational alteration of AtTPC1 channel and, therefore, to voltage gating of AtTPC1 channel (Guo *et al.*, 2016; Kintzer *et al.*, 2018). It has been proven that the VSDII conformation can be directly affected by the luminal Ca^{2+} sensor. In 2018, Cryo-EM structures of the AtTPC1-DDE(D240A/D454A/E528A) mutant, in which the luminal Ca^{2+} sensing site 1 was functionally abolished,

were examined (Kintzer *et al.*, 2018). The authors found that in the presence of 0.1 mM Ca^{2+} the AtTPC1-DDE channel resides in an intermediate state (Kintzer *et al.*, 2018), while the AtTPC1-WT channel appeared to be still in the resting closed channel state (Guo *et al.*, 2016; Kintzer *et al.*, 2018; Kintzer and Stroud, 2016). Even if the VSDII of AtTPC1 channel adopted a half-activated conformation in the intermediate state, the conductance pathway was closed (Fig. 4.1). However, with respect to the resting state, in the intermediate state the charge transfer center has moved downward while R3 has moved slightly upward, and the voltage sensor S10 toward the pore. Thus, the gating charge R3 in the voltage sensor S10 has been transferred across the charge transfer center. It means that these gating charges R3, R4 and R5 can more easily cross the membrane barrier in the intermediate state compared to the resting state. Considering also electrophysiological studies with the AtTPC1-DDE (Guo *et al.*, 2017), therefore, such conformational changes in the VSDII of the AtTPC1-DDE mutant support the opening of the AtTPC1 channel and shift the voltage-dependent activation threshold to more negative potentials under low luminal Ca^{2+} . Thus, there is a direct interaction between the vacuolar Ca^{2+} sensor site 1 and voltage sensor in AtTPC1 channel. In the present thesis, it was observed that mutations of the new luminal Ca^{2+} sensing site 3 (Glu605/Asp606) affected the number of equivalent gating charges z_1/z_2 moved during the transition of AtTPC1 channel between the assumed $C_1 \rightleftharpoons C_2$ and $C_1 \rightleftharpoons O$ states (Fig. 3.1.4). Since voltage-dependent channel opening depends on the gating charge movement (see above), an altered number of the equivalent gating charges indicates a change in the function of the voltage sensor (Guo *et al.*, 2016; Jašlan *et al.*, 2016). Thus, in the present context, the novel luminal Ca^{2+} binding site Glu605/Asp606 affected voltage sensing in AtTPC1. Therefore, one can conclude that there is a functional link between the new luminal Ca^{2+} binding site E605/D606 and the voltage sensor domain. Because of the same effects of Ca^{2+} sensing site 1 and 3 on channel gating, one could assume that disruption of the new luminal Ca^{2+} binding site 3 (Glu605/Asp606)

near the luminal pore mouth promotes channel activation at more negative voltages possibly also by establishing an intermediate channel state (Fig. 4.1; Guo *et al.*, 2016; Kintzer and Stroud, 2016).

In addition, the Glu605/Asp606 motif in the pore region was recently reported to regulate the ion flow through the conduction pathway (Navarro-Retamal *et al.*, 2021). As the AtTPC1 crystal structure revealed, Glu605 and Asp606 forms a construction site within the cation conduction pathway (Kintzer and Stroud, 2016). Molecular dynamic simulations revealed that these pore residues (Glu605, Asp606) seem to control the direction of ion flow between cytosol and lumen by reorienting its configuration (Navarro-Retamal *et al.*, 2021). During influx simulations, this motif compacted towards the channel pore and impedes the flow of K⁺ ions from the lumen toward the selectivity filter. In contrast, during efflux simulations this motif detaches from the channel pore, thereby facilitating the flow of K⁺ through the channel from the cytosol to the lumen. These observations suggested that the movement of the pore residues Glu605/Asp606 regulate the opening and closing of TPC1 channel. The neutralized motif E605/D606 would impair such regulation and reduce the electrostatic interactions between the E605/D606-motif and the permeating ions. Therefore, the TPC1 channel opened with less activation energy when the pore residues were neutralized (E605A/D606N). In conclusion, the new luminal Ca²⁺ binding site 3 formed by the charged residues Glu605/Asp606 near the pore mouth regulate the gating of TPC1 channel by cooperating with the voltage sensor and stabilizing the conductance pathway.

4.1.2. The pore motif Glu605/Asp606 contributes to the low tolerance of AtTPC1 to high luminal Ca²⁺

Due to its complex structure, the voltage activation threshold of SV/TPC1 channel is under control of many factors including luminal Ca²⁺ (Hedrich and

Marten, 2011; Hedrich *et al.*, 2018). In the past and in the present thesis (section 3.1; Dadacz-Narloch *et al.*, 2011; Guo *et al.*, 2016; Pottosin *et al.*, 2004; Pottosin *et al.*, 1997), it has been shown that high luminal Ca^{2+} shifts the TPC1 activation to more positive voltages by binding to luminal Ca^{2+} sensing sites. This observation prompted the researchers to investigate how the voltage sensing domains (VSDs) change their conformations, when the luminal Ca^{2+} binding site is occupied by the Ca^{2+} ion. After the crystal structure of AtTPC1 was revealed (Guo *et al.*, 2016), it was found that luminal Ca^{2+} can stabilize VSDII (S7-S10) in the resting state by holding the functional voltage sensor domain S10 together with the S7 and S5 of the neighboring subunit. This conformation prevents the movement of the functional voltage sensor S10 in response to voltage changes. This observation showed that if the luminal Ca^{2+} binding sites of AtTPC1 channel are damaged, the VSDII will be out of the inhibitory control of the luminal Ca^{2+} binding sites and AtTPC1 channel will obtain high tolerance to luminal Ca^{2+} (Guo *et al.*, 2016). This was also proven by electrophysiological studies. When the luminal binding site (Asp240, Asp454 and Glu528) was damaged by the mutation D454N (*fou2*), AtTPC1 channel lost its sensitivity toward luminal calcium and exhibits promoted voltage-dependent channel opening due to the voltage activation threshold shifted to more negative potentials (Dadacz-Narloch *et al.*, 2011). Similar observations have been obtained for other mutated amino acids (Asp240, Glu528, Glu239, Glu457), which contribute to vacuolar calcium sensing (Dadacz-Narloch *et al.*, 2011; Guo *et al.*, 2016; Jaślan *et al.*, 2016). In the present thesis, the negative amino acids near the pore mouth Glu605/Asp606 can coordinate luminal Ca^{2+} ion and function as a new luminal Ca^{2+} binding site. When this new Ca^{2+} binding site was mutated, the voltage activation threshold of AtTPC1 shifted to more negative potentials even in the absence of luminal Ca^{2+} and AtTPC1 channel became also more tolerant to luminal Ca^{2+} . This is similar with that of *fou2* mutant (Dadacz-Narloch *et al.*, 2011). As already discussed above in section 4.1.1, the Glu605/Asp606 motif near the pore mouth is functionally linked to the

voltage sensor. Therefore, one can conclude that when luminal Ca^{2+} occupies the new luminal Ca^{2+} binding site 3 (Glu605/Asp606), the movement of voltage sensor S10 is probably also fixed just as suggested when luminal Ca^{2+} binds to the other luminal Ca^{2+} sensing site.

4.2. The hyperactivity of the native *Vicia faba* TPC1 channel is partly related to the loss of luminal Ca^{2+} sensor Glu605/Asp606

Considering the pore charges Glu605/Asp606 as the third new luminal Ca^{2+} sensing site in AtTPC1 (section 3.1), a total of three luminal Ca^{2+} sensor sites have been identified so far in the AtTPC1 channel (Dadacz-Narloch *et al.*, 2011; Guo *et al.*, 2016; Kintzer and Stroud, 2016). Interestingly, Glu457 from site 2 and Glu605/Asp606 from site 3 are not conserved at homologous sites in Fabaceae TPC1 channels; for example, in *Vicia faba* TPC1 Glu605/Asp606 are neutralized by the exchange to either alanine (Ala607) or asparagine (Asn608) (Fig. 3.7). Furthermore, glutamic acid (Glu457) in AtTPC1 was replaced by the neutral amino acid asparagine at homologous site in *Vicia faba* (Asn458). Interestingly, TPC1 channel from *Vicia faba* is hyperactive, with the negatively shifted voltage dependency and reduced susceptibility to blocking luminal Ca^{2+} (Fig. 3.9-3.12). Therefore, VfTPC1 confers hyperexcitability to the vacuole (Fig. 3.13), as did the artificial *fou2* channel (Jaślan *et al.*, 2019). When AtTPC1 was mutated by the two or three polymorphic residues present in VfTPC1 at homologous sites (Asn458, Ala607, Asn608), both AtTPC1 double mutant (E605A/D606N) and triple mutation (E457N/E605A/D607N) gained similar VfTPC1-like voltage dependence and luminal Ca^{2+} insensitivity. In comparison, it has been reported that the mutation E457N promoted the closing state of AtTPC1 channel, because although E457N led to a loss of sensitivity of the AtTPC1 channel to luminal divalent cations while the voltage dependence,

however, shifted to more positive potentials (Dadacz-Narloch *et al.*, 2011). Thus, in other words, the third luminal Ca²⁺ sensing site (Glu605/Asp606) is dominant and can override the opposite effect of E457N on voltage dependence. However, in the other way around, mutating the three polymorphic site residues (N458E/A607E/N608D) in VfTPC1 with the negative charged amino acids in AtTPC1 failed to convert the gating behavior of VfTPC1 to that of AtTPC1 (Fig. 3.20). VfTPC1 triple mutant (N458E/A607E/N608D) and VfTPC1-WT had a similar voltage dependence and luminal Ca²⁺ insensitivity (Fig. 3.20). Such lack of success is often observed when mutations are introduced to re-gain a function as in the present case with VfTPC1. This effect may be linked to additional structural adaptations which probably have evolved in the Fabaceae channel and have fixed the gating characteristics of VfTPC1. Therefore, there should exist other different functional determinants between *Arabidopsis thaliana* and *Vicia faba* except for the polymorphic site residues in the luminal Ca²⁺ sensing site 3, which stabilize the VfTPC1 hyperactivity and could be possibly revealed in the future by the crystal structure of VfTPC1.

4.3. Amino acids Glu605/Asp606 are not involved in determining the TPC1 channel conductivity

Till now, TPC1 channel has been studied from many different plant species for long time. Among those studies, it has been observed that different species have different TPC1 unitary conductance (Tale 4.1; Beyhl *et al.*, 2009; Hedrich and Marten, 2011; Schulz-Lessdorf and Hedrich, 1995). The difference of unitary conductance between AtTPC1 and VfTPC1 channels was also observed in the present thesis (Fig. 3.21). The unitary conductance of AtTPC1-WT transiently expressed in mesophyll protoplasts of *attpc1-2* mutant plants was 79 pS under symmetrical 150 mM K condition, as observed for TPC1 channels in *Arabidopsis thaliana* wild type plants under same solute condition

(Beyhl *et al.*, 2009). This also indicate that the transient expression of the TPC1 channel in the *attpc1-2* background did not affect the TPC1 ion transport capacity. In contrast, the unitary conductance of transiently expressed VfTPC1-WT channel was 232 pS, which was thus 3-fold higher than that of AtTPC1 (section 3.2.4).

Table 4. 1. The unitary conductance of different TPC1 channel variants.

Specie/ channel variant	Tissue	KCl [mM] cytosol/ lumen	pH cytosol/ lumen	γ (pS)	reference
<i>A. thaliana</i> WT AtTPC1-WT	mesophyll	100/100	7.5/5.5	80	Beyhl <i>et al.</i> , 2009
<i>A. thaliana</i> WT AtTPC1-WT	mesophyll	100/100	7.5/7.5	40	Beyhl <i>et al.</i> , 2009
<i>Vicia faba</i> VfTPC1-WT	guard cell	200/200	7.5/7.5	280	Schulz-Lessdorf and Hedrich, 1995
<i>Vicia faba</i> VfTPC1-WT	guard cell	100/100	7.5/7.5	150	Schulz-Lessdorf and Hedrich, 1995
<i>A. thaliana</i> <i>attpc1-2</i> VfTPC1-WT	mesophyll	100/100	7.5/5.5	232	In this thesis
<i>A. thaliana</i> <i>attpc1-2</i> AtTPC1-WT	mesophyll	100/100	7.5/5.5	75	In this thesis
<i>A. thaliana</i> <i>attpc1-2</i> AtTPC1- E605A/D606N	mesophyll	100/100	7.5/5.5	78	In this thesis
<i>A. thaliana</i> <i>attpc1-2</i> AtTPC1-D454N	mesophyll	100/100	7.5/5.5	82	Lenglet <i>et al.</i> , 2017
<i>A. thaliana</i> <i>attpc1-2</i> AtTPC1- D454N/A669V	mesophyll	100/100	7.5/5.5	43	Lenglet <i>et al.</i> , 2017
<i>A. thaliana</i> <i>attpc1-2</i> AtTPC1- D454N/M629I	mesophyll	100/100	7.5/5.5	40	Lenglet <i>et al.</i> , 2017

In the present work, the unitary conductance of VfTPC1-WT was slightly larger

than in the previous 1995 report where the unitary conductance of TPC1 from *Vicia faba* was determined to be 150 pS (Schulz-Lessdorf and Hedrich, 1995). This difference in the VfTPC1 unitary conductance is likely related to the different experimental conditions. In this thesis the single channel fluctuations were recorded under a pH gradient directed into the vacuole ($\text{pH}_{\text{cytosol}} 7.5/\text{pH}_{\text{lumen}} 5.5$) and not under symmetrical pH 7.5 conditions. As previously reported for AtTPC1-WT by Beyhl *et al.* (2009), such a pH gradient strongly promotes the unitary conductance (Table 4.1). However, considering the different unitary conductance of VfTPC1 and AtTPC1 under identical solute conditions, this raises the question of the underlying mechanism. One possible reason could be different residues within or near the pore of these TPC1 channel variants. For instance, in the AtTPC1 channel, the residues Met629 (in pore domain II) and Ala669 (pore-forming of S12) has been reported to affect the unitary conductance of AtTPC1 (Lenglet *et al.*, 2017). The unitary conductance of both AtTPC1 mutants M629I/D454N, A669V/D454N decreased from 80 pS to about 40 pS compared with AtTPC1 mutant D454N (Lenglet *et al.*, 2017). As shown in the present thesis (section 3.2.4), the double mutation of the luminal pore residues (E605A/D606N), however, did not affect the ion transport capacity of AtTPC1, indicating that at least these two amino acids (E605/D606) near the pore mouth, forming a negatively charged ring of four residues in total, do not determine the unitary conductance of the Arabidopsis TPC1 channel (Fig. 3.21, Table 4.1). In comparison, the large conductance of the BK channel (200-400 pS), is at least partially related to a negatively charged ring of a total of eight glutamate residues localized at the cytoplasmic entrance to the ion transport pathway. Neutralization of these eight glutamates caused a 50% reduction in the outward single-channel currents (Brelidze *et al.*, 2003; Nimigean *et al.*, 2003). However, a negatively charged ring formed by E605/D606 in the luminal entrance of the pore of AtTPC1 are missing in VfTPC1. Moreover, this negative charged ring in AtTPC1 does not affect conductance. Therefore, it is meaningful to know whether a negative charged ring exist at the

cytoplasmic entrance of VfTPC1. In the future, with investigating of the crystal or CryoEM structure of VfTPC1, this could be defined. Which other structural reasons could contribute to the high conductance of TPC1 in *Vicia faba*? Again, one could look at other known determinants of BK channel's unitary conductance. It has been revealed that the internal entrance (cytoplasmic entrance) of the pore is much wider in BK channels than Kv channels (Jiang *et al.*, 2002; Zhou *et al.*, 2011). The single channel conductance of Kv channel is much smaller, around 20 pS (Naranjo *et al.*, 2016). Together with electrostatic calculation, it was concluded that the large cytoplasmic cavity of the BK channel is important for the huge channel conductance (Jiang *et al.*, 2002; Latorre *et al.*, 2017; Zhou *et al.*, 2011). Therefore, in the future, it might be interesting to investigate whether the VfTPC1 and AtTPC1 channel may differ in their cytoplasmic cavity.

4.4. High impact of the voltage activation threshold on vacuole excitability

Recently, the presence of TPC1 was reported to be a prerequisite for vacuole excitability. If no TPC1 channels are present in the vacuole membrane, the vacuole excitability is lost (Jaślan *et al.*, 2019). Moreover, the strength of vacuole excitability is related to the voltage activation threshold of TPC1. When hyperactive TPC1 channels (e.g. *fou2*) with a negatively shifted voltage activation threshold are targeted to the vacuole membrane, the vacuole membrane becomes hyperexcitable (Jaślan *et al.*, 2019). However, such vacuole hyperexcitability was not observed in the presence of the Arabidopsis AtTPC1 wild type channel (Jaślan *et al.*, 2019). The results in this thesis are consistent with this observation. When the voltage activation threshold of the TPC1 channel variants VfTPC1-WT and AtTPC1-E457N/E605A/D606N were shifted to negative potentials compared to AtTPC1-WT, the vacuole was

obviously hyperexcitable (Fig. 3.18, 3.19). However, hyperactive TPC1 channels will strongly affect plant growth in their natural environment (Bonaventure *et al.*, 2007b; Lenglet *et al.*, 2017). In case of the artificial hyperactive AtTPC1 mutant *fou2* (D454N), the plant growth is retarded because of the activation of the jasmonate-associated wounding responses. This suggests that the TPC1 channel activity must be controlled in the plant to avoid endless vacuolar excitation to protect the cells during this process. This would require controlling the voltage gating of TPC1 channel by reducing or enhancing the effect of inhibitory or stimulatory regulators of TPC1. The artificial expression of AtTPC1 wild type into an animal expression system pronouncedly shifted the channel gating to negative voltages compared with AtTPC1 expression in its natural plant vacuole system (Guo *et al.*, 2016). This also indicated that posttranslational modifications of TPC1 occur in planta or animal cell system that modulate TPC1 channel gating. These posttranslational modifications of TPC1 may include, for example, interaction with some regulatory proteins (e.g. kinase, phosphatase, 14-3-3 proteins) or lipid compounds/derivatives (Allen and Sanders, 1995; Bethke and Jones, 1997; Gutla *et al.*, 2012; Latz *et al.*, 2007; Schulz-Lessdorf and Hedrich, 1995). For instance, the protein phosphatase calcineurin showed a dual regulatory effect on SV/TPC1: an increase in calcineurin had an inhibitory effect on TPC1 activity while low concentrations of calcineurin promoted the activity of TPC1 (Allen and Sanders, 1995).

Regardless of how pronounced the luminal Ca^{2+} sensitivity of different SV/TPC1 channels is, it is undisputed that with an increasing Ca^{2+} concentration in the vacuole, more TPC1 channels will be inhibited (Fig. 3.4, 3.5, 3.18; Beyhl *et al.*, 2009; Dadacz-Narloch *et al.*, 2011; Guo *et al.*, 2016; Lenglet *et al.*, 2017; Pottosin *et al.*, 2004; Pottosin *et al.*, 1997). Moreover, the TPC1- dependent vacuole excitation can be downregulated by the high luminal Ca^{2+} concentration (Jaślan *et al.*, 2019). Besides, the vacuole excitation was reported to increase the cytosolic Ca^{2+} levels in intact plants by releasing Ca^{2+}

from the vacuole via a vacuole Ca^{2+} homeostat (Dindas *et al.*, 2021). Therefore, it seems that there is a close correlation between the vacuole excitation and the Ca^{2+} homeostat (Dindas *et al.*, 2021). Compared to a lower luminal Ca^{2+} concentration, a higher luminal Ca^{2+} concentration will cause a larger transmembrane Ca^{2+} gradient, therefore, a larger Ca^{2+} release from the vacuole will happen. However, when the Ca^{2+} homeostat depends on TPC1-dependent vacuolar excitation, the higher luminal Ca^{2+} concentration will inhibit the TPC1 activity more strongly. Then, the vacuole excitation will be reduced, resulting in turn in less Ca^{2+} release. Therefore, it seems that the vacuole excitation and the vacuole Ca^{2+} homeostat in plants are functionally linked and influence each other (Fig. 4.2).

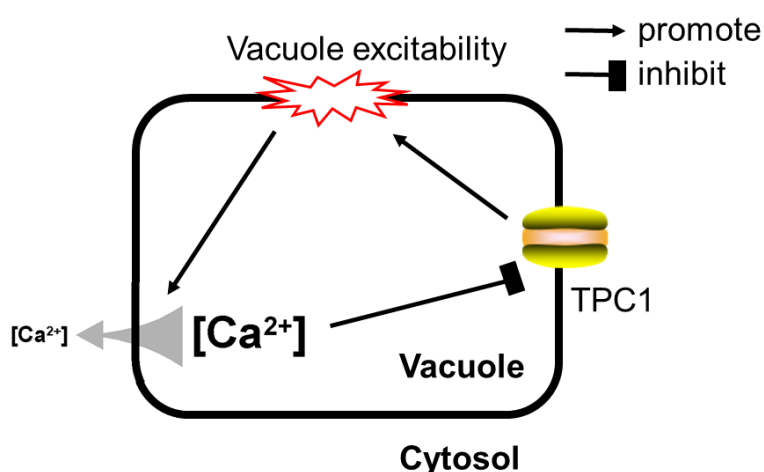


Fig. 4. 2. Functional link between vacuole excitation and the vacuole Ca^{2+} homeostat.

At a higher Ca^{2+} level in the vacuole, a larger transmembrane Ca^{2+} gradient (gray arrow) across the vacuole membrane is present, so that Ca^{2+} is pushed from the vacuole into the cytosol at an increased rate. However, the high luminal Ca^{2+} inhibits more the TPC1 channels, which in turn will attenuate TPC1-dependent excitation and thus reduce the Ca^{2+} release from the vacuole into the cytosol. Accordingly, the vacuole Ca^{2+} homeostat can be controlled by vacuole excitation, and vice versa.

4.5. Is VfTPC1 involved in Ca^{2+} release from vacuole *in vivo*?

It was suggested that the TPC1 channel may function in Calcium-Induced

Calcium Release (CICR) in plants, i.e. TPC1 channels directly release calcium ions into the cytoplasm after activation by a cytosolic Ca^{2+} signal. This was firstly proposed by Ward and Schroeder (1994) because they found that SV/TPC1 channels are Ca^{2+} -permeable (Ward and Schroeder, 1994) and combined with the observations that SV/TPC1 is the cytosolic Ca^{2+} activated (Hedrich *et al.*, 1987). The authors demonstrated that in the presence of 5 mM cytosolic Ca^{2+} and 50 mM vacuolar Ca^{2+} , the SV channel is capable to release calcium from the vacuole (Ward and Schroeder, 1994). Unfortunately, this ionic condition used in this publication was far away from physiological conditions for Ca^{2+} in native cellular environment which is more in the range of 0.1-1 μM Ca^{2+} in the cytosol and 0.2-2 mM Ca^{2+} in the lumen (Bethke and Jones, 1994; Felle *et al.*, 1988; Pérez *et al.*, 2008). Later, numerous experimental studies have been performed in *Arabidopsis thaliana* to prove whether TPC1 participates in CICR in planta (Choi *et al.*, 2014; Islam *et al.*, 2010; Peiter *et al.*, 2005; Ranf *et al.*, 2008). Scientists observed that the AtTPC1-loss-of-function disrupted stomatal closure in response to higher external Ca^{2+} compared with wild-type plants (Peiter *et al.*, 2005). However, this external calcium-induced cytosolic calcium transients observed in wild-type plants appeared to be not changed in *attpc1-2* (Islam *et al.*, 2010). Besides, loss of AtTPC1 function did not impair the Ca^{2+} responses triggered by various abiotic stressors (cold, hyperosmotic, salt and oxidative) and biotic effectors (*elf18*, *flg22*) (Ranf *et al.*, 2008). However, Choi *et al.* (2014), reported that salt-induced Ca^{2+} waves were still propagating from the root to the shoot in *attpc1-2* mutants but at reduced rates compared to wild type plants. These results suggested that the SV/TPC1 channel from *Arabidopsis thaliana* might not be directly responsible for the generation of cytosolic Ca^{2+} signals. This view is further supported by studies on the artificial *fou2* mutant from *Arabidopsis thaliana*. The *fou2* plants, equipped with this hyperactive TPC1 channel, showed an increased vacuolar Ca^{2+} content compared to wild type plants (Beyhl *et al.*, 2009). This observation, however, is contradictory to CICR, because if CICR occur with a hyperactive TPC1 channel,

more luminal Ca^{2+} should have been released, resulting in a lower luminal Ca^{2+} level and higher cytosolic Ca^{2+} (Beyhl *et al.*, 2009). In contrast, the *fou2* mutant was reported to have a slightly lower cytosolic Ca^{2+} level compared to wild type plants under both non-stressed and wounded conditions (Lenglet *et al.*, 2017). Thus, these studies on *fou2* does not seem to support the CICR hypothesis. Therefore, similar to the TPC1 channel mutant *fou2* from *Arabidopsis thaliana*, the hyperactive VfTPC1, which is also characterized by a voltage activation threshold at more physiological membrane potentials and an insensitivity to luminal Ca^{2+} (section 3.2.1), is unlikely to be involved in CICR under physiological conditions as well. Instead, a Ca^{2+} homeostat which is triggered by the TPC1-dependent vacuole excitation – as outlined in the previous section 4.4 – likely leads to vacuolar Ca^{2+} release (Dindas *et al.*, 2021). Thus, taken together, TPC1 is involved in Ca^{2+} signaling *in vivo*, but it seems that TPC1 itself does not act as a vacuolar Ca^{2+} release channel and indirectly shapes a cytosolic Ca^{2+} signal via a vacuolar Ca^{2+} homeostat which is triggered by TPC1-dependent vacuolar excitation.

4.6. The possible role of TPC1 in nodule-infected root cells of legumes during nitrogen fixation

Vicia faba belongs to the legume family. As legumes, the most notable feature is that they can interact with nitrogen-fixing rhizobia to establish a complicated root endosymbiosis. During the process, legumes form root nodules, where rhizobia live in and convert atmospheric nitrogen into ammonia and feed their host plant (Roth and Stacey, 1989). During the process of nitrogen-fixing, it has been reported that the K^+ concentration decreases in the vacuoles of nodule-infected cell (Fedorova *et al.*, 2021). Moreover, two potassium channels from the legume *Medicago truncatula*, the MtAKT1 (uptake of K^+ into cytosol) and MtGORK (release of cytosolic K^+) in plasma membrane are mistargeted and

are reduced in the nodule-infected cells (Fedorova *et al.*, 2021; Ivashikina *et al.*, 2001). These results indicate that the homeostasis of cytosolic K⁺ might be impaired in infected cells (Fedorova *et al.*, 2021). Because the vacuole functions as a K⁺ store and therefore is supposed to maintain the homeostasis of cytosolic K⁺ (Liu and Martinoia, 2020; Walker *et al.*, 1996), one could propose that the vacuolar K⁺ level decreases during the release of cytosolic K⁺ to the outside of plasma membrane in nodule-infected cell. When K⁺ is released from the cytosol, the cytosolic K⁺ concentration would be lower than in the vacuole. In order to keep homeostasis of cytosolic K⁺, vacuolar K⁺ will flow into the cytosol which would in turn result in a decreased vacuolar K⁺ level. Interestingly, when the K⁺ gradient across the vacuolar membrane is directed into the cytosol, the vacuolar TPC1 channel would be activated and mediates an inward K⁺ current into the cytosol (Ivashikina and Hedrich, 2005). Thus, in order to maintain the cytosolic K⁺ homeostasis of nodule-infected root cells of legumes, the VtTPC1 channel could contribute to K⁺ release from the vacuole, leading to reduced K⁺ levels in the vacuole.

5. Summary

The slowly activating vacuolar SV/TPC1 channel is ubiquitously expressed in plants and provides a large cation conductance in the vacuolar membrane. Thereby, monovalent (K^+ , Na^+) and in principle also divalent cations, such as Ca^{2+} , can pass through the channel. The SV/TPC1 channel is activated upon membrane depolarization and cytosolic Ca^{2+} but inhibited by luminal calcium. With respect to the latter, two luminal Ca^{2+} binding sites (site 1 Asp240/Asp454/Glu528, site 2 Glu239/Asp240/Glu457) were identified to coordinate luminal Ca^{2+} . In this work, the characteristics of the SV/TPC1 channels in terms of regulation and function were further elucidated, focusing on the TPC1s of *Arabidopsis thaliana* and *Vicia faba*. For electrophysiological analysis of the role of distinct pore residues for channel gating and luminal Ca^{2+} sensing, TPC1 channel variants were generated by site-directed mutagenesis and transiently expressed as eGFP/eYFP-fusion constructs in *Arabidopsis thaliana* mesophyll protoplasts of the TPC1 loss-of-function mutant *attpc1-2*.

1. As visualized by confocal fluorescence laser-scanning microscopy, all AtTPC1 (WT, E605A/Q, D606N, D607N, E605A/D606N, E605Q/D606N/D607N, E457N/E605A/D606N) and VfTPC1 channel variants (WT, N458E/A607E/N608D) were correctly targeted to the vacuole membrane.

2. Patch-clamp studies revealed that removal of one of the negative charges at position Glu605 or Asp606 was already sufficient to promote voltage-dependent channel activation with higher voltage sensitivity. The combined neutralization of these residues (E605A/D606N), however, was required to additionally reduce the luminal Ca^{2+} sensitivity of the AtTPC1 channel, leading to hyperactive AtTPC1 channels. Thus, the residues Glu605/Asp606 are functionally coupled with the voltage sensor of AtTPC1 channel, thereby modulating channel gating, and form a novel luminal Ca^{2+} sensing site 3 in AtTPC1 at the luminal entrance of the ion transport pathway.

3. Interestingly, this novel luminal Ca^{2+} sensing site 3 (Glu605/Asp606) and

Glu457 from the luminal Ca^{2+} sensing site 2 of the luminal Ca^{2+} -sensitive AtTPC1 channel were neutralized by either asparagine or alanine in the TPC1 channel from *Vicia faba* and many other Fabaceae. Moreover, the VfTPC1 was validated to be a hyperactive TPC1 channel with higher tolerance to luminal Ca^{2+} loads which was in contrast to the AtTPC1 channel features. As a result, VfTPC1 but not AtTPC1 conferred the hyperexcitability of vacuoles. When AtTPC1 was mutated for the three VfTPC1-homologous polymorphic site residues, the AtTPC1 triple mutant (E457N/E605A/D606N) gained VfTPC1-like characteristics. However, when VfTPC1 was mutated for the three AtTPC1-homologous polymorphic site residues, the VfTPC1 triple mutant (N458E/A607E/N608D) still sustained VfTPC1-WT-like features. These findings indicate that the hyperactivity of VfTPC1 is achieved in part by the loss of negatively charged amino acids at positions that - as part of the luminal Ca^{2+} sensing sites 2 and 3 – are homologous to AtTPC1-Glu457/Glu605/Asp606 and are likely stabilized by other unknown residues or domains.

4. The luminal polymorphic pore residues (Glu605/Asp606 in AtTPC1) apparently do not contribute to the unitary conductance of TPC1. Under symmetrical K^+ conditions, a single channel conductance of about 80 pS was determined for AtTPC1 wild type and the AtTPC1 double mutant E605A/D606A. This is in line with the three-fold higher unitary conductance of VfTPC1 (232 pS), which harbors neutral luminal pore residues at the homologous sites to AtTPC1.

In conclusion, by studying TPC1 channel from *Arabidopsis thaliana* and *Vicia faba*, the present thesis provides evidence that the natural TPC1 channel variants exhibit differences in voltage gating, luminal Ca^{2+} sensitivity and luminal Ca^{2+} binding sites.

6. Zusammenfassung

Der langsam aktivierende vakuoläre SV/TPC1-Kanal wird in Pflanzen ubiquitär exprimiert und besitzt eine große Kationenleitfähigkeit in der Vakuolenmembran. Dabei können einwertige (K^+ , Na^+) und im Prinzip auch zweiwertige Kationen, wie Ca^{2+} , den Kanal passieren. Der SV/TPC1-Kanal wird bei Membrandepolarisation und zytosolischem Ca^{2+} aktiviert, aber durch luminales Calcium gehemmt. In Bezug auf letzteres wurden zwei luminaire Ca^{2+} -Bindungsstellen (Seite I Asp240/Asp454/Glu528, Seite II Glu239/Asp240/Glu457) zwecks Koordination von luminalem Ca^{2+} identifiziert. In dieser Arbeit wurden die Eigenschaften der SV/TPC1-Kanäle in Bezug auf Regulierung und Funktion weiter aufgeklärt, wobei der Schwerpunkt auf den TPC1-Proteinen von *Arabidopsis thaliana* und *Vicia faba* lag. Zur elektrophysiologischen Analyse der Rolle verschiedener Porenaminosäuren für das Kanal-Gating und die luminaire Ca^{2+} -Erkennung wurden TPC1-Kanalvarianten durch gezielte Mutagenese erzeugt und transient als eGFP/eYFP-Fusionskonstrukte in Mesophyll-Protoplasten der TPC1-Verlustmutante *attpc1-2* von *Arabidopsis thaliana* exprimiert.

1. Mittels konfokaler Fluoreszenz-Laser-Scanning-Mikroskopie wurde anhand der eGFP- bzw. eYFP-Fluoreszenzsignale nachgewiesen, dass alle AtTPC1- (WT, E605A/Q, D606N, D607N, E605A/D606N, E605Q/D606N/D607N, E457N/E605A/D606N) und VfTPC1-Kanalvarianten (WT, N458E/A607E/N608D) korrekt in die Vakuolenmembran eingebaut wurden.

2. Patch-Clamp-Studien zeigten, dass die Entfernung einer der negativen Ladungen an den Positionen Glu605 oder Asp606 bereits ausreichte, um die spannungsabhängige Kanalaktivierung mit höherer Spannungsempfindlichkeit zu fördern. Die kombinierte Neutralisierung dieser Reste (E605A/D606N) war jedoch erforderlich, um die luminaire Ca^{2+} -Empfindlichkeit des AtTPC1-Kanals zusätzlich zu reduzieren, was zu hyperaktiven AtTPC1-Kanälen führte. Die

Aminosäurereste Glu605/Asp606 sind also funktionell mit dem Spannungssensor des AtTPC1-Kanals gekoppelt und modulieren dadurch das Kanaltor. Sie bilden eine neuartige luminalen Ca^{2+} -Sensorstelle 3 in AtTPC1 am luminalen Eingang des Ionen transportweges.

3. Interessanterweise waren diese Aminosäurereste Glu605/Asp606 der neuartigen luminalen Ca^{2+} -Sensorstelle 3 und Glu457 von der luminalen Ca^{2+} -Sensorstelle 2 des luminalen Ca^{2+} -empfindlichen AtTPC1-Kanals im TPC1-Kanal von *Vicia faba* und vielen anderen Fabaceae entweder durch Asparagin oder Alanin neutralisiert. Darüber hinaus wurde der VfTPC1 als hyperaktiver TPC1-Kanal mit höherer Toleranz gegenüber luminalen Ca^{2+} -Belastungen validiert, was im Gegensatz zu den Eigenschaften des AtTPC1-Kanals stand. Infolgedessen ist VfTPC1, nicht aber AtTPC1, für die hohe Erregbarkeit der Vakuolen verantwortlich. Wenn AtTPC1 für die drei VfTPC1-homologen polymorphen Stellen mutiert wurde, erhielt die AtTPC1-Dreifachmutante (E457N/E605A/D606N) VfTPC1-ähnliche Eigenschaften. Wenn VfTPC1 jedoch für die drei AtTPC1-homologen polymorphen Stellen mutiert wurde, behielt die VfTPC1-Dreifachmutante (N458E/A607E/N608D) weiterhin VfTPC1-WT-ähnliche Merkmale. Diese Ergebnisse deuten darauf hin, dass die Hyperaktivität von VfTPC1 zum Teil durch den Verlust von negativ geladenen Aminosäuren an Positionen erreicht wird, die - als Teil der luminalen Ca^{2+} -Sensorstellen 2 und 3 - homolog zu AtTPC1-Glu457/Glu605/Asp606 sind und wahrscheinlich durch andere unbekannte Reste oder Domänen stabilisiert werden.

4. Die luminalen polymorphen Porenreste (Glu605/Asp606 in AtTPC1) beeinflussen offenbar nicht die Einzelkanalleitfähigkeit von TPC1. Unter symmetrischen K^+ -Bedingungen wurde für den AtTPC1-Wildtyp und die AtTPC1-Doppelmutante E605A/D606A eine Einzelkanalleitfähigkeit von etwa 80 pS ermittelt. Dies steht im Einklang mit der dreifach höheren

Einzelkanalleitfähigkeit von VfTPC1 (232 pS), der an den homologen Stellen zu AtTPC1 neutrale luminale Porenreste aufweist.

Durch die Untersuchung von TPC1-Kanälen aus *Arabidopsis thaliana* und *Vicia faba* konnte in der vorliegenden Arbeit nachgewiesen werden, dass diese natürlichen TPC1-Kanalvarianten Unterschiede im Spannungs-Gating, der luminalen Ca^{2+} -Empfindlichkeit und den luminalen Ca^{2+} -Bindungsstellen aufweisen.

7. Table list

Table 2. 1. Primers used in this work.	18
Table 2. 2. PCR reaction (50 μ l) standard.....	20
Table 2. 3. Standard PacI enzyme digestion.....	21
Table 2. 4. Standard User enzyme reaction.....	21
Table 2. 5. Standard DPN 1 enzyme digestion.	22
Table 2. 6. Components of the DNA plasmids used in this study.	23
Table 2. 7. Components of LB agar plate.....	23
Table 2. 8. Components of LB medium.....	24
Table 2. 9. Components of lysis buffer.	25
Table 2. 10. Components of enzyme solution.	27
Table 2. 11. Components of W5 solution.....	27
Table 2. 12. Components of MMG solution.	27
Table 2. 13. Components of the PEG solution.	28
Table 2. 14. Solutions for whole-vacuole voltage clamp measurements.	45
Table 2. 15. Solutions for whole-vacuole current clamp measurements.	46
Table 2. 16. Solutions for single channel measurements.	46
Table 3. 1. The lifetime of the post-stimulus plateau phase (t_{plateau}) of TPC1 channel variants from all independent experiments.....	82
Table 4. 1. The unitary conductance of different TPC1 channel variants.	96

8. Figure list

Fig. 1. 1. Schematic representation of the representative pumps, antiporters and ion channels of vacuole transport systems.	3
Fig. 1. 2. Schematic representation of the <i>Arabidopsis thaliana</i> TPK1 topology.	7
Fig. 1. 3. Schematic representation of the secondary structure of an AtTPC1 subunit.	9
Fig. 2. 1. The principle of generation of point mutation with overlapping User primers.	19
Fig. 2. 2. Principle cloning procedure for the generation of site-directed mutagenesis constructs.	22
Fig. 2. 3. Four different patch-clamp configurations.	32
Fig. 2. 4. TPC1-activating voltage-pulse protocol for whole-vacuole current recordings.	36
Fig. 2. 5. TPC1-deactivating voltage-pulse protocol for whole-vacuole current recordings.	36
Fig. 2. 6. Representative analysis of the steady-state current density.	38
Fig. 2. 7. Representative analysis of relative channel open probability.	39
Fig. 2. 8. Principle of analysis of the half-activation time.	40
Fig. 2. 9. Representative analysis of the half-deactivation time.	41
Fig. 2. 10. Activating voltage-pulse protocol applied for single channel recordings.	42
Fig. 2. 11. Analysis of single channel conductance.	43
Fig. 2. 12. Current pulse protocol applied for voltage recordings.	44
Fig. 2. 13. Analysis of voltage recordings before, during and after current injection.	45
Fig. 3. 1. Subcellular localization of <i>Arabidopsis thaliana</i> TPC1 channel variants.	50

Fig. 3. 2. Macroscopic current responses of vacuoles transformed with AtTPC1 channel variants to voltage depolarization.....	52
Fig. 3. 3. Effect of voltage and luminal Ca ²⁺ on TPC1 currents mediated by different <i>Arabidopsis thaliana</i> channel variants.....	53
Fig. 3. 4. The voltage dependence of <i>Arabidopsis thaliana</i> TPC1 channel variant.	55
Fig. 3. 5. The voltage dependence of <i>Arabidopsis thaliana</i> TPC1 channel variant.	57
Fig. 3. 6. The gating charge movement of AtTPC1 channel variants.	60
Fig. 3. 7. Polymorphism of functional TPC1 channel domains with a role in luminal Ca ²⁺ coordination.....	62
Fig. 3. 8. The localization of <i>Vicia faba</i> TPC1 channels.	63
Fig. 3. 9. The activation and deactivation of <i>Arabidopsis thaliana</i> TPC1 and <i>Vicia faba</i> TPC1 channels.....	65
Fig. 3. 10. The voltage dependence of TPC1 channel from <i>Vicia faba</i> and <i>Arabidopsis thaliana</i>	67
Fig. 3. 11. The current responses of vacuoles harboring either <i>Arabidopsis thaliana</i> TPC1 or <i>Vicia faba</i> TPC1 channels under low and high luminal Ca ²⁺	68
Fig. 3. 12. The voltage dependence of TPC1 channels from <i>Vicia faba</i> and <i>Arabidopsis thaliana</i> under low and high luminal Ca ²⁺	69
Fig. 3. 13. Dependency of vacuole excitability on species-dependent TPC1 channel variants.....	71
Fig. 3. 14. Subcellular localization and electrophysiological characterization of AtTPC1 channel variants under 0 mM luminal Ca ²⁺ conditions.....	73
Fig. 3. 15. The voltage dependence of TPC1 channel variants.....	75
Fig. 3. 16. Activation and deactivation kinetics of AtTPC1 channel variants. .	76
Fig. 3. 17. Effect of luminal calcium on current response of TPC1 channel variants.	78
Fig. 3. 18. The voltage-dependent channel activity of TPC1 channel variants	

in response to different luminal Ca ²⁺	80
Fig. 3. 19. Dependency of vacuole excitability on TPC1 channel variants.	82
Fig. 3. 20. The voltage-dependent channel activity of VfTPC1 triple mutant (N458E/A607E/N608D).....	84
Fig. 3. 21. Single channel analysis of TPC1 channel variants.....	86
Fig. 4. 1. The working model of the voltage sensor from AtTPC1 channel.....	90
Fig. 4. 2. Functional link between vacuole excitation and the vacuole Ca ²⁺ homeostat.	100

9. Reference

Allen GJ, Sanders D. 1995. Calcineurin, a type 2B protein phosphatase, modulates the Ca²⁺-permeable slow vacuolar ion channel of stomatal guard cells. *The Plant Cell* **7**, 1473-1483.

Amodeo G, Escobar A, Zeiger E. 1994. A cationic channel in the guard cell tonoplast of *Allium cepa*. *Plant Physiology* **105**, 999-1006.

Becker D, Geiger D, Dunkel M, Roller A, Bertl A, Latz A, Carpaneto A, Dietrich P, Roelfsema M, Voelker C. 2004. AtTPK4, an Arabidopsis tandem-pore K⁺ channel, poised to control the pollen membrane voltage in a pH- and Ca²⁺-dependent manner. *Proceedings of the National Academy of Sciences* **101**, 15621-15626.

Behringer D, Zimmermann H, Ziegenhagen B, Liepelt S. 2015. Differential gene expression reveals candidate genes for drought stress response in *Abies alba* (Pinaceae). *PLoS One* **10**, e0124564.

Bertl A, Blumwald E, Coronado R, Eisenberg R, Findlay G, Gradmann D, Hille B, Köhler K, Kolb H-A, MacRobbie EJS. 1992. Electrical measurements on endomembranes. *Science* **258**, 873-874.

Bethke PC, Jones RL. 1994. Ca²⁺-calmodulin modulates ion channel activity in storage protein vacuoles of barley aleurone cells. *The Plant Cell* **6**, 277-285.

Bethke PC, Jones RL. 1997. Reversible protein phosphorylation regulates the activity of the slow-vacuolar ion channel. *The Plant Journal* **11**, 1227-1235.

Beyhl D, Hörtensteiner S, Martinoia E, Farmer EE, Fromm J, Marten I, Hedrich R. 2009. The *fou2* mutation in the major vacuolar cation channel TPC1 confers tolerance to inhibitory luminal calcium. *The Plant Journal* **58**, 715-723.

Bonaventure G, Gfeller A, Proebsting WM, Hörtensteiner S, Chételat A, Martinoia E, Farmer EE. 2007a. A gain-of-function allele of TPC1 activates oxylipin biogenesis after leaf wounding in Arabidopsis. *The Plant Journal* **49**, 889-898.

Bonaventure G, Gfeller A, Rodríguez VM, Armand F, Farmer EE. 2007b. The

fou2 gain-of-function allele and the wild-type allele of Two Pore Channel 1 contribute to different extents or by different mechanisms to defense gene expression in Arabidopsis. *Plant and Cell Physiology* **48**, 1775-1789.

Brelidze TI, Niu X, Magleby KL. 2003. A ring of eight conserved negatively charged amino acids doubles the conductance of BK channels and prevents inward rectification. *Proceedings of the National Academy of Sciences* **100**, 9017-9022.

Brüggemann LI, Pottosin II, Schönknecht G. 1998. Cytoplasmic polyamines block the fast-activating vacuolar cation channel. *The Plant Journal* **16**, 101-105.

Brüggemann LI, Pottosin II, Schönknecht G. 1999a. Cytoplasmic magnesium regulates the fast activating vacuolar cation channel. *Journal of Experimental Botany* **50**, 1547-1552.

Brüggemann LI, Pottosin II, Schönknecht G. 1999b. Selectivity of the fast activating vacuolar cation channel. *Journal of Experimental Botany* **50**, 873-876.

Capozzi F, Casadei F, Luchinat C. 2006. EF-hand protein dynamics and evolution of calcium signal transduction: an NMR view. *Journal of Biological Inorganic Chemistry* **11**, 949-962.

Carpaneto A, Cantu' AM, Busch H, Gambale F. 1997. Ion channels in the vacuoles of the seagrass *Posidonia oceanica*. *FEBS Letters* **412**, 236-240.

Carpaneto A, Cantù AM, Gambale F. 1999. Redox agents regulate ion channel activity in vacuoles from higher plant cells. *FEBS Letters* **442**, 129-132.

Carpaneto A, Cantù AM, Gambale F. 2001. Effects of cytoplasmic Mg²⁺ on slowly activating channels in isolated vacuoles of *Beta vulgaris*. *Planta* **213**, 457-468.

Choi W-G, Toyota M, Kim S-H, Hilleary R, Gilroy S. 2014. Salt stress-induced Ca²⁺ waves are associated with rapid, long-distance root-to-shoot signaling in plants. *Proceedings of the National Academy of Sciences* **111**, 6497-6502.

Cormack BP, Valdivia RH, Falkow S. 1996. FACS-optimized mutants of the green fluorescent protein (GFP). *Gene* **173**, 33-38.

Coyaud L, Kurkdjian A, Kado R, Hedrich R. 1987. Ion channels and ATP-driven pumps involved in ion transport across the tonoplast of sugarbeet vacuoles. *Biochimica et Biophysica Acta (BBA)-Biomembranes* **902**, 263-268.

Dadacz-Narloch B, Beyhl D, Larisch C, López-Sanjurjo EJ, Reski R, Kuchitsu K, Müller TD, Becker D, Schönknecht G, Hedrich R. 2011. A novel calcium binding site in the slow vacuolar cation channel TPC1 senses luminal calcium levels. *The Plant Cell* **23**, 2696-2707.

Dadacz-Narloch B, Kimura S, Kurusu T, Farmer EE, Becker D, Kuchitsu K, Hedrich RJNP. 2013. On the cellular site of two-pore channel TPC 1 action in the Poaceae. *New Phytologist* **200**, 663-674.

De Angeli A, Zhang J, Meyer S, Martinoia E. 2013. AtALMT9 is a malate-activated vacuolar chloride channel required for stomatal opening in Arabidopsis. *Nature communications* **4**, 1-10.

de Vries H. 1885. *Die Plasmolytische Studien über die Wand Vacuolen.* G. Bernstein.

Dindas J, Dreyer I, Huang S, Hedrich R, Roelfsema MRG. 2021. A voltage-dependent Ca²⁺ homeostat operates in the plant vacuolar membrane. *New Phytologist* **230**, 1449-1460.

Dreyer I, Sussmilch FC, Fukushima K, Riadi G, Becker D, Schultz J, Hedrich R. 2021. How to grow a tree: plant voltage-dependent cation channels in the spotlight of evolution. *Trends in Plant Science* **26**, 41-52.

Dujardin F. 1841. *Histoire naturelle des zoophytes: Infusoires, comprenant la physiologie et la classification de ces animaux, et la manière de les étudier à l'aide du microscope.* Roret.

Echeverria E, Burns JK. 1989. Vacuolar acid hydrolysis as a physiological mechanism for sucrose breakdown. *Plant Physiology* **90**, 530-533.

Eisenach C, Baetz U, Huck NV, Zhang J, De Angeli A, Beckers GJ, Martinoia E. 2017. ABA-induced stomatal closure involves ALMT4, a phosphorylation-dependent vacuolar anion channel of Arabidopsis. *The Plant*

Cell **29**, 2552-2569.

Ettxeberria E, Pozueta-Romero J, Gonzalez P. 2012. In and out of the plant storage vacuole. *Plant Science* **190**, 52-61.

Fedorova EE, Coba de la Pena T, Lara-Dampier V, Trifonova NA, Kulikova O, Pueyo JJ, Lucas MM. 2021. Potassium content diminishes in infected cells of *Medicago truncatula* nodules due to the mislocation of channels MtAKT1 and MtSKOR/GORK. *Journal of Experimental Botany* **72**, 1336-1348.

Felle H. 1988. Cytoplasmic free calcium in *Riccia fluitans* L. and *Zea mays* L.: Interaction of Ca²⁺ and pH? *Planta* **176**, 248-255.

Furuichi T, Cunningham KW, Muto S. 2001. A putative two pore channel AtTPC1 mediates Ca²⁺ flux in Arabidopsis leaf cells. *Plant and Cell Physiology* **42**, 900-905.

Gaxiola RA, Palmgren MG, Schumacher K. 2007. Plant proton pumps. *FEBS Letters* **581**, 2204-2214.

Gobert A, Isayenkov S, Voelker C, Czempinski K, Maathuis FJ. 2007. The two-pore channel TPK1 gene encodes the vacuolar K⁺ conductance and plays a role in K⁺ homeostasis. *Proceedings of the National Academy of Sciences* **104**, 10726-10731.

Grefen C, Donald N, Hashimoto K, Kudla J, Schumacher K, Blatt MR. 2010. A ubiquitin-10 promoter-based vector set for fluorescent protein tagging facilitates temporal stability and native protein distribution in transient and stable expression studies. *The Plant Journal* **64**, 355-365.

Guo J, Zeng W, Chen Q, Lee C, Chen L, Yang Y, Cang C, Ren D, Jiang Y. 2016. Structure of the voltage-gated two-pore channel TPC1 from *Arabidopsis thaliana*. *Nature* **531**, 196-201.

Gutla PVK, Boccaccio A, De Angeli A, Gambale F, Carpaneto A. 2012. Modulation of plant TPC channels by polyunsaturated fatty acids. *Journal of Experimental Botany* **63**, 6187-6197.

Hamamoto S, Marui J, Matsuoka K, Higashi K, Igarashi K, Nakagawa T, Kuroda T, Mori Y, Murata Y, Nakanishi Y. 2008. Characterization of a tobacco

TPK-type K⁺ channel as a novel tonoplast K⁺ channel using yeast tonoplasts. *Journal of Biological Chemistry* **283**, 1911-1920.

Hamill OP, Sakmann B. 1981. Multiple conductance states of single acetylcholine receptor channels in embryonic muscle cells. *Nature* **294**, 462-464.

Hedrich R, Flügge U, Fernandez J. 1986. Patch-clamp studies of ion transport in isolated plant vacuoles. *FEBS Letters* **204**, 228-232.

Hedrich R, Kurkdjian A, Guern J, Flügge U. 1989. Comparative studies on the electrical properties of the H⁺ translocating ATPase and pyrophosphatase of the vacuolar-lysosomal compartment. *The EMBO journal* **8**, 2835-2841.

Hedrich R, Marten I. 2011. TPC1-SV channels gain shape. *Molecular Plant* **4**, 428-441.

Hedrich R, Mueller TD, Becker D, Marten I. 2018. Structure and function of TPC1 vacuole SV channel gains shape. *Molecular Plant* **11**, 764-775.

Hedrich R, Neher E. 1987. Cytoplasmic calcium regulates voltage-dependent ion channels in plant vacuoles. *Nature* **329**, 833-836.

Hedrich R, Schroeder JI. 1989. The physiology of ion channels and electrogenic pumps in higher plants. *Annual Review of Plant Biology* **40**, 539-569.

Hedrich R. 2012. Ion channels in plants. *Physiological reviews* **92**, 1777-1811.

Herman EM, Larkins BA. 1999. Protein storage bodies and vacuoles. *The Plant Cell* **11**, 601-613.

Hille B. 1992. G protein-coupled mechanisms and nervous signaling. *Neuron* **9**, 187-195.

Höfte H, Hubbard L, Reizer J, Ludevid D, Herman EM, Chrispeels MJ. 1992. Vegetative and seed-specific forms of tonoplast intrinsic protein in the vacuolar membrane of *Arabidopsis thaliana*. *Plant Physiology* **99**, 561-570.

Hoh B, Hinz G, Jeong B-K, Robinson DG. 1995. Protein storage vacuoles form *de novo* during pea cotyledon development. *Journal of Cell Science* **108**,

299-310.

Isayenkov S, Isner JC, Maathuis FJM. 2010. Vacuolar ion channels: Roles in plant nutrition and signalling. *FEBS Letters* **584**, 1982-1988.

Islam MM, Munemasa S, Hossain MA, Nakamura Y, Mori IC, Murata Y. 2010. Roles of AtTPC1, vacuolar two pore channel 1, in Arabidopsis stomatal closure. *Plant and Cell Physiology* **51**, 302-311.

Ivashikina N, Becker D, Ache P, Meyerhoff O, Felle HH, Hedrich R. 2001. K⁺ channel profile and electrical properties of Arabidopsis root hairs. *FEBS Letters* **508**, 463-469.

Ivashikina N, Hedrich R. 2005. K⁺ currents through SV-type vacuolar channels are sensitive to elevated luminal sodium levels. *The Plant Journal* **41**, 606-614.

Jaślan D, Dreyer I, Lu J, O'Malley R, Dindas J, Marten I, Hedrich R. 2019. Voltage-dependent gating of SV channel TPC1 confers vacuole excitability. *Nature Communications* **10**, 1-9.

Jaślan D, Mueller T, Becker D, Schultz J, Cuin T, Marten I, Dreyer I, Schönknecht G, Hedrich R. 2016. Gating of the two-pore cation channel AtTPC1 in the plant vacuole is based on a single voltage-sensing domain. *Plant Biology* **18**, 750-760.

Jiang Y, Lee A, Chen J, Cadene M, Chait BT, MacKinnon R. 2002. The open pore conformation of potassium channels. *Nature* **417**, 523-526.

Johannes E, Sanders D. 1995. Luminal calcium modulates unitary conductance and gating of a plant vacuolar calcium release channel. *The Journal of Membrane Biology* **146**, 211-224.

Kawano T, Kadono T, Fumoto K, Lapeyrie F, Kuse M, Isobe M, Furuichi T, Muto S. 2004. Aluminum as a specific inhibitor of plant TPC1 Ca²⁺ channels. *Biochemical and Biophysical Research Communications* **324**, 40-45.

Kintzer AF, Green EM, Dominik PK, Bridges M, Armache JP, Deneka D, Kim SS, Hubbell W, Kossiakoff AA, Cheng Y, Stroud RM. 2018. Structural basis for activation of voltage sensor domains in an ion channel TPC1. *Proceedings of the National Academy of Sciences* **115**, E9095-E9104.

Kintzer AF, Stroud RM. 2018. On the structure and mechanism of two-pore channels. *The FEBS Journal* **285**, 233-243.

Kintzer AF, Stroud R. 2016. Structure, inhibition and regulation of two-pore channel TPC1 from *Arabidopsis thaliana*. *Nature* **531**, 258-264.

Kolb H-A, Köhler K, Martinoia E. 1987. Single potassium channels in membranes of isolated mesophyll barley vacuoles. *The Journal of Membrane Biology* **95**, 163-169.

Kovermann P, Meyer S, Hörtensteiner S, Picco C, Scholz-Starke J, Ravera S, Lee Y, Martinoia E. 2007. The *Arabidopsis* vacuolar malate channel is a member of the ALMT family. *The Plant Journal* **52**, 1169-1180.

Krebs M, Beyhl D, Görlich E, Al-Rasheid KA, Marten I, Stierhof Y-D, Hedrich R, Schumacher K. 2010. *Arabidopsis* V-ATPase activity at the tonoplast is required for efficient nutrient storage but not for sodium accumulation. *Proceedings of the National Academy of Sciences* **107**, 3251-3256.

Krüger F, Schumacher K. 2018. Pumping up the volume-vacuole biogenesis in *Arabidopsis thaliana*. *Seminars in Cell & Developmental Biology* **80**, 106-112.

Lagostena L, Festa M, Pusch M, Carpaneto A. 2017. The human two-pore channel 1 is modulated by cytosolic and luminal calcium. *Scientific Reports* **7**, 1-11.

Larisch N, Kirsch SA, Schambony A, Studtrucker T, Böckmann RA, Dietrich P. 2016. The function of the two-pore channel TPC1 depends on dimerization of its carboxy-terminal helix. *Cellular and Molecular Life Sciences* **73**, 2565-2581.

Larisch N, Schulze C, Galione A, Dietrich P. 2012. An N-terminal dileucine motif directs two-pore channels to the tonoplast of plant cells. *Traffic* **13**, 1012-1022.

Latorre R, Castillo K, Carrasquel-Ursulaez W, Sepulveda RV, Gonzalez-Nilo F, Gonzalez C, Alvarez O. 2017. Molecular determinants of BK channel

functional diversity and functioning. *Physiological Reviews* **97**, 39-87.

Latz A, Becker D, Hekman M, Müller T, Beyhl D, Marten I, Eing C, Fischer A, Dunkel M, Bertl A. 2007. TPK1, a Ca²⁺-regulated Arabidopsis vacuole two-pore K⁺ channel is activated by 14-3-3 proteins. *The Plant Journal* **52**, 449-459.

Lenglet A, Jašlan D, Toyota M, Mueller M, Müller T, Schönknecht G, Marten I, Gilroy S, Hedrich R, Farmer E. 2017. Control of basal jasmonate signalling and defence through modulation of intracellular cation flux capacity. *New Phytologist* **216**, 1161-1169.

Lin C, Yu Y, Kadono T, Iwata M, Umemura K, Furuichi T, Kuse M, Isobe M, Yamamoto Y, Matsumoto H. 2005. Action of aluminum, novel TPC1-type channel inhibitor, against salicylate-induced and cold-shock-induced calcium influx in tobacco BY-2 cells. *Biochemical and Biophysical Research Communications* **332**, 823-830.

Liu G, Martinoia E. 2020. How to survive on low potassium. *Nature Plants* **6**, 332-333.

Marcel D, Müller T, Hedrich R, Geiger D. 2010. K⁺ transport characteristics of the plasma membrane tandem-pore channel TPK4 and pore chimeras with its vacuolar homologs. *FEBS Letters* **584**, 2433-2439.

Martinoia E, Meyer S, De Angeli A, Nagy R. 2012. Vacuolar transporters in their physiological context. *Annual Review of Plant Biology* **63**, 183-213.

Marty F. 1999. Plant Vacuoles. *The Plant Cell* **11**, 587-599.

Meyer S, Scholz-Starke J, De Angeli A, Kovermann P, Burla B, Gambale F, Martinoia E. 2011. Malate transport by the vacuolar AtALMT6 channel in guard cells is subject to multiple regulation. *The Plant Journal* **67**, 247-257.

Mullis K, Faloona F, Scharf S, Saiki R, Horn G, Erlich H. 1986. Specific enzymatic amplification of DNA in vitro: the polymerase chain reaction. *Cold Spring Harbor Symposia on Quantitative Biology*, Cold Spring Harbor Laboratory Press **51**, 263-273.

Naranjo D, Moldenhauer H, Pincuntureo M, Díaz-Franulic I. 2016. Pore size

matters for potassium channel conductance. *Journal of General Physiology* **148**, 277-291.

Navarro-Retamal C, Schott-Verdugo S, Gohlke H, Dreyer I. 2021. Computational analyses of the AtTPC1 (Arabidopsis Two-Pore Channel 1) permeation pathway. *International Journal of Molecular Sciences* **22**, 10345.

Neher E, Sakmann B. 1976a. Noise analysis of drug induced voltage clamp currents in denervated frog muscle fibres. *The Journal of Physiology* **258**, 705-729.

Neher E, Sakmann B. 1976b. Single-channel currents recorded from membrane of denervated frog muscle fibres. *Nature* **260**, 799-802.

Nimigean CM, Chappie JS, Miller C. 2003. Electrostatic tuning of ion conductance in potassium channels. *Biochemistry* **42**, 9263-9268.

Nour-Eldin HH, Hansen BG, Nørholm MH, Jensen JK, Halkier BA. 2006. Advancing uracil-excision based cloning towards an ideal technique for cloning PCR fragments. *Nucleic Acids Research* **34**, e122-e122.

Paris N, Stanley CM, Jones RL, Rogers JC. 1996. Plant cells contain two functionally distinct vacuolar compartments. *Cell* **85**, 563-572.

Peiter E, Maathuis FJ, Mills LN, Knight H, Pelloux J, Hetherington AM, Sanders D. 2005. The vacuolar Ca²⁺-activated channel TPC1 regulates germination and stomatal movement. *Nature* **434**, 404-408.

Pérez V, Wherrett T, Shabala S, Muniz J, Dobrovinskaya O, Pottosin I. 2008. Homeostatic control of slow vacuolar channels by luminal cations and evaluation of the channel-mediated tonoplast Ca²⁺ fluxes in situ. *Journal of Experimental Botany* **59**, 3845-3855.

Pottosin I, Dobrovinskaya O. 2014. Non-selective cation channels in plasma and vacuolar membranes and their contribution to K⁺ transport. *Journal of Plant Physiology* **171**, 732-742.

Pottosin I, Schönknecht G. 2007. Vacuolar calcium channels. *Journal of Experimental Botany* **58**, 1559-1569.

Pottosin II, Martínez-Estévez M, Dobrovinskaya OR, Muniz J,

Schönknecht G. 2004. Mechanism of luminal Ca^{2+} and Mg^{2+} action on the vacuolar slowly activating channels. *Planta* **219**, 1057-1070.

Pottosin II, Tikhonova LI, Hedrich R, Schönknecht G. 1997. Slowly activating vacuolar channels can not mediate Ca^{2+} -induced Ca^{2+} release. *The Plant Journal* **12**, 1387-1398.

Ranf S, Wunnenberg P, Lee J, Becker D, Dunkel M, Hedrich R, Scheel D, Dietrich P. 2008. Loss of the vacuolar cation channel, AtTPC1, does not impair Ca^{2+} signals induced by abiotic and biotic stresses. *The Plant Journal* **53**, 287-299.

Rienmüller F, Dreyer I, Schönknecht G, Schulz A, Schumacher K, Nagy R, Martinoia E, Marten I, Hedrich R. 2012. Luminal and cytosolic pH feedback on proton pump activity and ATP affinity of V-type ATPase from Arabidopsis. *Journal of Biological Chemistry* **287**, 8986-8993.

Schonknecht G. 2013. Calcium Signals from the Vacuole. *Plants* **2**, 589-614.

Schulz-Lessdorf B, Hedrich R. 1995. Protons and calcium modulate SV-type channels in the vacuolar-lysosomal compartment—channel interaction with calmodulin inhibitors. *Planta* **197**, 655-671.

Schulze C, Sticht H, Meyerhoff P, Dietrich P. 2011. Differential contribution of EF-hands to the Ca^{2+} -dependent activation in the plant two-pore channel TPC1. *The Plant Journal* **68**, 424-432.

Shimada T, Takagi J, Ichino T, Shirakawa M, Hara-Nishimura I. 2018. Plant vacuoles. *Annual Review of Plant Biology* **69**, 123-145.

Shoffner MA, Cheng J, Hvichia GE, Kricka LJ, Wilding P. 1996. Chip PCR. I. Surface passivation of microfabricated silicon-glass chips for PCR. *Nucleic Acids Research* **24**, 375-379.

Tao X, Lee A, Limapichat W, Dougherty DA, MacKinnon R. 2010. A gating charge transfer center in voltage sensors. *Science* **328**, 67-73.

Tikhonova LI, Pottosin II, Dietz KJ, Schönknecht G. 1997. Fast-activating cation channel in barley mesophyll vacuoles. Inhibition by calcium. *The Plant*

Journal **11**, 1059-1070.

van Leeuwenhoek A. 1800. *The select works of anthony van leeuwenhoek: containing his microscopical discoveries in many of the works of nature.* Translator.

Vitale A, Hinz G. 2005. Sorting of proteins to storage vacuoles: how many mechanisms? *Trends in Plant Science* **10**, 316-323.

Vitale A, Raikhel NV. 1999. What do proteins need to reach different vacuoles? *Trends in Plant Science* **4**, 149-155.

Walker DJ, Leigh RA, Miller AJ. 1996. Potassium homeostasis in vacuolate plant cells. *Proceedings of the National Academy of Sciences* **93**, 10510-10514.

Wang Y-J, Yu J-N, Chen T, Zhang Z-G, Hao Y-J, Zhang J-S, Chen S-Y. 2005. Functional analysis of a putative Ca²⁺ channel gene TaTPC1 from wheat. *Journal of Experimental Botany* **56**, 3051-3060.

Ward JM, Schroeder JI. 1994. Calcium-activated K⁺ channels and calcium-induced calcium release by slow vacuolar ion channels in guard cell vacuoles implicated in the control of stomatal closure. *The Plant Cell* **6**, 669-683.

Weber E, Neumann D. 1980. Protein bodies, storage organelles in plant seeds. *Biochemie und Physiologie der Pflanzen* **175**, 279-306.

Wink M. 1993. The plant vacuole: a multifunctional compartment. *Journal of Experimental Botany* **8**, 231-246.

Yoo SD, Cho YH, Sheen J. 2007. Arabidopsis mesophyll protoplasts: a versatile cell system for transient gene expression analysis. *Nature Protocols* **2**, 1565-1572.

Zhou Y, Xia X-M, Lingle CJ. 2011. Cysteine scanning and modification reveal major differences between BK channels and Kv channels in the inner pore region. *Proceedings of the National Academy of Sciences* **108**, 12161-12166.

10. Glossary

°C	degree Celsius
μM	micro molar
A	alanine
AD/DA	analog-to-digital
Ag	silver
AgCl	silver chloride
Ala	alanine
ALMT	Al ³⁺ -activated malate transporters
Asn	asparagine
Asp	aspartic acid
bp	base pair
BSA	bovine serum albumin
C ₁	first close state
C ₂	second close state
Ca ²⁺	calcium ion
CAX	Ca ²⁺ / H ⁺ antiporter
Cl ⁻	chloride ion
C _m	membrane capacitance
Cs ⁺	cesium ion
D	aspartic acid
dNTPs	deoxynucleotide
E	glutamic acid
e ⁻	electron
e.g	exempli gratia
eGFP	enhanced green fluorescent protein
EGTA	ethylene glycol-bis(β-aminoethyl ether)-N,N,N',N'-tetraacetic acid
E _N	nernst potential
exp	exponential
eYFP	enhanced yellow fluorescent protein
FV	fast vacuolar
fwd	forward
g	gram
<i>g</i>	gravity acceleration
Gln	glutamine
Glu	glutamic acid
G _{max}	maximal open probability
h	hour
H ⁺	proton
HEPES	4-(2-hydroxyethyl)-1-piperazineethanesulfonic acid
I	isoleucine
I _{0.5}	half maximum current
I _{deact-0.5}	half-deactivation time
I _{inst}	instantaneous current
I _{leak}	leak current

I_{max}	maximum current
I_{ss}	steady-state current
I_{ss} (V)	steady-state current in certain voltage
I_{ss}/C_m	steady-state current density
I_t	tail currents
JA	jasmonic acid
K^+	potassium ion
K_B	michaelis constant
kHz	kilo Hertz
L	liter
LB media	luria-Bertani media
Li^+	lithium ion
LJP	liquid junction potential
M	molar
M	methionine
MES	2-(N-morpholino) ethanesulfonic acid
Met	methionine
Mg^{2+}	magnesium ion
mL	millilitre
mm	millimetre
mM	milimolar
MMg	mannitol magnesium buffer
$mosmol\ kg^{-1}$	milliosmole per kilogram
ms	millisecond
mV	millivolt
$M\Omega$	mega ohm
N	asparagine
Na^+	sodium ion
NH_4^+	ammonium cation
nm	nanometer
nM	nanomolar
NO_3^-	nitrate ion
N_{total}	total number of channels
O	open state
OD	optical density
pA	picoampere
PEG	polyetyloglicol
pH	proton concentration
P_o (V)	open probability in certain voltage
PP	pyrophosphate
Q	glutamine
R	arginine
Rb^+	rubidium ion
rel. P_o (V)	relative open probability in certain voltage
rev	revers
s	second
SV	slow vacuolar
$t_{act-0.5}$	half-activation time

TPC1	Two Pore Channel
<i>tpc1-2</i>	Two Pore Channel knock-out mutant
TPK	tandem pore K ⁺
Tris	(hydroxymethyl) aminomethane
UBQ10	ubiquitin10
V	volt
V	valine
v/v	volume/volume
V ₁	midpoint voltage reflecting the C ₁ ⇌ O transition
V ₂	midpoint voltage reflecting the C ₂ ⇌ C ₁ transition
V-ATPase	ATP-driven pump for vacuolar H ⁺ accumulation
VK	vacuolar potassium
V _m	membrane voltage
V-PPase	pyrophosphate-driven pump for vacuolar H ⁺ accumulation
W5	incubation buffer in protoplast transformation procedure
z ₁	gating charge 1
z ₂	gating charge 2
μl	microliter
μm	micrometer
μmol s ⁻¹ m ⁻²	micromole per second and square meter
μs	microsecond
π	osmotic pressure

11. Curriculum Vitae

Jinping Lu

jinpings.lu@stud-mail.uni-wuerzburg.de

- Personal** Female
Born on March 7, 1990
Chinese citizen
- Education**
- BS** Henan Agriculture University
Horticulture
09/2009-06/2013
Thesis "Efficient and timely cultivation techniques for pepper in open field"
Major GPA:3.30/4.00 Overall GPA:3.32/4.00
- MS** Northwest A&F University
Vegetable
09/2013-06/2016
Thesis "Function identification of pepper heavy metal transporter protein gene *CaHMA1* under high temperature and heavy-metal stress"
Supervisor: A. P. Minghui, Lu
Major GPA:3.44/4.00 Overall GPA:3.48/4.00
- PhD** University of Würzburg
Plant-physiology and biophysics
12/2016-12/2021
Thesis: "The vacuolar TPC1 channel and its luminal calcium sensing site in the luminal pore entrance"
Supervisor: Prof. Rainer Hedrich and Prof. Irene Marten

12. Publication list

Parts of this work was accepted for publication as an peer-reviewed article in the journal “*Proc. Natl. Acad. Sci. USA*” .

Miles Sasha Dickinson*, Jinping Lu*, Meghna Gupta, Irene Marten, Rainer Hedrich, Robert M. Stroud. ‘Molecular basis of multistep voltage activation in plant two-pore channel 1’ (* **equal contribution**)

Parts of this work in preparation for publication.

Jinping Lu, Miles Sasha Dickinson, Ingo Dreyer, Sabine Panzer, Ulrich Terpitz, Dawid Jaslan, Carlos Navarro-Retamal, Dietmar Geiger, Dirk Becker, Robert M. Strout, Irene Marten, Rainer Hedrich. ‘*Vicia faba* TPC1 is a genetically encoded hyperactive variant of the vacuole Two Pore Channel 1’

Peer-reviewed publication not part of this dissertation.

Jaślan Dawid, Ingo Dreyer, Jinping Lu, Ronan O’Malley, Julian Dindas, Irene Marten, and Rainer Hedrich. *Nature communications*. 2019. 'Voltage-dependent gating of SV channel TPC1 confers vacuole excitability', 10: 1-9.

13. Acknowledgements

I would like to thank Prof. Dr. Rainer Hedrich, the Chair of Botany I at the Julius von Sachs Institute of the Julius Maximilians, University of Würzburg, who gave me the opportunity to perform my PhD work in his biophysics lab with excellent working conditions.

I would like to express my special thanks to Prof. Dr. Irene Marten, who guided me to the door of electrophysiology field with her professional knowledge. Over the past 5 years, when needed, she was always on the side for supporting me to solve problems. Without her endless patience, constructive advice and useful discussion, I cannot finish my thesis.

I also would like to express my thanks to Prof. Dr. Erhard Wischmeyer for his evaluation of my annual reports as my second referee.

My thanks also go to Prof. Dr. Dietmar Geiger, Prof. Dr. Ingo Dreyer, Prof. Dr. Robert Stroud, Dr. Ulrich Terpitz and Dr. Miles Sasha Dickinson for their scientific suggestions and friendly cooperation.

Thanks also should go to my colleagues Dr. Dawid Jaślan, Dr. Justyna Jaślan, Dr. Shouguang Huang, Dr. Dorothea Graus, Dr. Akiko Rasmussen and the other employees Kerstin Neuwinger, Dr. Christian Wiese, Joachim Rothenhöfer, who always offered me help and created a pleasant working atmosphere.

Of course, I would like to thank my friend Juanjuan Cao, Kunkun Li, Meiqi Ding for always treating me with delicious Chinese food.

My heartfelt thank owes to my family for their many years' support, patience and understanding during my studies and my dissertation. I would like to specially thank Kunxi Zhang for his love, patience and support.

At last, I would also thank China Scholarship Council (CSC) and German Academic Exchange Service (DAAD) for financial support on me to study in Germany.

14. Affidavit in English and German

I hereby declare that my thesis entitled: „ **The vacuolar TPC1 channel and its luminal calcium sensing site in the luminal pore entrance**” is the result of my own work. I did not receive any help or support from commercial consultants. All sources and / or materials applied are listed and specified in the thesis.

Furthermore I verify that the thesis has not been submitted as part of another examination process neither in identical nor in similar form.

Besides I declare that if I do not hold the copyright for figures and paragraphs, I obtained it from the rights holder and that paragraphs and figures have been marked according to law or for figures taken from the internet the hyperlink has been added accordingly.

Würzburg, den _____

Jinping Lu

Eidesstattliche Erklärungen nach §7 Abs. 2 Satz 3, 4, 5 der Promotionsordnung der Fakultät für Biologie

Eidesstattliche Erklärung

Hiermit erkläre ich an Eides statt, die Dissertation: „**Der vakuoläre TPC1-Kanal und seine luminale Kalzium-Sensorstelle im luminalen Porenbereich**“, eigenständig, d. h. insbesondere selbständig und ohne Hilfe eines kommerziellen Promotionsberaters, angefertigt und keine anderen, als die von mir angegebenen Quellen und Hilfsmittel verwendet zu haben.

Ich erkläre außerdem, dass die Dissertation weder in gleicher noch in ähnlicher Form bereits in einem anderen Prüfungsverfahren vorgelegen hat.

Weiterhin erkläre ich, dass bei allen Abbildungen und Texten bei denen die Verwertungsrechte (Copyright) nicht bei mir liegen, diese von den Rechtsinhabern eingeholt wurden und die Textstellen bzw. Abbildungen entsprechend den rechtlichen Vorgaben gekennzeichnet sind sowie bei Abbildungen, die dem Internet entnommen wurden, der entsprechende Hypertextlink angegeben wurde.

Würzburg, den _____

Jinping Lu